TABLE OF CONTENTS

LIST OF TABLES

Page

LIST OF FIGURES

Page

LIST OF ABREVIATIONS

AA2024:	Aluminium Alloy 2024
AMTC:	Aerospace Manufacturing Technology Centre
AR:	As-Received
ASTM:	American Society for Testing and Materials
BCC:	Body Centered Cubic
BSE:	BackScattered Electrons
BCT:	Body-Centered Tetragonal
CCT:	Continuous Cooling Temperature
CRIAQ:	Consortium for Research and Innovation in Quebec
DIC:	Digital Image Correlation
EBSD:	Electron BackScaterred Diffraction
EDM:	Electrical Discharge Machining
FCC:	Face Centered Cubic
FEG-SEM:	Field Emission Gun – Scanning Electron Microscope
FEM:	Finite Element Modeling
FLC / FLD:	Forming Limit Curve / Diagram
FQRNT:	Fonds Québécois de Recherche Nature et Technologies
FX:	Free Expansion
HCP:	Hexagonal Closed Packed
HV:	Vickers Hardness
IN718:	Inconel 718
IPF:	Inverse Pole Figures
ITT:	Interrupted Tensile Test
K-S:	Kurdjumov-Sachs
MUD:	Multiple of Uniform Distribution
NDI:	Non Destructive Inspection
NRC:	National Research Council
NSERC:	Natural Sciences and Engineering Research Council of Canada
PWC:	Pratt & Whitney Canada

RD:	Rolling Direction
SF:	Schmidt Factor
SFE:	Stacking Fault Energy
SIM:	Strain Induced Martensite
SR:	Stress-Relieved
SS321:	Stainless Steel 321
THF:	Tube Hydroforming
TTT:	Time-Temperature-Transformation
UTS:	Ultimate Tensile Strength
YS:	Yield Strength

LIST OF SYMBOLS AND UNITS OF MEASUREMENTS

α':	BCC martensitic phase
ε:	HCP martensitic phase
γ:	Austenitic matrix
γ':	Inconel 718 hardening precipitates
γ'':	Inconel 718 hardening precipitates
δ:	Inconel delta phase
β:	Inconel delta phase
ε_{global}:	Global strain
ε_P:	Plastic strain
ε_0:	Constant parameter
σ:	True stress
K:	Strength coefficient
n:	Strain Hardening coefficient
E:	Young modulus
wt%:	Weight percent
$T_f°$:	Melting point

INTRODUCTION

Metal forming processes are relevant methods to manufacture generic components. Those methods are well-established and generally preferred to other methods such as machining because of their important cost reduction. Deep drawing metal forming processes consist of manufacturing methods using a die-part-die contact to form the piece. They presented many limitations such as a non-uniform thickness distribution on both sides due to the metal contacts. To overcome these disadvantages, forming methods with fluids media have been established (Vollertsen, 2001). Hydroforming technology is part of these methods and is particularly used for thin-walled components. Hydroforming is very close to the conventional deep-drawing method but is based on fluid-part-die contact which allowed a decrease on the thickness drawbacks because of the presence of fluid contact in one side. The hydroforming process can be applied to sheets as well as tubes.

Tube hydroforming technology

Figure 0.1 shows a typical Tube Hydroforming (THF) operation for a simple part. The basic steps followed to manufacture a simple part by tube hydroforming have been detailed as follows by Dohmann and Hartl (2004):

- The initial work piece is placed into a die cavity that corresponds to the final shape of the component,
- The dies are closed by a hydraulic press and the ends of the tube sealed by plungers and the filling-up of the tube begins,
- During the forming stage, the material expands by the simultaneous action of a hydrostatic internal pressure and an external mechanical loading at the tube ends.

All these stages are performed in a single step in the hydroforming press and the final part is obtained directly. This makes the hydroforming process an interesting forming technology.

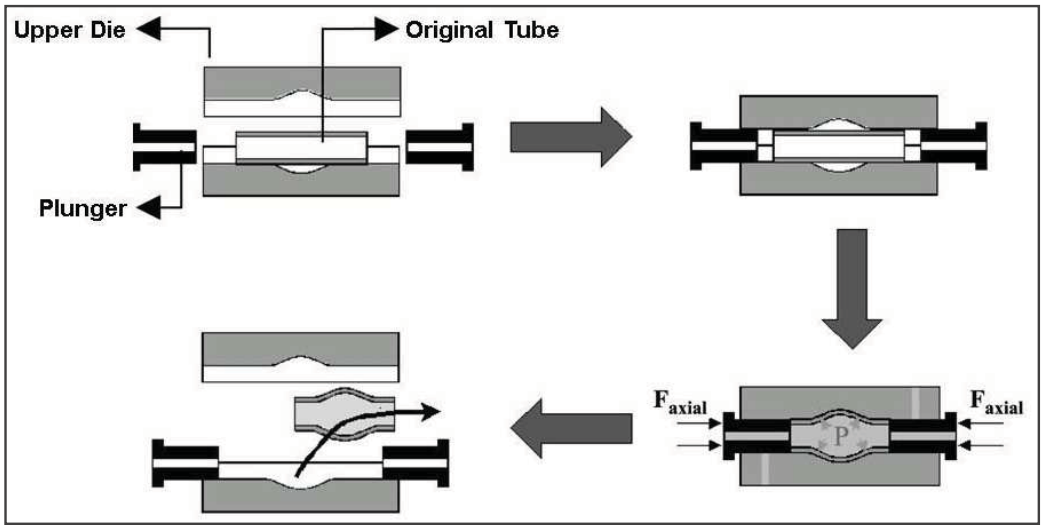

Figure 0.1 Steps in typical tube hydroforming process
Adapted from Koç (2008)

THF presents many advantages compared to traditional "stamping then welding" processes. It allows a lower weight/rigidity ratio as well as a reduction of the number of welds in an assembly which allows a considerable weight reduction. Moreover, it provides higher strength and quality in a part with complex shape. This process is also known for its reduced tooling and assembly costs and the fewer number of secondary operations (Zhang, 1999). With all these advantages, hydroforming became a widely used forming process in many industries such as automotive, sanitary, or electronic (Lang et al., 2004). But, some limitations remain such as slow cycle time, expensive equipment and above all, the lack of extensive knowledge as well as effective database for each step of the process.

The material aspect is another important factor influencing the THF process. The success of the manufacturing of components by tube hydroforming mainly depends on the proper choice, quality and consistency of the incoming materials. Thus, it is important to start the forming process with blanks possessing the desired properties. The required characteristics of raw materials for quality hydroforming applications have been summarized by Koç and Altan (2001) in these terms:

- High and uniform elongation,

- High strain hardening exponent,
- Low anisotropy,
- Close mechanical and surface properties of weld line to the base material in the case of welded tubular materials,
- Good surface quality,
- Close dimensional tolerances (thickness, diameter and shape),
- Burr free ends,
- Tube edges perpendicular to the longitudinal axis.

Based on these requirements, most of the materials used in deep drawing or stamping are suitable for hydroforming. The specificities of tubular raw materials come from the tube making process itself. In fact, tubes are generally manufactured either by roll forming and weld or by extrusion. But, whatever the fabrication process chosen, it will affect the properties of the tube to be hydroformed. In addition, the complexity of the hydroformed components requires that, most of the time, additional preceding operations such as bending or crushing have to be considered together with the hydroforming process itself (Hartl, 2005). As a result, these preliminary operations affect the formability of the raw tube before hydroforming. It is therefore crucial to measure and take into consideration the influence of all the actions occurring before the hydroforming process on the overall formability of the component.

Aerospace industry constraints

In spite of all the advantages of the hydroforming process and although the process is widely used in the automotive industry for instance, it took a long time before the aerospace industry became interested in the process. Its application is relatively new and very challenging in aerospace. On top of the recentness of the technology, it should be taken into account the complexity of the aerospace components, the tight tolerances allowed and the limited formability of the aerospace alloys. This is mainly because aerospace components use high-performance materials with high strength that require high pressures. In fact, most aerospace

materials are known to be high strength and have limited formability. Thus, it is necessary to determine and optimize material properties of aerospace components for the aerospace industries.

In the other hand, economically, the process is interesting for aircrafts manufacturers because they deal with medium to low production volumes and lot of prototyping (Koç, 2008, p. 316). Currently, very little work has been done experimentally on the behavior of materials under the specific conditions of hydroforming (Ahmetoglu andAltan, 2000; Lianfa andCheng, 2008).

Problem statement

The research work presented here is part of the CRIAQ 4.6 project: the development of process modeling tools for virtual manufacturing of aerospace components by tube hydroforming. In the current world context of increased competitiveness and greener choices, Pratt & Whitney Canada is very interested in the application of the hydroforming process to step up their competitiveness by manufacturing engine components by THF which is a green, cost-effective and innovative process. The focus of the doctoral work was to study the mechanical and metallurgical behavior of designated aerospace alloys during hydroforming-type deformation and improve their hydroformability. In other words, the purpose is to bring experimental responses to aerospace material deformation by hydroforming and thus, improve the material models for finite element analysis of the hydroforming process.

Industrial spin-offs

The aim of the research is to endorse the possibility of using the hydroforming process to manufacture complex components by developing a method which allows the extension of the hydroformability of aerospace alloys i.e. a multi-step process has been experimentally developed and will be later modeled for optimization purposes using the finite element method. The resulting materials data obtained from the characterization tests constitute a

significant database for further simulation models. The results of this research led to the development of a manufacturing methodology of aircraft parts by hydroforming based on the optimal mechanical and thermal parameters as well as the accurate forming sequence. The formability improvement of aerospace alloys have allowed the manufacturing of generic aerospace components by hydroforming.

Outline of the thesis

The thesis is organized in five chapters followed by the conclusions and some recommendations. Since this thesis is paper-based, three out of the five chapters are papers published or at least submitted to scientific peer-reviewed journals.

The first chapter is separated in three sections. It puts in place the structure of the thesis by grouping together the research objectives, a succinct literature review (completed in the specific papers) and a methodology description. The first section reminds the research problematic and objectives. The research objectives are addressed and the appropriate chapter responding to each of them is referenced. The second section consists of a general literature review which sets the context of the work. A more specific and detailed literature review is included in each paper. Finally, the last section describes the methodology and brings out the originality of the research.

Chapters 2 to 4 are dedicated to the austenitic stainless steel 321 (SS321). Chapter 2 presents the multistep forming process applied to SS321 through interrupted tensile tests. The mechanical aspect has been widely covered but the metallurgical properties were just touched on.

Chapter 3 focused on the metallurgical evolution of SS321 under multistep tensile tests. The mechanical properties at each step of the process were analyzed as well and put in parallel with the metallurgical response.

The application of the multistep process to a hydroforming type of deformation is presented in Chapter 4. It is a conference paper which present an industrial application to better illustrate the finality of the present work. SS321 tubes are subjected to interrupted free expansion tests which are hydroformed closest mechanical tests.

Chapter 5 is about superalloy Inconel 718 (IN718). This material is very complex and the main work was to identify the appropriate heat treatment which can be used as intermediate step during the multistep process and will allow a formability improvement of the material. An important metallurgical study has been conducted to understand the mechanisms involved in the formability enhancement of this alloy.

Finally, the conclusion sums up the contributions of this thesis as well as the recommendations for upcoming researches.

CHAPTER 1

LITERATURE REVIEW

In this chapter, the research context is defined. In the first section, the problem encountered in this thesis as well as its objectives are presented. Then, a critical overview of the literature related to the existing formability improvement methods on one hand, and to the studied aerospace materials on the other hand is performed. Finally, the methodology applied to conduct this research is described. The last section also highlighted the originality of the research.

1.1 Research problematic and objectives

1.1.1 Research problematic

The research project conducted during this thesis is part of the CRIAQ 4.6 project: Process Modeling Tools Development for the Virtual Manufacturing of Aerospace Components by Tube Hydroforming. The global purpose of the project can be defined as assessing the applicability of the THF technology to manufacture generic components for aerospace industry. Tube hydroforming of aerospace alloys is very challenging and faces several issues which have to be addressed in the CRIAQ project. In fact, the technology is relatively recent and also, the aerospace components are generally very complex and require a high accuracy/reliability. In addition, the tight tolerances used in the industry as well as the limited formability of the aerospace alloys lead to a lack of extensive knowledge on the THF of aerospace materials.

To overcome the above issues, the CRIAQ project has been divided in three sections, each of them answering one particular objective as presented Figure 1.1.

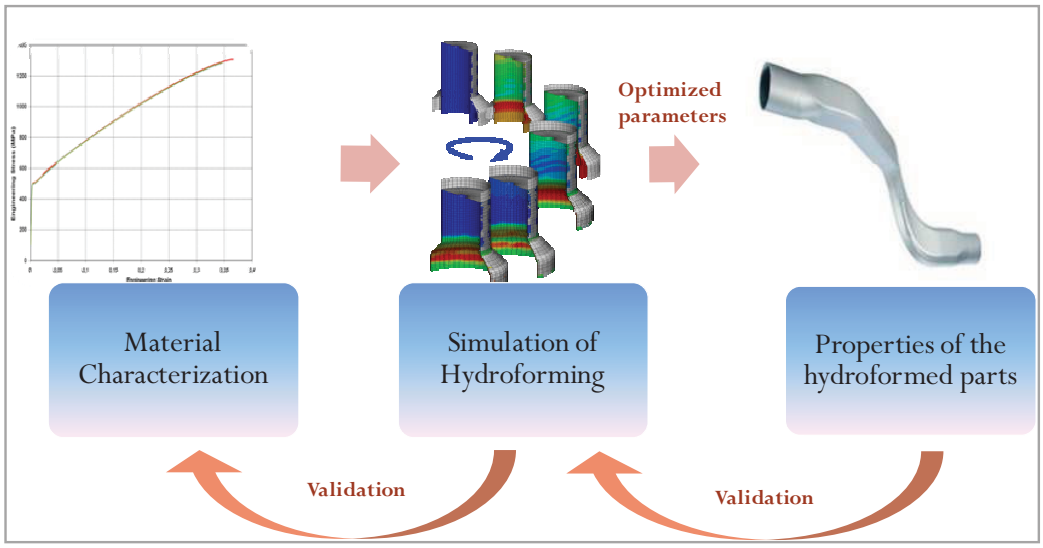

Figure 1.1 General flowchart of the CRIAQ 4.6 project.

The first step consists on performing a complete material characterization to determine the appropriate material properties (mechanical, contact, friction…) which was used to build accurate material models in the next step of process simulation. The doctoral research project presented here comes to this section. It consisted of studying experimentally the behavior of the objective aerospace alloys (stainless steel 321 and superalloy Inconel 718). It followed up a master work conducted on the development of appropriate methods to characterize aerospace alloys for THF applications in order to feed simulation models (Anderson, 2010). This work had been an opportunity to highlight how the designated alloys can be hardly deformed and had sparked off the present PhD study.

With the appropriate material properties obtained in the first section of the project, a valid and robust material model is built and integrated in some Finite Element simulations in order to determine the optimized parameters which will be used to experimentally manufacture prototype parts. This second part of the global project was the subject of another PhD (Saboori, 2015). Finally, based on the optimized parameters acquired, some parts were hydroformed and the properties of the hydroformed components were studied to confirm that they met the industrial requirements. Between each step, several validation tests were

iteratively performed to improve the procedure and to ensure that the industrial requirements are met continuously.

1.1.2 Research objectives

The main objective of this project is to develop a multistep forming process which allows formability improvement of specific aerospace alloys for hydroforming applications.
The specific objectives are:

1. Study the mechanical behavior of the aerospace alloys subjected to interrupted mechanical tests simulating the multistep hydroforming process
2. Investigate the metallurgical response of the material under this type of forming
3. Collect experimental data from the materials deformed by multistep hydroforming-type deformation which will be used to feed finite element analysis of the hydroforming process
4. Better understand the microstructural evolution of the materials at each stage of the multistep process and when subjected to several cycles of "deformation + heat treatment"
5. For the IN718 complex material, investigate the most appropriate intermediate heat treatment which conduct to formability improvement of this alloy

1.2 Literature review

The literature review presented here has been based on three main axes. First of all, the common methods usually conducted to improve the formability of any materials have been looked over with their advantages and limitations in order to highlight that the multistep process is the most effective method in the case of our research. In the other end, the restoration mechanisms which occur during the softening heat treatments and lead to the formability extension have been summarized. Finally, the designated aerospace materials are presented in details with an emphasis on their similarities and differences which justify their choice for the research.

1.2.1 Methods to increase the formability

Several authors were interested in ways to increase the “capacity to deform” of different materials. The objectives behind these studies were the emergence of a new generation of parts weighed lighter but with higher strength and more and more complex shapes. Globally, after the analysis of several papers on the domain, two elements can be brought out. First, most of the techniques are interested in light weight alloys generally represented by Aluminum (Al) alloys, Magnesium (Mg) alloys or Advanced High Strength Steels (AHSS) (Choi, Koc andNi, 2008) even if the techniques were mostly tested on Al alloys. All the techniques presented imply elevated temperatures, either at the same time as the forming or between forming steps. They can be separate into two groups depending on the moment of the heat treatment(s).

1.2.1.1 Hot or warm forming processes

In order to get the maximum from light weight alloys, which are associated with a limited formability, the use of elevated temperatures has been considered as a potential solution (Neugebauer et al., 2006). Forming at temperature superior to the room temperature has the benefit not only to significantly improve the ductility of the material, hence the forming capacity, but also by reducing the yield point, to decrease the forming forces and pressures required. Neugebauer et al. (2006) distinguished hot and warm forming in relation to the recrystallization temperature. This temperature is the minimum temperature at which the deformed grain structure of a metal is replaced by a new grain structure when exposed to heat treatments. Thus, a hot forming operation below this temperature is designed as a warm forming. The work piece is heated to the point where the yield point and work hardening are reduced. At or above the indicated temperature, they are called hot forming processes and recrystallization takes place. In addition to the level of temperature reached, another important issue is the way the heat is given to the part. Neugebauer (2006) suggested three types of temperature management systems. The product can be heated outside the tool and then deformed in the tool which is not heated. This process is costless but it faced an

important heat loss during the part transfer. The product can also be pre-warmed outside the tool and formed in a heated tool. The heat transfer loss is then minimized but heating the tool could be expensive and a challenge. Finally, the product can be heated and formed in the tool. For this process, an important work has to be done on the design of the forming and heating equipment.

The results obtained with these techniques on the formability enhancement depend on the material. According to Groche et al. (2002), the use of warm forming process, in the case of aluminum alloys, results in a lower yield point and a higher expansion. For magnesium and titanium, their hexagonal lattice structure leads to a limited number of sliding planes for forming at room temperature (Kleiner, Geiger andKlaus, 2003). In the case of magnesium, the elevated temperatures contribute to enhance forming capabilities by improving the ductility and also reducing the forming pressures required. For titanium alloys, at forming temperatures below 500°C there is no significant improvement in the forming behavior (Sibum, 2003). Neugebauer (2006) identified that the challenge in forming Advanced High Strength Steels is to keep their improved characteristics, specially strength, in the final part. That is coming with limitations in terms of forming capability. In fact, their high strength requires higher processing forces and adapted forming tools. In addition, their high yield strength leads to greater dimensional deviations due to spring back which have to be anticipated when designing forming dies. Consequently, he concluded that warm forming conducted below recrystallization temperature leads to an improvement in forming characteristics without any structural changes in the case of these alloys. On the contrary, hot forming is more difficult to conduct because of high temperatures to be reached and the related limitations of the facilities.

1.2.1.2 Incremental forming processes

Incremental forming process is a technique where a part is formed into the final work piece by a series of small increments of deformation. The multistep forming process stemmed from the incremental technique as a process that can improve material formability through the use

of recovery heat treatments applied between increments of deformation (Golovashchenko andKrause, 2005). These authors have used interrupted tensile tests, then plane strain tests, to simulate the incremental forming process on aluminum 6xxx alloys. Their objective was to identify the right heat treatment sequence that is able to restore the formability of the metal without penalizing alloy's performances. In conclusion, Golovashchenko and Krause (2005) attested that a particular heat treatment (250˚C, 30s) of prestrained (10%) aluminum alloy AA6111 provided sufficient recovery to increase elongation from 25% to 45% with one intermediate heat treatment. Even if the heat treatment performed in this case is very short and can hardly be performed in the case of the objective aerospace alloys, it is observed that an intermediate heat treatment can have an impact on the elongation increase. They also highlighted the key factors to attempt formability improvement of the alloy, i.e. the heat treatment temperature, time and the amount of deformation between heat treatments. The incremental strain should reflect an adequate amount of deformation corresponding to the first forming operation of a part. In the case of hydroforming, it could be equivalent to the bending before hydroforming step for instance. Also, this deformation should be enough to generate significant microstructural changes but not enough to cause localized necking. The heat treatment specifications should be chosen in consideration of the alloys properties and responses to annealing. In the case of these aluminum alloys, the heat treatment had removed the majority of the deformation done during the increments without incurring significant aging. The authors had tested more complex states of stress through dome testing and the results obtained were in good agreement with their tensile tests results. This shows that the results obtained with very simple tests as tensile tests could be extended to complex states of stress observed in most forming operations for some alloys.

Other studies had also been conducted on aluminum alloy AA2024 about the effect on the formability of pre-strain and heat treatments (O'Donnell et al., 2008a; O'Donnell et al., 2008b). The first paper studied the effect of three pre-strain levels and the recovery annealing process. The pre-straining was represented by tensile testing, and the plaques were annealed at (340˚C, 60 min) before undergone final deformation. The formability had been measured through Forming Limit Diagram (FLD). The results obtained had shown for pre-strain less

than 12% no effect on the formability was noticed. The Forming Limit Curve (FLC) for 12% pre-strain indicates an improvement in formability, particularly close to plane strain region, however, the authors do not suggested any clear explanations. It had also been observed a reduction in formability for all specimens regardless of the pre-strain level in the biaxial strain region which was explained by sheet thinning combined with the appearance of surface defects and polygonization during recovery anneal (O'Donnell et al., 2008a). The results obtained for all the processing routes tested in these papers indicated a significant change in the materials texture.

1.2.2 Heat treatments

Heat treatments can be performed to restore the ductility of the material in order to be able to continue the deformation. In the case of multistep forming process, the intermediate heat treatment applied would be annealing. The term annealing is a generic metallurgical term which suggests the subsequent heat of a deformed material to high temperature. In other words, it denotes a heat treatment conducted to soften metallic materials. Generally, the reason for annealing a piece is to make possible further deformations without any fracture (Byrne, 1965, p. V). The annealing can be divided into three stages: recovery, recrystallization, and grain growth (or coarsening) according to several authors (Brooks, 1982, p. 33; Doherty et al., 1997; Humphreys andHatherly, 2004) and they will be detailed below. Figure 1.2 illustrates schematically the annealing process at the microstructural level of the material.

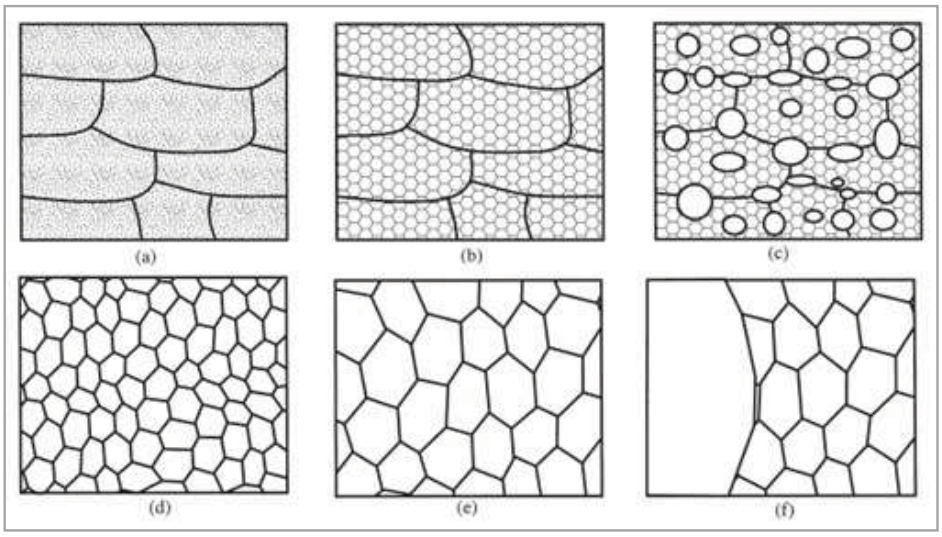

Figure 1.2 Schematic diagram of the main annealing processes;
(a) Deformed state, (b) Recovered, (c) Partially recrystallized,
(d) Fully recrystallized, (e) Grain growth, (f) Abnormal grain growth
Adapted from Humphreys and Hatherly (2004, p. 2)

When a material has its crystalline structure deformed (Figure 1.2a), it is common to recover from this state by heat treatments. During the deformation, energy is stored in the lattice through dislocations. And it is this energy which is released through when the part is annealed. Doherty et al. (1997) pay a particular attention to define recovery (Figure 1.2b) as followed: « Recovery can be defined as all annealing processes occurring in deformed materials that occur without migration of a high angle grain boundary ».

Recrystallization (Figure 1.2c & d) is a metallurgical phenomenon at the structural level which occurs during or after the deformation and/or annealing processes. The recrystallization has been defined by Doherty and al. (1997, p. 219) as « the formation of new grain structure in a deformed material by the formation and migration of high angle grain boundaries driven by the stored energy of deformation ». This means that before recrystallization can take place, it is necessary, for the material, to have undergone prior deformation up to a critical point. This is the critical strain which refers to the minimum amount of deformation required to provide nuclei with sufficient stored energy to drive their growth. Thus, the major difference between recrystallization and recovery resides in the

formation and migration (recrystallization) or not (recovery) of these high angle grain boundaries.

Finally, grain coarsening (Figure 1.2e), according to Doherty et al. (1997) can be viewed as « processes involving the migration of grain boundaries when the driving force for migration is solely the reduction of the grain boundary itself ». « The high angle grain boundaries are those with greater than 10° to 15° misorientation » according to the authors. In the case of grain growth, compared to recrystallization, only the migration without formation of grain boundaries occurred. Very often, all these mechanisms occur gradually, but without any precise start or stop points. They, generally, overlap each other. Brooks (1982, p. 34) summarizes the annealing steps defined above in terms of driving force, mechanism and result as shown in Table 1.1.

Table 1.1 Driving force and mechanisms associated with the annealing process
Adapted from Brooks (1982)

	RECOVERY	RECRYSTALLIZATION	GRAIN GROWTH
DRIVING FORCE	Reduction in internal energy by dislocation rearrangement	Further decrease in internal energy by removing dislocations remaining after recovery	Reduction in total grain boundary energy
MECHANISM	Movement of vacancies and atoms to produce dislocation climb or glide	Growth of strain-free regions by atom-by-atom jump across interface between strain-free grains and matrix	Large grains consume small grains by atom-by-atom jump across grain boundaries
RESULTS	- Residual stresses removed - Strain-free regions form	- New set of grains form, frequently with preferred orientation - Strength reduced - Ductility increases	- Decrease in strength

With Table 1.1, it is possible to visualize clearly the main aspects of the annealing process in terms of metallurgical mechanisms. All these steps manifest themselves through heat treatments applied to the material. Since the multistep process combines deformation and heat treatments, their study will be the baseline of the work performed in this thesis.

1.2.3 The designated aerospace alloys

This section presents the existing heat treatments for austenitic stainless steels as well as nickel-iron superalloys before looking over the specificities of the studied materials.

1.2.3.1 Austenitic stainless steels heat treatments

The stainless steels are well known for their optimal corrosion resistance. They can be differentiated thanks to the major phase in presence and this phase will dictate the type of heat treatments. Austenitic stainless steels cannot be hardened by heat treatment but their strength could be increased by alloying or by cold working which may involve strain-induced martensite formation (Krauss, 1990, p. 373; Totten, 2007, p. 705). The heat treatments applied to austenitic stainless steels are generally annealing, treatments to prevent corrosion, and stress relief as detailed below:

- *Solution annealing:* this heat treatment is generally performed before any usage. Its purpose is to dissolve the phases that have precipitated during processing of the material, such as carbides (Totten, 2007, p. 706). The annealing causes recrystallization of the strain-hardened microstructure and also restores the ductility of the alloy (Krauss, 1990, p. 373). The lower temperature limit has to be chosen over the temperature range of carbides precipitation, i.e. superior to 900°C, and the upper limit is controlled by the grain growth. The common range for solution annealing temperature of austenitic stainless steels is between 955°C and 1065°C (Totten, 2007). In addition, a particular care should be taken to cool sufficiently fast to avoid carbides precipitation. In the case of SS321, water cooling is not mandatory, air cooling is sufficient to avoid sensitization.

- *Stabilize annealing:* it is used in the case of stabilized steels such as SS321 to assure maximum intergranular corrosion resistance. In fact, it causes precipitation of alloy carbides which, as a result, decrease the amount of Carbon available for Chromium carbide precipitation, and hence, maximize corrosion resistance. The optimal heat treatment should be performed after solution annealing in a temperature range between 845°C and 955°C for a duration up to 5h (depending on the sample size).
- *Stress-Relief annealing:* the purpose of this heat treatment is to reduce internal stresses without intentionally changing the material structure and properties (Chandler, 1995). The most effective way is to cool the alloy slowly from the solution annealing temperature. However, during slow cooling, detrimental carbide precipitation may occur. But, on the other hand, a fast cooling may reintroduce residual stresses. The range of temperature for stress-relief treatment is generally between 925 and 1010°C. At this temperature range, longer time exposure can be used without significant grain growth (Totten, 2007, p. 708).

1.2.3.2 Stainless steel 321

SS321 is part of the stainless steels called stabilized. The addition of strong carbide formers such as titanium allows an important reduction of sensitization. Sensitization is defined as the precipitation of carbides at grains boundaries resulting in the depletion of Cr making possible intergranular corrosion. In fact, the titanium added avoids intergranular chromium carbide precipitation, i.e. sensitization because the carbon combines preferentially with Ti to form harmless Ti carbides and leaves Cr in the solution to maintain full corrosion resistance (Boyer, 1990, p. 203). Thus, it possesses one of the highest corrosion resistance among the stainless steels. It is also very highly alloyed so that it is able to remain in the austenitic condition at low temperatures and cannot be hardened by heat treatment (Allen, 1969, p. 302). SS321 has an high interest because it develops very interesting mechanical properties by cold working into a matrix without any precipitates. However, it is subjected to martensite formation. There are two possibilities for the formation of martensite in the austenitic stainless steels: by cooling below the room temperature or in response to cold work (Krauss,

1990, p. 366; Totten, 2007, p. 709). The transformation during cooling occurs at a specific temperature (M_s) which could be calculated in function of the steel composition based on empirical equations (Eichelmann andHull, 1953). For SS321, M_s is around cryogenic temperatures as most of austenitic stainless steels. This M_s corresponds to the formation temperature of the martensite α' which is a body-centered cubic structure. Another martensite is expected when the stacking fault energy of austenite decreases (Totten, 2007, p. 709). The structure of this phase called ε is hexagonal compact-packed and arises from regular stacking of intrinsic faults on alternated close-packed {111} planes of the austenite (Marshall, 1984). At room temperature, the martensite observed in stainless steels is strain-induced martensite. The martensite generated in response to cold working is called Strain Induced Martensite (SIM). As the austenite phase is not stable at room temperature, applied plastic deformation leads to the phase transformation from metastable austenite to more stable martensite. The formation and the amount of both kinds of martensite depend on the alloy composition, the stacking fault energy, the temperature, amount and rate of the deformation and also the stress state during deformation (Kaieda andOguchi, 1985). The formation and the amount of martensite (both types) increase with decreasing deformation temperature (Totten, 2007, p. 709). Finally, when the stainless steels containing deformation-induced martensite are annealed, the martensite may recrystallize or revert to austenite and this may affect the formability of the austenitic stainless steels (Peterson, Mataya andMatlock, 1997).

1.2.3.3 Superalloys heat treatments

The heat treatments of superalloys are very complex and depend on their composition, phases, structural effects as well as properties needed at the end. Their structure is constituted by a stable FCC austenitic matrix γ containing several other phases such as strengthening phases, primary carbides, secondary phases, and some oxides (Mons, 1996). The complex structure of these alloys made their heat treatments very crucial. The heat treatments are performed either to strength by precipitation or to harden by solid solution. The general heat

treatments conducted on the Nickel-Iron base superalloy IN718, detailed by DeAntonio et al. (1991), are listed below:

- *Solution Treating*: the goal of this heat treatment is to go up to a temperature high enough to put into solution the hardening phases and dissolve some carbides (Cr ones in particular). Its consequence is to produce maximum corrosion resistance or to prepare for age hardening. Its temperature depends on the properties desired. It is generally followed by either a quenching or aging treatments. Quenching after solution treating allows to maintain, at room temperature, the supersaturated solid solution obtained at high temperature (DeAntonio et al., 1991; Mons, 1996). The quenching leads to a finer age-hardening precipitate size compared to slow cooling precipitates, as well as it affects the distribution of precipitates in the matrix.
- *Stress Relieving:* this heat treatment is more often performed on non-age-hardenable alloys and consists of compromising between maximum relief of stresses and damaging effects to high-temperature properties as well as operation costs (Mons, 1996). When applied to age-hardenable alloys, the stress relieving heat treatment will be performed at the same temperature as the solution treating.
- *Annealing:* in the case of superalloys, the annealing heat treatment implies complete recrystallization and attaining maximum softness. Its purpose is to reduce hardness and increase ductility to facilitate forming or machining, prepare for welding, relieve stresses after welding, produce specific microstructures, or soften age-hardened structures by dissolution of second phases (DeAntonio et al., 1991). It is usually applied to non-hardening alloys. For the age-hardenable alloys, the annealing is the same as for the solution treating.
- *Aging treatments:* the objective of these heat treatments is to strengthen age-hardenable alloys by causing precipitation of maximum quantities of one or more phases from the supersaturated matrix that is developed during solution treating (DeAntonio et al., 1991). Since more than one phase can precipitate from the alloy matrix, the selection of the aging temperatures and times is very important and should be chosen judiciously. In Inconel 718, a double aging treatment (aging in two steps) consisting of holding the material solution treating during 8h at respectively 720 and

620°C is commonly performed to control the size distribution of the two main precipitates γ' and γ''.

1.2.3.4 Superalloy Inconel 718

IN718 is a nickel-iron base superalloy, part of the high-temperature material class. It exhibits excellent physical and mechanical properties, which remain from cryogenic to elevated temperatures ($0.8\times T^{\circ}_{f}$) as well as high strength and excellent corrosion resistance at high temperatures. Its FCC nickel matrix confers toughness and ductility properties. In addition, the nickel brings stability of the FCC form from room temperature to its melting point (Reed, 2008, p. 25). Each alloying element has its particular role and influences the phases' stability. For example, Ni, Cr, and Mo match with the austenite matrix γ and thereby stabilize it. Others, like Nb, Ta, Ti, Al with their greater atomic radii (compare to Ni) promote the formation of ordered phases (Reed, 2008, p. 35). IN718 superalloy microstructure can be detailed as below (Slama andCizeron, 1997):

- The γ phase exhibits the FCC structure and constitutes a continuous matrix phase in which the other phases reside.
- The γ'precipitates [Ni_3(Al,Ti)] (ordered $L1_2$), coherent with the γ–matrix and γ'' [Ni_3Nb] precipitates which have a BCT structure are the main strengtheners. They impart reasonably high tensile and creep strength at elevated temperatures while maintaining adequate ductility, fracture toughness, and fatigue properties. Contrarily to most of the superalloys which are hardened by precipitation of the γ' phase, the main hardening phase of IN718 is the γ'' precipitates.
- The δ (or β) precipitates [Ni_3Nb] generally precipitate at the γ–grain boundaries. This orthorhombic phase is incoherent with γ, thus do not confer any strength to the alloy.
- MC-type carbides (MC, M_6C, $M_{23}C_6$) precipitate also at the γ–grain boundaries. The carbon combines with reactive elements such as Niobium or Titanium to form the carbides. These precipitates improve the intergranular creep resistance of IN718.

The various phases are formed jointly or successively depending on the temperature range and the aging time. The TTT (Temperature-Time-Transformation) diagram of IN718, presented in Figure 1.3, allows defining precisely the precipitation domains of each phase. It is very useful for the definition of the appropriate heat treatments.

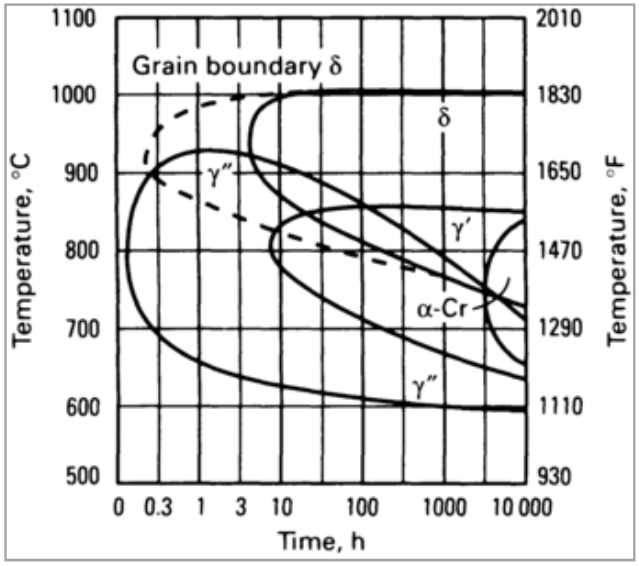

Figure 1.3 Temperature – Time – Transformation diagram of a hot-forged IN718 bar
From (DeAntonio et al., 1991)

To address the objective of this research, the appropriate heat treatment to extend the IN718 formability consists in dissolving all the strengthening phases while limiting γ grain growth. Thus, the ideal IN718 microstructure would be made up of δ precipitates dispersed into the γ matrix. Based on Slama and Cizeron (1997) study on the IN718 behavior under isothermal heat treatments, the perfect heat treatment will be held at a temperature between 890°C, which corresponds to the δ precipitates coalescence, and 920°C, temperature at which the dissolution of δ starts. Similarly, from the CCT diagram (Continuous Cooling Temperature) built by Slama and Cizeron, the cooling rate should be maintain between 5°C/s and 100°C/s to assure that only the δ phase precipitates and no hardening phases are formed. One can

expect that this type of microstructure will provide to the material a very low strength and a very high ductility.

1.3 Conclusions

The two objective materials have in common their crystallographic structure: Face-Centered Cubic matrix structure. In the case of SS321, the matrix base is an Iron – Chromium alloy system. The nickel added to the austenitic phase stabilizes the FCC structure at room temperature. SS321 can be defined as a substitutional solid solution of chromium and nickel in iron (Lula, Parr andHanson, 1989, p. 21). IN718 is a nickel-iron based superalloy. Its austenitic FCC matrix is completed with an important number of alloying elements which made IN718 a very complex material (Reed, 2008, p. 34).

The multistep process applied to SS321 corresponds to perform cold work in a matrix without precipitates. On the contrary, for IN718, it is about cold work in the same matrix but full of precipitates which are in addition very sensitive to heat treatments. As a result, studying SS321 represents a solid baseline to assess the methodology before working on the more complex material IN718.

CHAPTER 2

ORGANIZATION OF THE THESIS

The purpose of this chapter is to describe the scientific approach of the project in order to understand the interrelation between the following chapters. To perform material characterization, several methods have been developed over the time. In a context of formability improvement, two different approaches have been considered : from a macroscopic point of view with mechanical tests and at a microscopic level with metallurgical characterization. The most appropriate methods conducted in both cases to meet our objectives of formability improvement are detailed in this section as well as the global adopted methodology, and the experimental plans put in place.

2.1 The multi-step forming method approach

To reach the objective fixed in this research, a multi-step forming method approach had been adopted. It consists in dividing the complete forming process into several steps of deformation, each of them followed by an appropriate heat treatment. The heat treatment is performed to restore the material properties so that at the next level of deformation, the forming, is conducted on a stress free new material. Thus, higher level of total deformation can be reached and more complex parts manufactured. Practically, for tube hydroforming, a raw tube is heat treated after bending and again after crushing and a last time before hydroforming. At the end, another heat treatment could be necessary to come to the final part with the required properties.

In order to emulate the multistep forming process, that is to say each level of forming (bending / crushing / hydroforming) during the research project, interrupted mechanical tests were performed. As described in Figure 2.1, the forming process step was divided into either interrupted uniaxial tensile tests or free expansion tests. After the first level of deformation, the specimens were heat treated before undergoing the second step of deformation. The characterization procedure was performed simultaneously on macroscopic and microscopic

levels. In fact, on the macroscopic scale, the influence of the process on the mechanical properties of the materials was studied as well as the strain distribution during the forming section and the constitutive equations describing the material flow behavior. On the other side, the metallurgical behavior when the material is subjected to interrupted mechanical tests was investigated through microstructure and texture analysis. Also, the changes in the material structure, that is to say, the presence and/or disappearance of elements or phases were followed microscopically.

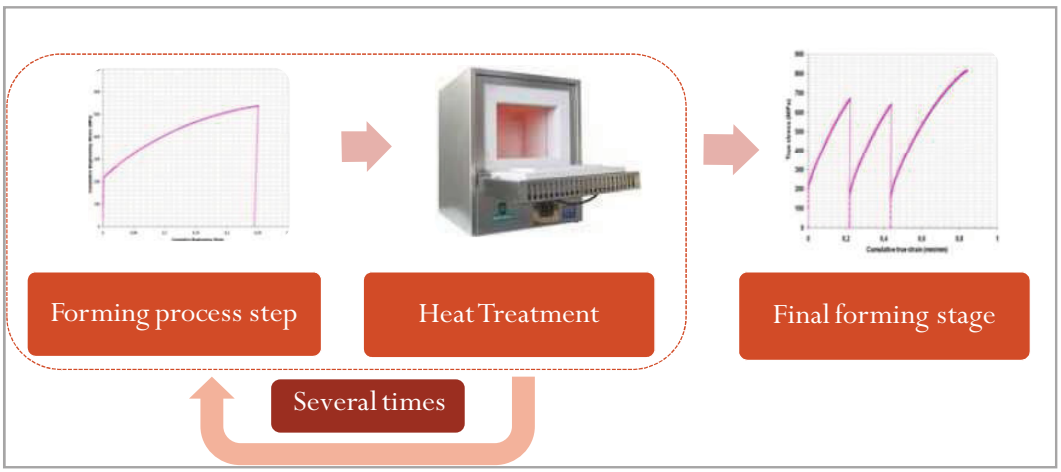

Figure 2.1 Multistep forming process description.

2.2 Mechanical tests

2.2.1 Generalities

The most relevant mechanical tests to properly simulate a hydroforming step has been identified as uniaxial tensile and free expansion tests. The reasons for choosing these mechanical tests as well as their relevance have been detailed in the master's thesis conducted under the same project (Anderson, 2010). To summarize, the uniaxial tensile test is one of the most commonly mechanical tests conducted because it is the easiest to set up and the mechanical properties are measured directly with the displacement / force data recorded. Thus, interrupted tensile tests constitute the main part of the thesis and have been conducted

on both materials. However, the uniaxial state of stress due to the pulling direction is an important drawback here because it is far from the hydroforming process. As for the free expansion test, it is very close to the hydroforming process but the static mechanical properties cannot be measured directly and have to be calculated. In addition, its set-up is more challenging and requires important resources. For these reasons, fewer tests have been performed and they are presented as a case study for SS321 material.

2.2.2 Design of experiments

All tests were done on material stocks (cold-rolled sheets) with 0.9 mm thickness in the form of standard tensile test specimens and 50.8 mm outside diameter for 0.9 mm thick seamless tubes for free expansion tests. The main objective of the first set of tests was to answer objectives 1 & 3, i.e. study the mechanical behavior of the material under multistep process and collect appropriate experimental data. This set of tensile tests (Chapter 2) was performed on SS321 at NRC-AMTC on standard specimens following ASTM E8/E8M in a servo-hydraulic tensile test machine (MTS810) equipped with a laser video extensometer as well as a digital image correlation system. Up to 3 cycles of tensile testing + heat treatment were performed and each step was repeated at least two times for a total of 20 tests. Two starting conditions were also studied, which double the number of tests for this section.

The second set of tensile tests replies to objectives 2 & 4 which are about investigating microstructural evolution of the material under multistep process. These tests (Chapter 3) were conducted on SS321 at ETS on subsize specimens in a Kammarath&Weiss micro testing machine equipped with a mechanical extensometer. Subsize tensile specimens (15 mm gauge length and 4 mm width) had been machined by EDM from standard tensile (7 micro scale specimens per 1 standard) as shown in Figure 2.2. Up to 2 cycles of tensile tests + heat treatment have been performed for a total of 8 tests. Their purpose was to go into the correlation between the mechanical properties and the metallurgical response in depth. Microscale tensile tests have been chosen to allow the microstructure / texture analyses in parallel with the mechanical deformation. In other words, the microstructural analyses were

performed on specimens that had already undergone a deformation step. Also, it has been validated that no difference existed between standard and subsize tensile tests in terms of mechanical properties.

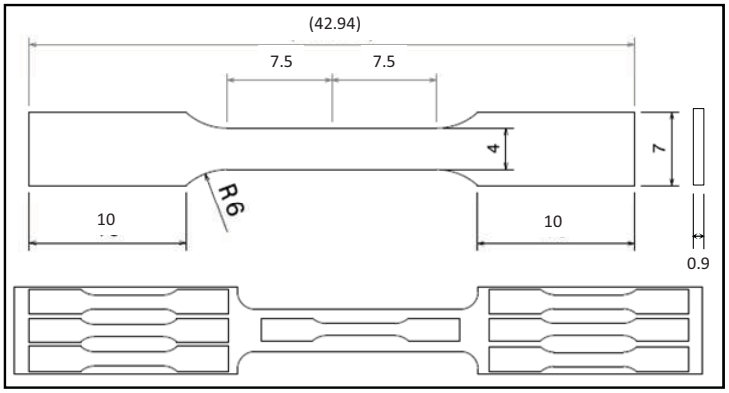

Figure 2.2 Microscale tensile specimen drawing and sampling plan (dimensions in mm)

The free expansion test experiments put the focus on objective 3 which is collecting appropriate experimental data to feed upcoming finite elements models. To validate the pertinence of the multistep process in the case of hydroforming, a case study has been conducted in SS321 tubes (chapter 4). In the free expansion test, a raw tube is placed in an open die into a hydroforming press and pressurized internally until the unclamped region deforms and bursts. This mechanical test, very close to the hydroforming process, is performed on a biaxial state of stress or more and allows reaching higher levels of deformation as expected during the forming processes. The free expansion test (FX) was performed at NRC-AMTC on 1000-Ton fully instrumented hydroforming press capable of more than 400MPa internal pressure. The load data had been extracted from the hydroforming press control system in conjunction with a non contact 3D measurement deformation system (Aramis®) to evaluate tubes expansion. A minimum of 10 tests have been performed including single FX and interrupted FX (cycle of deformation + heat treatment).

2.3 Metallurgical studies

In order to achieve the formability improvement of the designated materials, it is necessary to better understand the relation between the material structure and the mechanical properties previously determined. This part of the work was about following the microstructural evolution to explain the macroscopic changes observed on the materials properties. By understanding the relationships between microstructural and mechanical properties at each level of process, it had been possible to investigate, develop, and predict the appropriate parameters for the multistep forming process. In addition, the metallurgical studies conducted will be useful for documenting properly the heat treatment history of the materials in further FEM simulations. The metallurgical studies have been performed through microstructure analysis and crystallographic texture measurements. Both materials were characterized at micro scale using optical as well as Scanning Electron Microscopy. Specially, the microscope used at ETS was a Field Emission Gun Scanning Electron Microscope (FEG-SEM) Hitachi SU70. For crystallographic texture measurements, the SEM was combined with the Electron BackScattered Diffraction (EBSD). This microstructure characterization method allows an extensive metallurgical study of the material through grain size, grain orientation, phase identification as well as crystallographic texture analyses.

In the case of SS321, the subsize tensile specimens microstructures have been studied to determine the modifications on grains size, inclusions, and precipitates due to each step of the process. As well, previous heat treatments and deformations impact have been revealed. This part of the project fulfilled mainly objective 4, better understands microstructural evolution and is extensively developed in Chapter 3.

In the case of IN718, the metallurgical analyses were focused on the development (through heat treatments) of the most suitable microstructure for formability enhancement purpose. Thus, the same microstructural characterization tools were used on IN718 coupons subjected to various heat treatments (Chapter 5). A total of 40 coupons were analyzed in order to study the evolution of some phases with the view to improving formability. This set of experiments

answered Objective 5, dedicated to IN718, which focuses on investigating appropriate heat treatments for formability improvement of this complex alloy.

2.4 Experimental design and research significance

The chart presented in Figure 2.3 summarizes the experimental plans and correlates them with the objectives and the thesis outline.

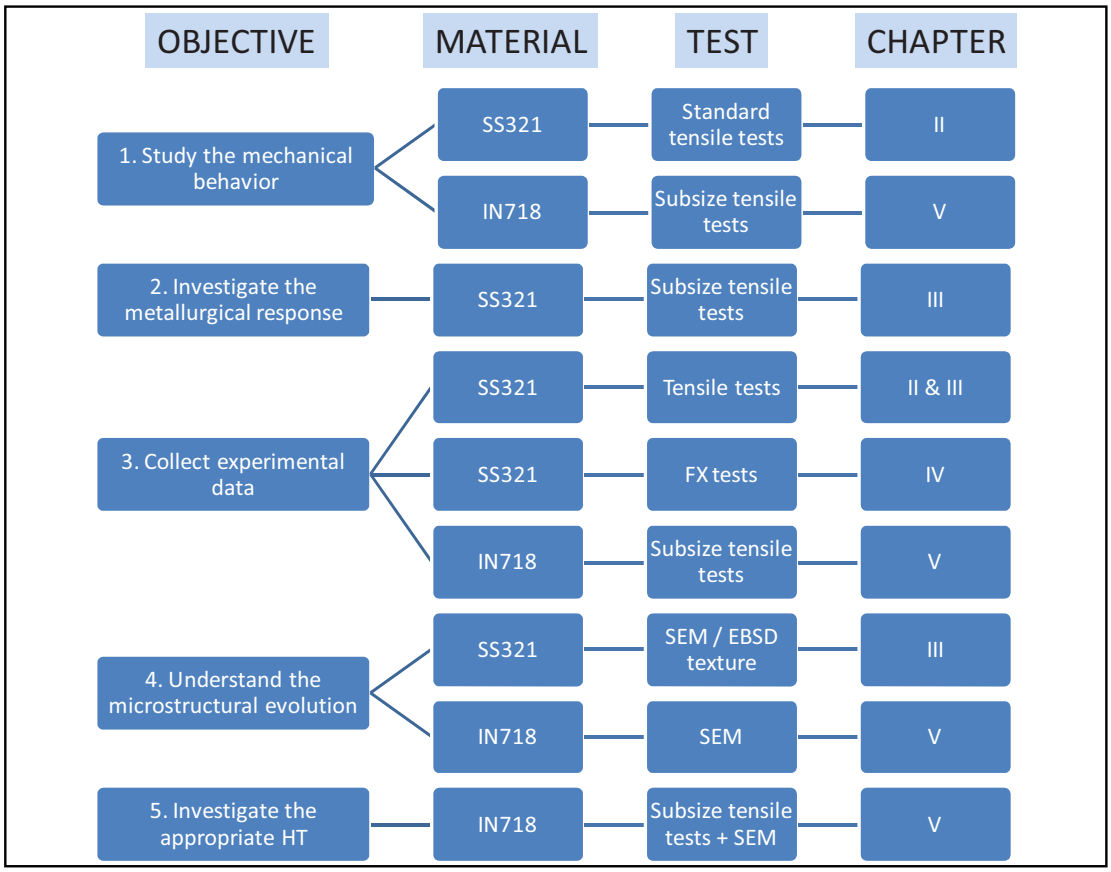

Figure 2.3 Experimental plans and thesis structure

According to the literature, the aerospace alloys, although they are very difficult to deform, have not been subjected to incremental or multistage forming. Forming aerospace materials by multistep process as performed in this work can be considered as an innovative way of

manufacturing aerospace parts. In addition, the multistep forming process allows a complete control of each step whether the heating or the forming comparing to other forming processes at elevated temperatures. The originality of the research work lies in the fact that it is mainly experimental. This is a way to fill partly the lack of knowledge observed on the hydroforming of aerospace alloys. In addition, it had created a useful database of aerospace materials properties for subsequent experimental works or simulations.

CHAPTER 3

PAPER 1: IMPROVING THE FORMABILITY OF STAINLESS STEEL 321 THROUGH MULTISTEP DEFORMATION FOR HYDROFORMING APPLICATIONS

Melissa Anderson[1,2], Javad Gholipour[2], Florent Bridier[1], Philippe Bocher[1], Mohammad Jahazi[1], Jean Savoie[3], Priti Wanjara[2]

[1]Ecole de Technologie Superieure, Mechanical Engineering Department, Montreal, QC, Canada
[2]National Research Council Canada, Aerospace Manufacturing, Montreal, QC, Canada
[3]Pratt & Whitney Canada, Special Process Development Group, Longueuil, QC, Canada

Article published in Transactions of the Canadian Society for Mechanical Engineering (CSME), Volume 37, No. 1, pp.39-52, 2013.

3.1 Abstract

Tube hydroforming (THF) is a well-established process in the automotive industry and its application is being extended to the aerospace for manufacturing complex geometries. However, most of the alloys used in aerospace are high in strength and low in formability, which renders the application of THF more challenging. The objective of this paper is to present a method to increase the formability of an austenitic stainless steel. A multistep forming process was simulated through interrupted uniaxial tensile testing experiments to study the influence of the latter process on formability. The tensile test was divided into several deformation steps with a stress relief heat treatment after each forming step. The results indicated that the application of intermediate heat treatments considerably increased the formability of the stainless steel 321 alloy (SS321). Microstructure evolution as a function of deformation or heat treatment parameters was also investigated and revealed the formation of strain-induced martensite after the first deformation and heat treatment cycle without any deleterious effect on formability enhancement.

3.2 Introduction

Tube hydroforming is a forming process that uses a pressurized fluid, to plastically deform a given blank tube material into a desired shape. This technique presents many advantages compared to the traditional stamping and welding processes. It allows a lower weight to rigidity ratio as well as reducing the number of welds in an assembly which can considerably reduce the weight of the final product and also improve dimensional accuracy. Moreover, THF provides higher strength and surface quality in a part with a complex shape (Koç andAltan, 2001). It is also well known for its reduced tooling and assembly costs (Zhang, 1999). With all these advantages, THF has become a widely used forming process in many industries such as automotive, marine, sanitary and electronic (Lang et al., 2004). In the case of the aerospace industry, the application of THF is relatively new and very challenging. Indeed, due to the high strength of the materials used in aerospace and the complexity of the components, very high pressures are needed for hydroforming. On the other hand, the required tight tolerances and the limited formability of most aerospace alloys requires a very good understanding of material flow during the process to avoid premature failure or unacceptable thickness variations during THF.

The purpose of the present publication is on improving the hydroformability of tubes made of SS321, which is one of the most widely used aerospace alloys. To this end, intermediate heat treatments have been developed and performed between multiple deformation steps. Interrupted tensile tests (ITT) were used as a mean to replicate multistep forming processes (Anderson, 2010). Tensile testing has the advantage of being well implemented in industry, standardized and relatively easy in its procedure and data interpretation. The application of a specific intermediate heat treatment on deformed specimens should lead to material restoration and consequently to mechanical properties improvement (Golovashchenko andKrause, 2005). This paper focuses on the comparison of the formability performance and the microstructure to better understand microstructure evolution occurring along with formability enhancement.

3.3 Experimental procedure

3.3.1 Material

The austenitic SS321 alloy used for this study is a chromium-nickel austenitic grade stabilized by titanium to minimize intergranular chromium carbide precipitation. Due to its composition, this alloy cannot be hardened by heat treatment (Allen, 1969).

Tensile specimens were machined according to ASTM-E8 standard using laser cutting from a 1 mm thick rolled sheet. The samples were loaded in the rolling direction. The latter was selected after prior testing which did not reveal any significant difference in the mechanical properties of specimens cut in the transverse or 45 degrees directions. The multistep forming/heat treatment experiments were carried out for two starting material conditions: as-received (AR) and stress-relieved (SR).

3.3.2 Mechanical tests

Tensile tests were conducted at room temperature using a servo-hydraulic Materials Testing System 810 (MTS-810). Prior to testing, the width and thickness of each specimen were measured at three different locations along the 50 mm gauge length to determine the engineering stresses. Tensile tests were performed under displacement control mode with an equivalent strain rate of $0.25s^{-1}$ until rupture.

As illustrated in Figure 3.1, the tensile testing machine was equipped with both a laser video extensometer and the Aramis® digital image correlation (DIC) system. The laser video extensometer was placed behind the specimen to measure the global extension at the gauge length. The Aramis® (DIC) system is a non-contact optical deformation measurement system that is used to measure full 3D-strain fields. The system comprises of two CCD cameras, a trigger box and a high performance PC system. The two stereoscopic cameras of the system were placed in front of the specimen to capture local strains during testing. To measure

strains with the DIC system, the surface of the gauge length on each specimen must be covered with a high-contrast random speckle pattern. Thus, the front side of the specimen was painted with random speckles of black paint on a white background; while on the back side two pieces of laser tape were attached to mark the gauge length for the laser extensometer during testing. The elongation, tracked by the video-extensometer, was used to evaluate the deformation when plotting the global stress-strain curves thereby allowing stopping the test at any specific strain. The deformations captured by the DIC system were used to map the strain distribution over the specimen‘s gauge length area. The same data acquisition rate, 50 points per second, was used for the laser extensometer and the tensile load records. This allowed an easier and more accurate interpretation of the results. On the other hand, the DIC system triggered images at a frame rate of 3 images per second. At the end of the test, each DIC system image was computed and post-processed to extract the strain maps. The engineering stress was obtained by using the load data collected from the tensile testing machine during the test.

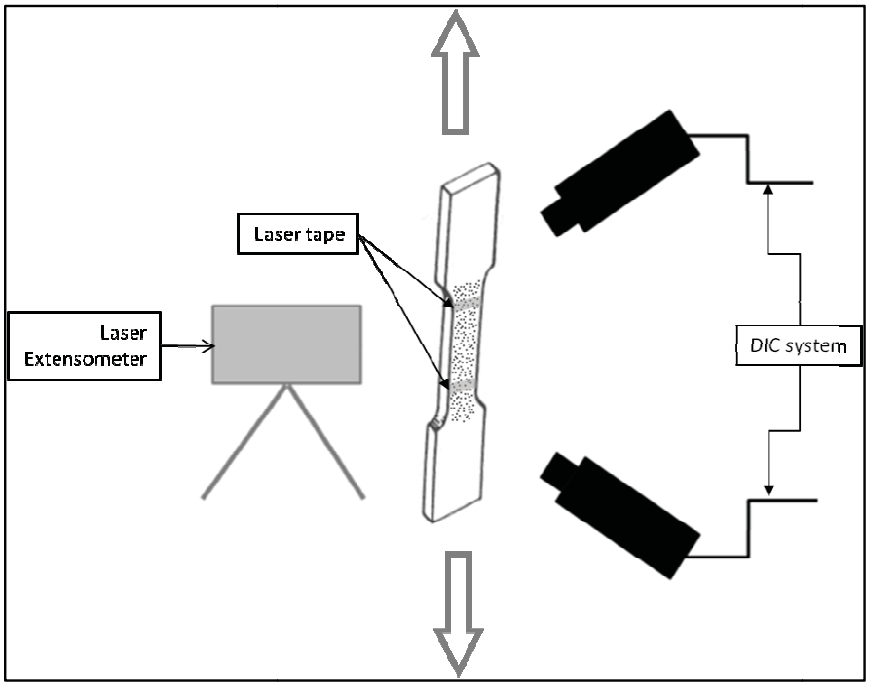

Figure 3.1 Schematic set up for interrupted tensile testing

3.3.3 Heat treatments

Stress relieving heat treatments were performed under secondary vacuum at 982°C for one hour followed by controlled cooling at 19°C/min down to 538°C and then air cooled to room temperature. The purpose of the stress relieving heat treatment (SR condition) is to increase the ductility of the material. It also stabilizes the microstructure against chromium carbide formation which may cause sensitization (Chandler, 1995).

3.3.4 Interrupted thermo-mechanical testing

Specimens were subjected to 1, 2 or 3 cycles of tensile testing up to the limit strain with a SR heat treatment performed between each tensile test. For each condition, final tensile loading was systematically performed up to rupture. The value of the limit strain was selected close to the onset of necking, which was determined via the strain distribution measurement using the DIC system. For each specimen, the thickness was measured at the end of tensile testing. All sequences of tensile tests C SR treatment cycles were performed twice to validate the repeatability of the experiments.

3.3.5 Microstructure evolution

The microstructures of the specimens in the AR, SR and cycles of deformation and SR treatments, were characterized by scanning electron microscopy (SEM) and electron backscatter diffraction (EBSD). The specimens were mechanically ground and then polished for 12 hours using a vibratory polisher (Vibro-Met) with colloidal silica. EBSD analyses were performed with a high-resolution Hitachi SU-70 field emission gun - scanning electron microscope (FEG-SEM) equipped with an Oxford-Channel 5 HKL acquisition system. The FEG-SEM was operated at 20 kV with a probe current of 14 nA. The specimens for the EBSD analysis were extracted from the center of the gauge length. Two different types of EBSD maps were acquired. The first one was performed over a large area of 1905 x 1425 μm^2 with a step size of 1µm. The second one was focused over 635 x 475 μm^2 with a step

size of 0.25 μm. The larger maps covered a sufficient number of grains for grain size and shape statistical calculations. The second maps were used to estimate the percentage of the different phases present in the microstructure. Both martensite and austenite were indexed. In both cases, the percentage of non-indexed points within the EBSD maps is between 2 % and 8 % depending on the specimens.

3.4 Results and discussion

3.4.1 Strain distribution up to rupture

The evolution of the major engineering strain distributed along the gauge length median axis during tensile testing of the AR condition is illustrated in Figure 3.2. Here, the strain distribution is plotted at various levels of the global strain ε_{global}, i.e., 4 %, 25 %, 40 %, 47 %, 50 % and 51.5 %. Up to 25 % strain, the curve indicates a very uniform strain distribution along the specimen. At 40 % global strain, the distribution of the local strain was still relatively uniform and the difference between the maximum and the minimum strain values was about 5 %. However, beyond 40 % strain, although no local instability was noticed along the gauge length, the above difference exceeded 10 %, indicating that strain localization has taken place. Thus, 40 % strain was considered as the maximum strain that can be applied safely without the risk of strain localization. In the present investigation, in order to maximize the cumulative applied strain for a given number of deformation-heat treatment cycles, the 40 % strain value was selected as the incremental deformation applied to the specimens after each heat treatment.

3.4.2 Cumulative stress-strain curves

The cumulative engineering stress-strain curves obtained from several interrupted tensile tests are shown in Figure 3.3. The initial state of the material before the first tensile test was the AR condition. In Figure 3.3, specimen A was pulled up to rupture. Specimen B was pulled up to 40 %, then unloaded and subjected to the SR heat treatment, and finally pulled

up to rupture. Specimen C was subjected to 2 cycles of tension: loading up to 40 % → unloading → SR heat treatment two times, and then reloading up to rupture.

The mechanical properties of the specimens at each step of the process are summarized in **Erreur ! Source du renvoi introuvable.**. The maximum strain reached at each step as well as the cumulative strain reached at the end of the process is also provided. The cumulative strain was calculated by considering the new dimensions of the specimen after each deformation step as input values. Note that the limit strains applied were not always exactly 40 %: The deviation from the target value of 40 % is less than 1 % and is due to the time difference between the reading of the actual strain by the laser extensometer and stopping of the test.

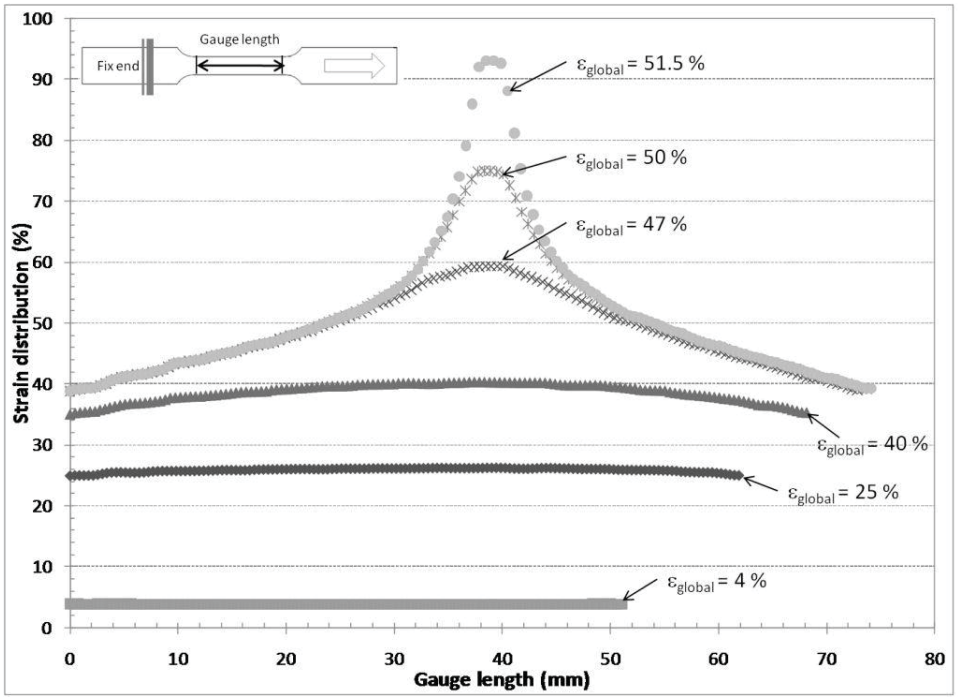

Figure 3.2 Strain distribution along an AR tensile sample up to rupture

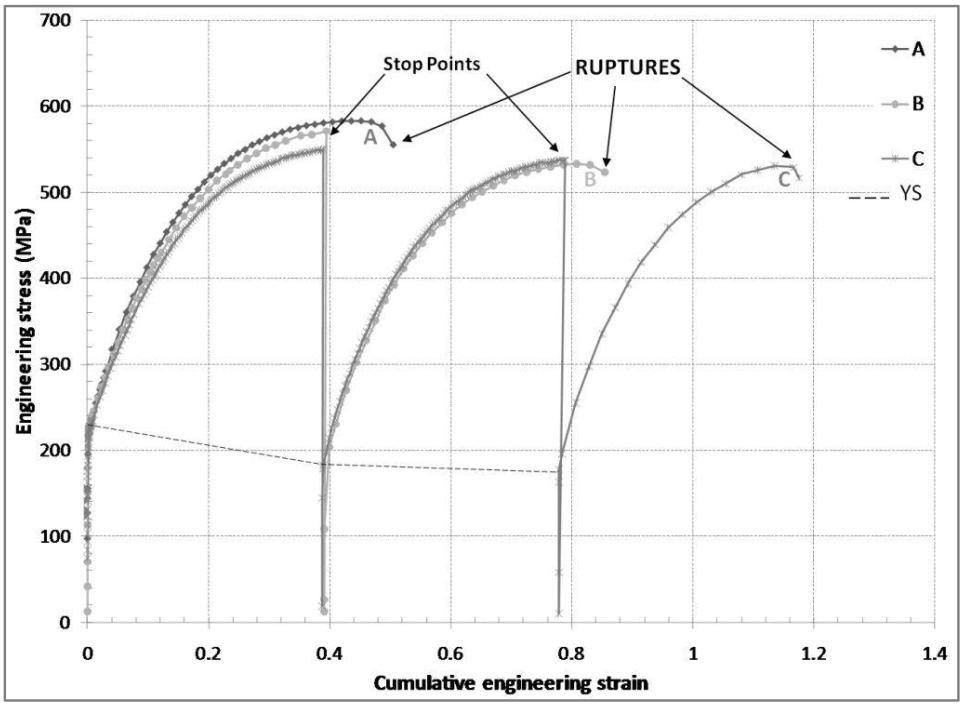

Figure 3.3 Cumulative stress-strain curves for 40% limit strain starting with AR condition

Table 3.1 Mechanical properties of the sample subjected to 40% limit strain in the AR condition

	Forming path	0.2% YS (MPa)	Strain applied or strain at rupture (%)	Cumulative strain	UTS (MPa)
A	AR	226	51.5	51.5	586
B	AR	229	39.5	39.5	-
	AR+40%+SR	181	47.8	87	534
C	AR	223	39.1	39.1	-
	AR+40%+SR	183	40	79.1	-
	AR+40%+SR+40%+SR	176	40	119.1	535

As illustrated in Figure 3.3, the application of the SR heat treatments allowed restoring the ductility of the material after each deformation step. Specifically, the elongation to rupture for the AR condition (specimen A), for one (specimen B) and two (specimen C) deformation-heat treatment cycles are similar: 40 to 47 %. It is worth noting that the cumulative strain

before rupture in specimen C exceeded 110 % indicating a higher formability of the alloy achieved using the proposed approach. In fact, according to the stress-strain curves, the specimens after each deformation and heat treatment cycle appear to start over as a new material. It can be noted from Table 1 that the conventional 0.2 % yield strength (YS) decreased from one deformation step to the next. In fact, the major drop in YS (from 226 MPa to 182 MPa) occurred after the first deformation and heat treatment cycle. Specifically, this drop was 48 MPa (21 %) and 40 MPa (18 %) for specimens B and C, respectively. However, the decrease in YS was only 4 % after the second deformation-heat treatment cycle; falling from 183 MPa to 176 MPa for specimen C. The significant decrease in YS after the first deformation-heat treatment cycle indicates that the AR specimens were not in the fully annealed condition and is thus a residual effect of the pre-existing work hardening in the material.

To confirm that the YS drop after the first step originates from the mechanical state of the AR specimens, the SR heat treatment was applied to the AR specimens before tensile testing. These specimens were identified as A_{SR}, B_{SR}, and C_{SR} and their testing conditions, cumulative strains and mechanical properties are displayed in Table 3.2 and Figure 3.4. The initial YS of specimens A_{SR}, B_{SR}, and C_{SR} is lower than that of specimens A, B, and C, confirming that the AR specimens were indeed in a work hardened state. As indicated in Figure 3.4 and Table 3.2, the overall decrease in YS for the specimens B_{SR} and C_{SR}, after the first and/or second deformation-heat treatment cycle, does not exceed 15 MPa compared to the initial value (specimen A_{SR}).

Table 3.1 and Table 3.2 also show that the same level of ultimate tensile strength (UTS) was reached in the last step for all cases. Specifically, the UTS does not significantly vary with either the starting material state or the number of deformation-heat treatment cycles.

Finally, in order to compare the global mechanical behavior of the material during the multistep forming process, the hardening equations at each step were determined. These equations, which represent the mechanical behavior of the material, are crucial inputs to the

finite element models for the hydroforming process. There are several mathematical expressions generally used to describe the strain hardening behavior of steels. In the case of SS321, it has been shown (Anderson, 2010; Saboori et al., 2010) that the Swift equation (Swift, 1952), as shown in Equation 3.1, gives a suitable description of the material behavior for hydroforming applications:

$$\sigma = K(\varepsilon_0 + \varepsilon_p)^n \tag{3.1}$$

With the true stress, K the strength coefficient, n the strain hardening coefficient, ε_P the plastic strain, and ε_0 a constant parameter that represents the strain hardening in the material prior to tensile testing (Datsko, 1966a). The appropriate hardening coefficients were obtained using the least square method.

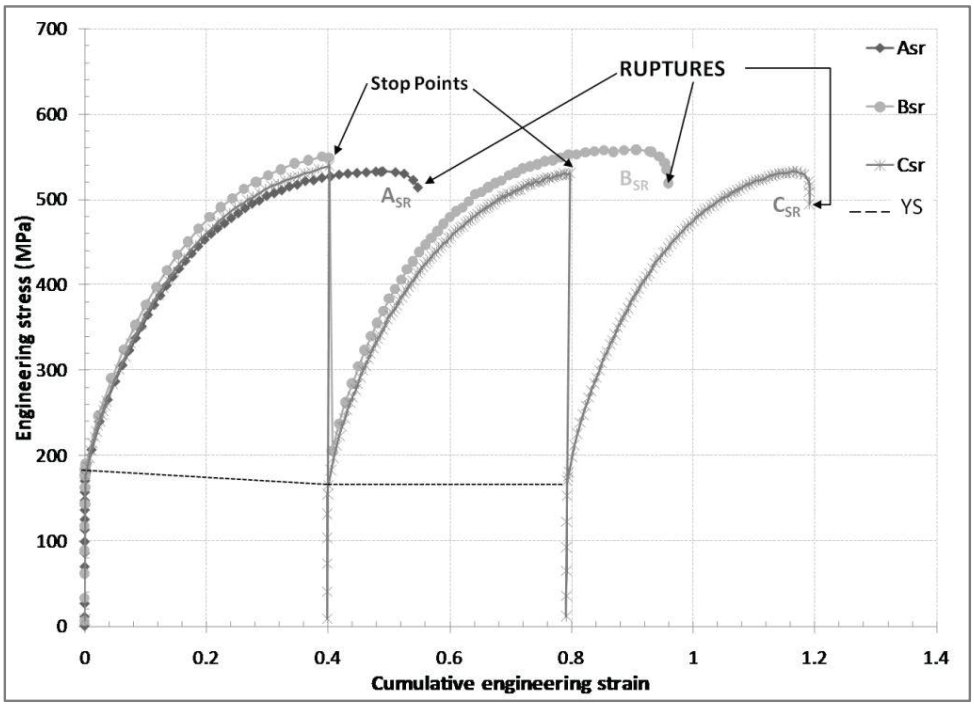

Figure 3.4 Cumulative stress-strain cures for 40% limit strain starting with SR condition

Table 3.2 Mechanical properties of the sample subjected to 40% limit strain in the SR condition

	Forming path	0.2% YS (MPa)	Strain applied or strain at rupture (%)	Cumulative strain	UTS (MPa)
A_{SR}	SR	190	51.7	51.7	573
B_{SR}	SR	190	40.1	40.2	-
	SR+40%+SR	176	56.6	96.7	560
C_{SR}	SR	180	40.4	40.4	-
	SR+40%+SR	169	40	80.4	-
	SR+40%+SR+40%+SR	166	39.9	120.3	535

Thus, the data from specimen C_{SR} were used to calculate the strength coefficient K as well as the strain hardening coefficient n for each deformation step (Table 3.3). The results indicate that the strain hardening coefficients are relatively similar throughout the process. Hence, the formability appears not to be affected by the multistep process. It can then be concluded that the intermediate heat treatments did not affect the global hardening behavior of the SS321, but only restored its ductility after each cycle of tensile test.

Table 3.3 Best fitted coefficients of the Swift hardening equation at each step of the multistep tensile test for C_{SR}

Swift $\sigma = K(\varepsilon_0 + \varepsilon_P)^n$	Specimen C_{SR} SR – 40% - SR – 40% - SR - R		
	Step 1	Step 2	Step 3
K	1367.8	1348.1	1341.5
n	0.5832	0.5770	0.5489
ε_0	0.0276	0.0252	0.0209

3.4.3 Microstructural analysis

The EBSD scan of the AR specimen is displayed in Figure 3.5. The grey levels, observed from one grain to the other in Figure 3.5a, correspond to the EBSD diffraction index quality distribution. The AR specimen exhibits a uniform and equiaxed microstructure with a

homogeneous grain size around 8 μm. A small amount of martensite (about 4.5%) was identified by EBSD in several grains of the AR specimen (Figure 3.5b).

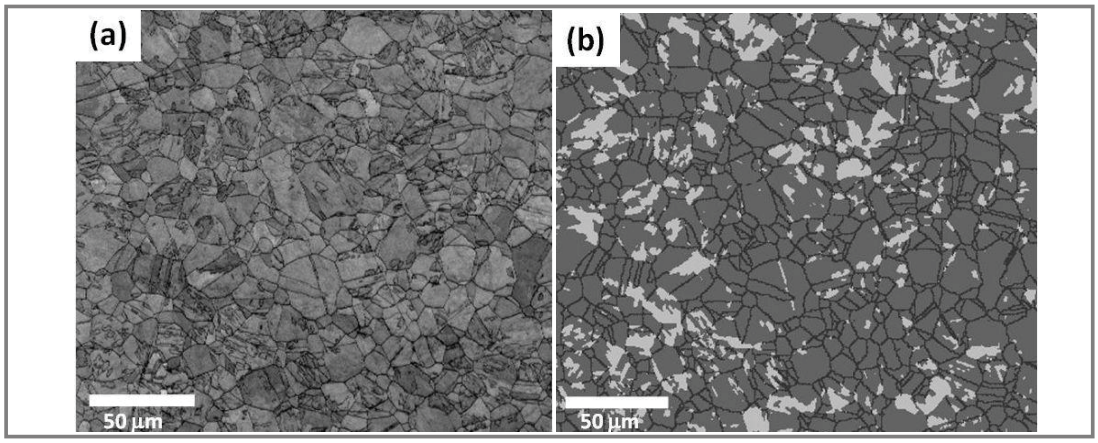

Figure 3.5 EBSD maps of a As-received (AR) specimen without deformation
(a) diffraction quality index image reflecting specimen microstructure;
(b) phases identification image: austenite in dark grey and martensite in light gray

SS321 as an austenitic stainless steel is susceptible to form strain-induced martensite (SIM) as shown in Figure 3.5b. The martensite phase tends to appear heterogeneously in certain austenitic grains as a result of intense cold working (Lecroisey andPineau, 1972; Olson andCohen, 1976). This confirms that the as-received material was not fully annealed and the work hardening observed on tensile test results is due to the cold rolling process of the sheet. The SIM transformation is well documented particularly for metastable austenitic stainless steels with low stacking fault energy such as SS 304 or SS 316 (Datsko, 1966b; Lecroisey andPineau, 1972; Lula, Parr andHanson, 1989; Mangonon Jr andThomas, 1970; Smaga, Walther andEifler, 2008). The formation of SIM is the result of plastic deformation which leads to a phase transformation from austenite into martensite. The transformation is enhanced by high strains, low strain rates, low temperatures and lower nickel contents (Angel, 1954b; Hecker et al., 1982; Peterson, Mataya andMatlock, 1997).

The relationship between the martensite formation and the formability is known to be a very complex phenomenon. In fact, in the case of uniaxial tension, Angel (1954b) and then

Hecker (1982) demonstrated that the ductility appears to depend on both the extent of martensite formation and the strain at which martensite forms. According to Rosen *et al.* (1972) and confirmed by Talyan *et al.* (1998), the ductility in metastable austenitic stainless steels is dominated by the formation and distribution of martensite over the tensile specimen and not by the total amount of martensite. There are two types of martensite formed sequentially from the austenite γ (FCC) : martensite ε (HCP) then martensite α' (BCC) (Mangonon Jr andThomas, 1970; Solomon andSolomon, 2010; Talonen et al., 2005). The volume percent of ε martensite compared to α' is considered as negligible above approximately 15% strain (Ghosh, Mallick andChattopadhyay, 2011; Rosen, Jago andKjer, 1972). In the present study only α' martensitic, i.e., the stable phase, was detected by EBSD which is in agreement with the above reference since the applied strain in this study is 40%.

The EBSD maps of the SR specimens are displayed in Figure 3.6-3.8. In Figure 3.6, the SR specimen has undergone no deformation. The SR specimen in Figure 3.7 has been deformed to 40% strain and then SR heat treated again. Finally, the SR specimen presented in Figure 3.8 has undergone 2 cycles of deformation and SR heat treatments. Figure 3.6a, 3.7a and 3.8a represent the microstructure of the specimens whereas Figure 3.6b, 3.7b and 3.8b represent the distribution of the phases. The specimens that have undergone only the SR treatment (Figure 3.6a) exhibit a uniform and equiaxed microstructure with average grain sizes very similar to that of the AR specimen presented in Figure 3.5a (7.9 ± 0.5 μm compared to 8.0 ± 0.2 μm); however, with the difference that no martensite was found in the microstructure after the SR treatment indicating that the SR heat treatment was able to transform all the martensite into austenite. Thus, in these conditions, the applied heat treatment is not only able to restore the mechanical properties of the material but also reverses the strain induced martensite into austenite without any effect on the grain size.

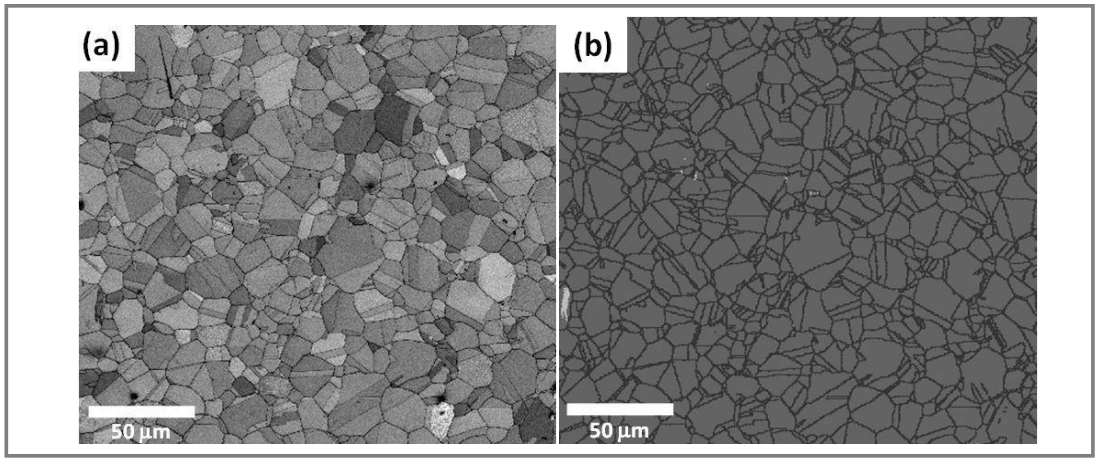

Figure 3.6 EBSD maps of a stress-relieved (SR) specimen without deformation
(a) diffraction quality index image reflecting the specimen microstructure;
(b) phases identification image: austenite in dark gray and martensite in light gray

The microstructure of the 'SR + 40% + SR' specimen shows a combination of some large grains next to smaller ones (Figure 3.7a). This indicates the possibility of recrystallization and /or grain growth due to the second SR heat treatment. In Figure 3.8a, after 2 cycles, i.e. 'SR + 40% + SR + 40% + SR', the grains are significantly bigger and more heterogeneously distributed than in the previous case (Figure 3.7a). Grain size distributions performed over 6670, 2150 and 2271 grains for the SR, 'SR+40%+SR' and 'SR+40%+SR +40%+SR' specimens, respectively are illustrated in Figure 9. Such numbers of grains are sufficient for proper statistical analysis since, generally, a minimum set of 200 grains and a step size ten times smaller than the grain diameter is recommended (Humphreys, 2004). The grain size distribution confirms that the SR specimen is mostly composed of relatively small grains whereas the introduction of a deformation step (SR+40%+SR) results in a wider distribution in size with a larger number of bigger grains. The analysis of the results in Figure 9 also indicates that the average size of the grains becomes even bigger when a second deformation step is included. Based on the above discussion, it can be stated that the level of applied prior deformation was high enough to onset some recrystallization and grain growth upon the application of the heat treatment.

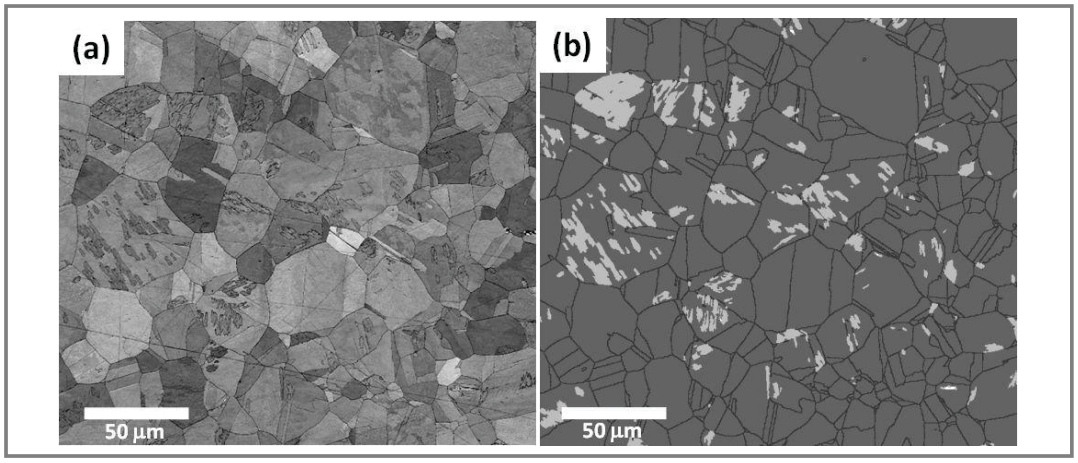

Figure 3.7 EBSD maps of a specimen that has undergone the sequence SR + 40% + SR (a) diffraction quality index image reflecting the specimen microstructure; (b) phases identification image: austenite in dark gray and martensite in light gray

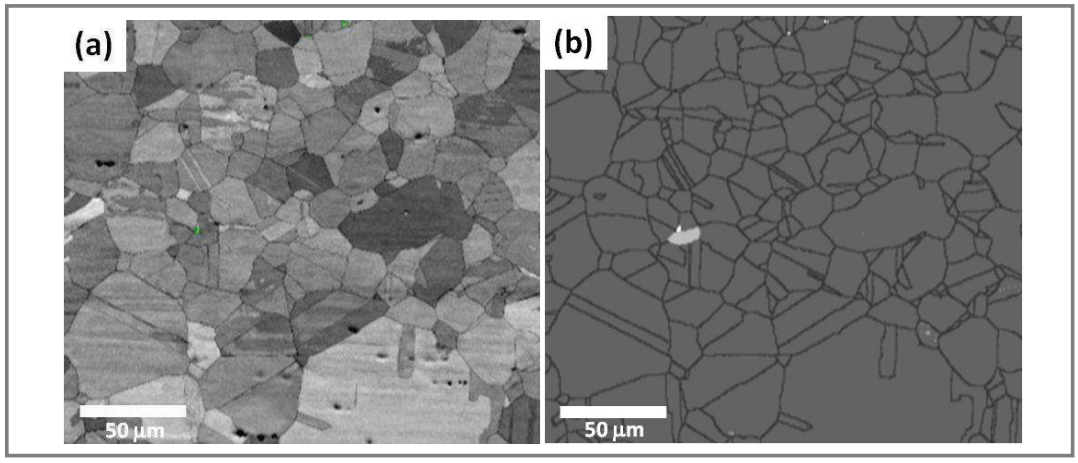

Figure 3.8 EBSD maps of a specimen that has undergone the sequence SR + 40% + SR + 40% + SR (a) diffraction quality index image reflecting the specimen microstructure; (b) phases identification image: austenite in dark gray and martensite in light gray

The phases present in the specimens are compared in Figure 3.6b, 3.7b, and 3.8b. Figure 3.6b corresponds to the SR specimen and shows a fully austenitic microstructure. In Figure 3.7b, it can be seen that in the 'SR + 40% + SR' specimen, some martensite is still present in several grains even after the SR treatment. Up to 7.5% of martensite was quantified by EBSD showing that the second SR heat treatment was unable to remove all the martensite in the

microstructure. However, in Figure 3.8b, the microstructure after 2 cycles of deformation and SR heat treatment is fully austenitic.

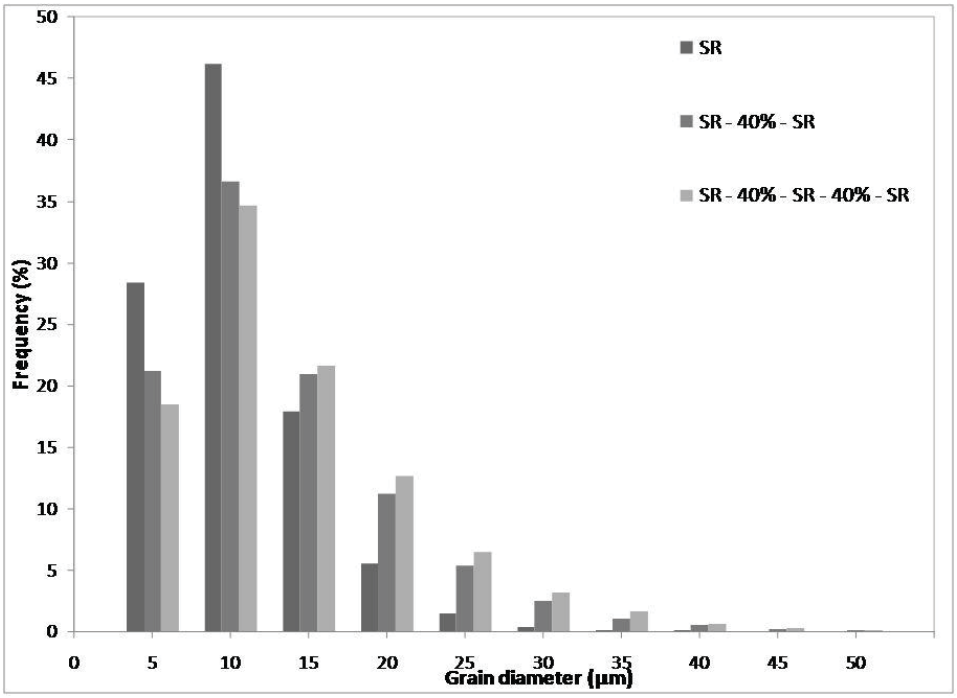

Figure 3.9 Grain sizes distribution measured statistically by EBSD for the three 'SR', 'SR + 40% + SR' and 'SR + 40% + SR + 40% + SR' on a population of 6670, 2150 and 2271 grains respectively

In order to confirm the amount of α'-martensite in the specimens identified by EBSD, some measurements were performed on the specimens using a Feritscope®, a device used to measure the δ-ferrite content on austenitic stainless steels welds. The measurement is based on the ferromagnetism of the α'-martensite compared to that of austenite (paramagnetic). It has been reported that this method can be used as a direct and reliable way to measure the α'-martensite content (Kumar et al., 2005; Talonen et al., 2005). Since the magnetic permeability of α'-martensite measured by the feritscope depends on the strain, it is necessary to convert the feritscope readings to actual α'-martensite through calibration

curves (Hecker et al., 1982; Kumar et al., 2005). According to Talonen *et al.* (2005), the actual martensite α'content can be evaluated with the following equation :

$$Martensite\ \alpha' content = 1.71\ \times Feritscope\ reading \quad (3.2)$$

The results in Table 3.4 indicate that the α' martensite content measured by EBSD and by the feritscope follow the same trend. The difference can be explained by the non-indexed points of the EBSD reading and the large step size used (0.25 microns) during EBSD mapping. It can also be explained by the fact that the Feritscope® estimates the volume of the material and not only a 2 D plan as is the case for EBSD.

The Feritscope® results confirm that after one cycle of deformation and SR heat treatment, the totality of the SIM cannot be reverted to austenite. This finding is in agreement with those reported by other authors. For instance, Ghosh *et al.* (2012) mention a residual volume percent of strain induced α'-martensite after annealing (800°C/1h) in an austenitic stainless steel with a composition very similar to the one investigated in the present study.

Table 3.4 Phases contents detected in different specimens using 2 methods: EBSD analysis and Feritscope

SPECIMENS	EBSD (%)			FERITSCOPE (%)
	Non-indexed	Austenite	Martensite	α'-Martensite
AR *(A)*	5.9	89.6	**4.5**	**3.83 ± 0.09**
SR *(A_{SR})*	1.76	98.16	**0.08**	**0.55 ± 0.01**
SR+40%+SR *(B_{SR})*	1.28	91.22	**7.5**	**4.94 ± 0.12**
SR+40%+SR+40%+SR *(C_{SR})*	1.03	98.92	**0.05**	**0.61 ± 0.03**

The presence of martensite after the second SR heat treatment in the specimen undergoing the 'SR + 40% + SR' sequence could indicate that 40% strain corresponds to an excessive deformation level. It would then induce relatively stable martensite that could not be totally reverted into austenite for the specific combination of temperature and time used in the present work. In other words, for a given heat treatment (time and temperature) there may be a maximum level of strain that should not be exceeded otherwise the amount of martensite

generated is too high to disappear after the same heat treatment. Interestingly, Grosse *et al.* (2006) have reported that some residual martensite can be found in specimens that have undergone warm drawing and subsequent solution annealing (1h at 1040°C).

However, this threshold effect is not confirmed by the results obtained in the specimen after two cycles ('SR+40%+SR+40%+SR) as no more residual martensite is found after the last heat treatment. This suggests that the sole application of the SR heat treatment is not sufficient to completely remove residual martensite and other microstructural factors such as grain size and grain to grain misorientation have to be considered. According to Solomon *et al.* (2010), the volume fraction of martensite formed is a function of the grain orientation and its relationship with its neighbors (i.e. local deformation conditions).

3.5 Summary and conclusions

The objective of this paper was to present a method to increase the formability of the austenitic stainless steel 321 for hydroforming applications. A multistep forming process that consisted of a series of tensile testing with a subsequent softening heat treatment was studied. A limit strain of 40% and stress relief heat treatments were applied to the tensile specimens. The applied stress relief heat treatment led to a major restoration of the properties, such that after each heat treatment step the yield stress of the material was recovered to its initial value. It was shown that with a judicious combination of forming and heat treatment cycles, very high levels of deformation can be reached through this approach. The importance of the initial state of the material was pointed out. Particularly, the as-received material was not in the fully annealed state and the microstructure contained some residual martensite. This martensite phase, which is most likely strain induced, may be removed by an appropriate heat treatment. However, some remaining martensite was observed after the SR heat treatment in the 'SR+40%+SR' specimen (but not in the 'SR+40%+SR+40%+SR'). Hence, a deformation threshold of 40% (not to be exceeded) cannot alone fully explain the stabilization of some strain induced martensite. Additional work is ongoing to better understand the governing mechanisms of martensite stabilization during thermo-mechanical processing. This is of

particular importance as the limit strain applied at each step has to be optimized to ensure complete microstructural recovery during multistep forming processes.

3.6 Acknowledgements

The authors would like to extend their thanks to the Natural Sciences and Engineering Research Council of Canada (NSERC), the Consortium for Research and Innovation in Aerospace in Quebec under the CRIAQ 4.6 project, the Fonds de recherche nature et technologies (FQRNT) and the Pierre Arbour foundation for their financial support. The authors are also grateful to Mr. Daniel Chiriac, Mr. Daniel P. Turner and Dr Jean-Charles Stinville for their assistance.

3.7 References

Allen, Dell K. 1969. *Metallurgy theory and practice*. Chicago: American Technical Society, 663 p.

Anderson, Mélissa. 2010. « Tube hydroforming of aerospace alloys : material characterization methods ». Montréal, Canada, École de technologie supérieure.

Angel, T. 1954b. « Formation of martensite in austenitic stainless steels ». *The journal of the Iron and Steel Institute* vol. 177, n^{o} Part 1, p. 165-174.

Chandler, Harry. 1995. *Heat treater's guide : practices and procedures for irons and steels*, 2nd. Materials Park, OH: ASM International, vii, 903 p.

Datsko, J. 1966a. *Material Properties and Manufacturing Processes*. New York, USA: Wiley.

Datsko, Joseph. 1966b. *Material properties and manufacturing processes*. New York: Wiley, 543 p.

Ghosh, S., P. Mallick and P. Chattopadhyay. 2011. « Effect of reversion of strain induced martensite on microstructure and mechanical properties in an austenitic stainless steel ». *Journal of Materials Science,* vol. 46, n^{o} 10, p. 3480-3487.

Golovashchenko, Sergey, and Al Krause. 2005. « Improvement of formability of 6xxx aluminum alloys using incremental forming technology ». *Journal of Materials Engineering and Performance,* vol. 14, n^{o} 4, p. 503-507.

Grosse, M., D. Kalkhof, M. Niffenegger and L. Keller. 2006. « Influencing parameters on martensite transformation during low cycle fatigue for steel AISI 321 ». *Materials Science and Engineering: A,* vol. 437, n° 1, p. 109-113.

Hecker, S., M. Stout, K. Staudhammer and J. Smith. 1982. « Effects of Strain State and Strain Rate on Deformation-Induced Transformation in 304 Stainless Steel: Part I. Magnetic Measurements and Mechanical Behavior ». *Metallurgical and Materials Transactions A,* vol. 13, n° 4, p. 619-626.

Hilkhuijsen, P., H. J. M. Geijselaers and T. C. Bor. 2012. « The influence of austenite texture on the martensitic transformation of an austenitic stainless steel ». *Journal of Alloys and Compounds*, n° 0.

Humphreys, F. J. 2004. « Nucleation in recrystallization ». In *Proceedings of the Second Joint International Conferences on Recrystallization and Grain Growth, ReX and GG2, SF2M, August 30, 2004 - September 3, 2004*. (Annecy, France), I Vol. 467-470, p. 107-116. Coll. « Materials Science Forum »: Trans Tech Publications Ltd.

Koç, Muammer, and Taylan Altan. 2001. « An overall review of the tube hydroforming (THF) technology ». *Journal of Materials Processing Technology,* vol. 108, n° 3, p. 384-393.

Kumar, B., B. Mahato, N. Bandyopadhyay and D. Bhattacharya. 2005. « Influence of strain-induced phase transformation on the surface crystallographic texture in cold-rolled-and-aged austenitic stainless steel ». *Metallurgical and Materials Transactions A,* vol. 36, n° 11, p. 3165-3174.

Lang, L. H., Z. R. Wang, D. C. Kang, S. J. Yuan, S. H. Zhang, J. Danckert and K. B. Nielsen. 2004. « Hydroforming highlights: sheet hydroforming and tube hydroforming ». *Journal of Materials Processing Technology,* vol. 151, n° Copyright 2004, IEE, p. 165-77.

Lecroisey, F., and A. Pineau. 1972. « Martensitic transformations induced by plastic deformation in the Fe-Ni-Cr-C system ». *Metallurgical and Materials Transactions B,* vol. 3, n° 2, p. 391-400.

Lula, R. A., J. Gordon Parr and Albert Hanson. 1989. *Stainless steel*, rev. Metals Park, Ohio: American Society for Metals, x, 173 p.

Mangonon Jr, P. L., and G. Thomas. 1970. « Structure and properties of thermal-mechanically treated 304 stainless steel ». vol. 1, p. 1587-1594.

Olson, G., and Morris Cohen. 1976. « A general mechanism of martensitic nucleation: Part I. General concepts and the FCC → HCP transformation ». *Metallurgical and Materials Transactions A,* vol. 7, n° 12, p. 1897-1904.

Peterson, S., M. Mataya and D. Matlock. 1997. « The formability of austenitic stainless steels ». *JOM Journal of the Minerals, Metals and Materials Society,* vol. 49, n° 9, p. 54-58.

Rosen, A., R. Jago and T. Kjer. 1972. « Tensile properties of metastable stainless steels ». *Journal of Materials Science,* vol. 7, n° 8, p. 870-876.

Saboori, M., H. Champliaud, J. Gholipour, A. Gakwaya, J. Savoie and P. Wanjara. 2010. « Analytical Evaluation and Finite Element Simulation of material Characteristics in Tube Hydroforming of Aerospace Alloys ». In.

Smaga, M., F. Walther and D. Eifler. 2008. « Deformation-induced martensitic transformation in metastable austenitic steels ». *Materials Science and Engineering A,* vol. 483-484, n° 1-2 C, p. 394-397.

Solomon, N., and I. Solomon. 2010. « Deformation induced martensite in AISI 316 stainless steel ». *Revista de metalurgia,* vol. 46, n° 2, p. 121-128.

Swift, H. W. 1952. « Plastic instability under plane stress ». *Journal of the Mechanics and Physics of Solids,* vol. 1, n° 1, p. 1-18.

Talonen, Juho, Pertti Nenonen, Gersom Pape and Hannu Hanninen. 2005. « Effect of strain rate on the strain-induced , &rarr -martensite transformation and mechanical properties of austenitic stainless steels ». *Metallurgical and Materials Transactions A: Physical Metallurgy and Materials Science,* vol. 36 A, n° Compendex, p. 421-432.

Talyan, V., R. Wagoner and J. Lee. 1998. « Formability of stainless steel ». *Metallurgical and Materials Transactions A,* vol. 29, n° 8, p. 2161-2172.

Zhang, S. H. 1999. « Developments in hydroforming ». *Journal of Materials Processing Technology,* vol. 91, n° 1-3, p. 236-244.

CHAPTER 4

PAPER 2: MECHANICAL AND METALLURGICAL EVOLUTION OF SS321 UNDER MULTISTEP PROCESS

M. Anderson[1,2], F. Bridier[1,3], J. Gholipour[2], M. Jahazi[1], P. Wanjara[2], J. Savoie[4], P. Bocher[1]

[1]Ecole de Technologie Superieure, Mechanical Engineering Department, Montreal, Canada
[2]National Research Council Canada, Aerospace Manufacturing, Montreal, Canada
[3]DCNS Research, DCNS Nantes-Indret, France
[4]Pratt & Whitney Canada, Special Process Development Group, Longueuil, QC, Canada

Article published in Journal of Materials Engineering and Performance.
ISSN: 1059-9495, 2016-02-05

4.1 Abstract

This paper examines the metallurgical evolution of AISI Stainless Steel 321 (SS321) during multi-step forming; a process that involves cycles of deformation with intermediate heat treatment steps. The multi-step forming process was simulated by implementing interrupted uniaxial tensile testing experiments. Evolution of the mechanical properties as well as the microstructural features, such as twins and textures of the austenite and martensite phases, was studied as a function of the multi-step forming process. The characteristics of the Strain Induced Martensite (SIM) were also documented for each deformation step and intermediate stress relief heat treatment. The results indicated that the intermediate heat treatments considerably increased the formability of SS321. Texture analysis showed that the effect of the intermediate heat treatment on the austenite was minor and led to partial recrystallization, whilst deformation was observed to reinforce the crystallographic texture of austenite. For the SIM, an Olson-Cohen equation type was identified to analytically predict its formation during the multi-step forming process. The generated SIM was textured and weakened with increasing deformation.

4.2 Introduction

Austenitic stainless steels are widely used for engineering applications due to their high strength combined with relatively good formability. Type 321 is an austenitic chromium-nickel stainless steel (SS) stabilized with a titanium addition of at least five times the carbon content. Manufacturing of SS321 typically involves multiple processing steps to attain the geometric dimensions, microstructure and mechanical properties required of the part. Consequently, the possibility of increasing the formability of SS321 through multi-step forming is of specific interest for a wide range of applications in the aerospace, automotive and power generation industries. This process is important for the manufacturing of complex parts requiring medium to high strain levels, such as in hydroforming.

In multi-step forming, the combination of plastic deformation and heat treatment raises the question of recrystallization occurrence. As with most Face Centered Cubic (FCC) metals with low Stacking Fault Energy (SFE), SS321 is prone to the formation of annealing twins that when present in the microstructure indicate that the alloy underwent sufficient mechanical deformation prior to heat treatment to induce recrystallization. Several mechanisms leading to the formation of annealing twins have been suggested (Dash andBrown, 1963; Fullman andFisher, 1951; Gleiter, 1969; Meyers andMurr, 1978), and, reasonably, they most likely result from accidents associated with the growth of recrystallized grains originating in a previously deformed material that possesses a high density of stacking faults (Cahoon, Li andRichards, 2009). Thus, analyzing the amount of annealing twins at different stages in the multi-step forming process may provide evidence for the possible occurrence of recrystallization.

Considering that the trend for 300-series Fe-Cr-Ni stainless steels shows suppression of the martensitic transformation temperature and, in turn the Strain Induce Martensite (SIM) with increasing nickel and chromium concentrations, the relatively low amount of nickel in SS321 is thus expected to facilitate a phase transformation from austenite to martensite during plastic deformation. This SIM tends to enhance work hardening and may significantly

modify the mechanical behavior of the material. SIM transformation is well documented, particularly for metastable austenitic stainless steels with low SFE, such as SS304 or SS316 (Gey, Petit andHumbert, 2005; Lula, Parr andHanson, 1989; Mangonon Jr andThomas, 1970; Ravi Kumar et al., 2010; Smaga, Walther andEifler, 2008). The relationship between SIM formation and formability improvement of the alloy is known to be a very complex phenomenon. In fact, in the case of uniaxial tension, the ductility appears to depend on both the extent of martensite formation and the strain at which martensite starts to form (Angel, 1954a; Hecker et al., 1982). It is then important to precisely document the evolution of SIM with the applied strain.

In the case of SS321, only a few authors have reported on this phenomenon (Chunchun, Gang andNg, 2004; Grosse et al., 2006; Leban andTisu, 2013). Also the transformation from austenite to martensite as a result of plastic strain was enhanced by low strain rates, low temperatures and lower nickel contents (Angel, 1954a; Durand-Charre, 1997; Meetham, 1981). Moreover, the martensite phase was reported to appear heterogeneously in certain austenitic grains after intense cold working (Olson andCohen, 1976; Ravi Kumar et al., 2010). It is noteworthy that there are actually two types of martensite formed sequentially: austenite γ(FCC) $\rightarrow$martensite ε(HCP) $\rightarrow$martensite α'(BCC), where the terms HCP and BCC refer to the Hexagonal Closed Packed and Body Centered Cubic crystal structures (Mangonon Jr andThomas, 1970; Solomon andSolomon, 2010; Talonen et al., 2005). The volume percent of ε-martensite compared to that of α'-martensite is considered negligible above approximately 15% strain (Ghosh, Mallick andChattopadhyay, 2011; Rosen, Jago andKjer, 1972).

In order to predict the amount of martensite generated during deformation, several equations relating the volume fraction of martensite and the plastic strain have been developed. The progress observed has been summarized by Peterson (1997). Specifically, Angel (1954a) and then Olson and Cohen (1975) developed a model for the kinetics of SIM nucleation based on a shear-band intersection mechanism. This model has been recently applied by Talonen *et al.* (2005) on SS304 and SS301LN. On the other hand, Ramirez (1992) and Tsuta (1993)

suggested an alternative model, also resulting from the Olson and Cohen equation, that described the kinetics of α'-martensite transformation for a material subjected to complex strain paths. Grosse (2006) used the latter model in his study of martensite transformation during low cycle fatigue for SS321 and adapted it for low volume fractions of martensite (less than 30%). In the present study, both models (Olson-Cohen and Tsuta-Grosse) were implemented to describe the SIM measurements as a function of the cumulative strain because no parameters in these models are currently available for the case of a multi-step forming process:

The Olson-Cohen equation is as follows:

$$X_M = 1 - \exp[-\beta[1 - \exp(-\alpha \times \varepsilon)]^n] \tag{4.1}$$

where X_M is the α'-martensite volume fraction, α and β are temperature-dependant constants, n is a fixed exponent evaluated at 4.5 for austenitic stainless steels (Olson andCohen, 1975) and ε the true strain. The α parameter describes how fast shear-bands form with strain and depends on the SFE. The β parameter is proportional to the probability that a shear band intersection generates a α'-martensite embryo: this parameter is strongly related to the chemical driving force of the alloy.

Tsuta-Grosse equation is developed as follows:

$$X_M = A \times \varepsilon^B \times \exp\left(-BQ/T\right) \tag{4.2}$$

where A and B are parameters that depend on the material conditions, Q is the activation energy for initiating the reaction and T is temperature.

The crystallographic orientation relationship between austenite and SIM after cold rolling has been widely studied and was found to be of the Kurdjumov-Sachs (K-S) type (Kurc-Lisiecka, Ozgowicz andRatuszek, 2012; Ray et al., 1994; Venables, 1962). This implies that the formed {110} martensite plane is parallel to the parent {111} austenite plane and the [111]

martensite direction is parallel to the [101] direction of the austenite (Kumar et al., 2006; Kurdjumow andSachs, 1930). Texture evolution in austenitic stainless steels during uniaxial tensile deformation was studied by some authors who reported that two strong fiber textures belonging to the <111> and <100> directions parallel to the tensile direction were formed (Barbier et al., 2009; Jiménez andFrommeyer, 2010). However, the texture evolution of both austenite and the generated martensite developed during deformation of SS321 has not been reported, especially in the case where intermediate heat treatments are introduced between the deformation steps. Hence, the purpose of the present work is to observe the changes in the mechanical properties and metallurgical characteristics of the material when multi-step forming is conducted, giving the opportunity to document the associated SIM in the alloy subjected to this specific process.

4.3 Experimental procedure

4.3.1 Material

The composition, in weight percent (wt. %), of the 0.9 mm thick austenitic SS321 sheet material used is given in Table 4.1. The microstructure of the as-received sheet is presented in Figure 4.1. The average equiaxed austenitic grain size is about 8 μm. All specimens were subjected to a stress relief heat treatment (982°C for 1h) prior to testing to ensure that the initial material conditions were similar.

Table 4.1 Chemical composition of the as-received SS321 sheet

Element	Fe	Ni	Cr	Si	Al	Ti	Mn	S	P
Wt. %	67.60	8.50	16.63	0.38	0.05	0.20	1.30	0.10	0.001

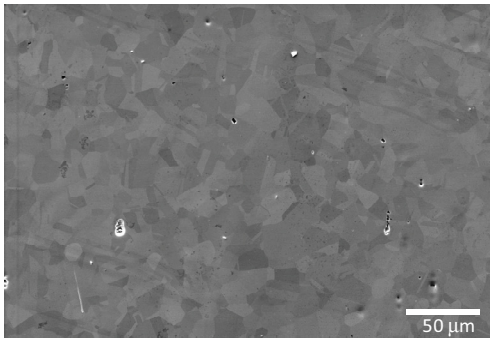

Figure 4.1 SEM image (SE mode)
of SS321 in the as-received condition

4.3.2 Mechanical tests

To emulate a multi-step forming process, tensile tests were conducted at room temperature with a Kammrath&Weiss® micro testing machine using flat micro-tensile specimens with a 15 mm gauge length and 4 mm width. It is noteworthy that all specimens were manufactured with Electro Discharge Machining (EDM). The strain was applied in the Rolling Direction (RD) of the sheet and measured with a mechanical extensometer that had a maximum displacement range of 1 mm. By contrast, the load data were collected through a microprocessor interfaced with the acquisition recording system of the tensile testing machine. Tensile loading was performed under displacement control mode with a strain rate of 0.03 s^{-1} up to a limit strain of 40%. Due to the limitation of the micro-tensile testing machine in terms of the stroke, a total cumulative strain of 100% was delimited for the experiments. In order to study the strain induced martensite evolution, the tensile tests were interrupted at specific strain levels to allow measurements at each stage. Thereafter, tensile loading was then continued up to the limit strain of 40%, at which point a heat treatment step was undertaken. Figure 4.2 shows the set-up of the tensile tests.

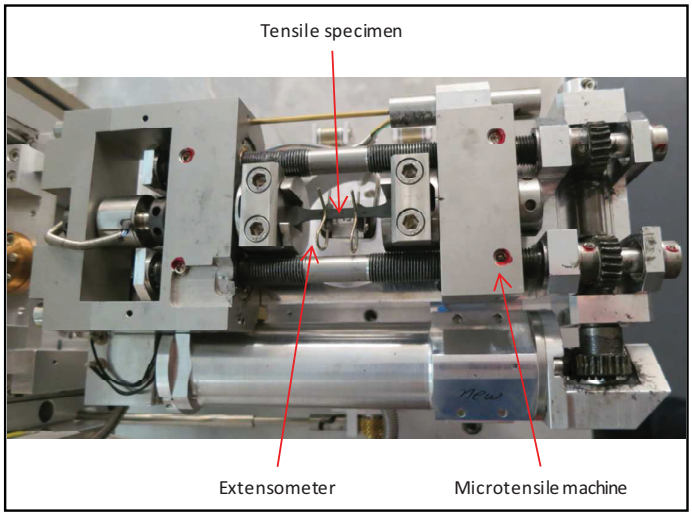

Figure 4.2 Set-up for the uniaxial micro tensile test

4.3.3 Heat treatments

The initial and intermediate heat treatment consisted of holding the specimen for one hour under a secondary vacuum at 982°C followed by rapid cooling at a rate ≥ 19°C/min to prevent chromium carbide formation, which may cause sensitization in SS321 (Chandler, 1995). Considering that SS321 can only be hardened by cold working, the heat treatment conducted was a stress relief (SR) to provide annealing of the material (static recovery and/or recrystallization). This results in a significant reduction in the yield stress with a concomitant increase in the ductility.

4.3.4 Interrupted thermo-mechanical testing

Table 4.2 describes the experimental design of the interrupted thermo-mechanical tests. As mentioned, each specimen was subjected to an initial SR heat treatment. It is important to mention that the generic term “strain” in this paper refers to the engineering strain. To support documenting the deformation evolution, a set of four specimens was deformed to 25% strain (i.e. step 0) without any subsequent SR heat treatment. For the interrupted thermo-mechanical tests, the tensile tests were pursued up to the limit strain of 40% (Step 1).

The SR heat treatment was performed (Step 1-SR) before the next cycle of tensile loading up to the limit strain of 40% (Step 2) with a SR heat treatment performed (Step 2-SR) and finally the last loading step up to 20% (Step 3) was applied. It is noteworthy that the limit strain value of 40% was selected to be close to but less than that for the onset of necking (Anderson, 2013). The methodology applied for the tests involved starting with four identical specimens and then retaining one sample after each deformation step for metallurgical analysis. Thus, the first sequence of the process (step 1: SR + 40%) was performed on four samples, then the second step (step 2: step 1 + SR + 40%) on 3 samples and finally the last step (step 3: step 2 + SR + 20%) on 2 samples. Final tensile loading was performed up to 20% strain to reach a total cumulative strain of 100%.

Table 4.2 Design of experiments for the interrupted tensile tests

	Condition	Number of Samples	Cumulative Engineering Strain	Intermediate heat treatments
Start	SR	4	-	-
Step 0	SR + 25%	4	25%	-
Step 1	SR + 40%	4	40%	-
Step 1-SR	SR + 40% + SR	3	40%	1x
Step 2	SR + 40% + SR + 40%	3	80%	1x
Step 2-SR	SR + 40% + SR + 40% + SR	2	80%	2x
Step 3	SR + 40% + SR + 40% + SR + 20%	2	100%	2x

4.3.5 Microstructure and texture analysis

To examine the microstructure, metallographic preparation was performed using automated grinding and polishing techniques, followed by vibratory polishing (Vibro-Met) with colloidal silica for 12 hours to render surfaces suitable for Electron BackScatter Diffraction (EBSD). The microstructures were examined in the central region of the gauge length of the tensile specimen obtained from each step in the interrupted thermo-mechanical process, using a high-resolution Hitachi SU-70 Field Emission Gun - Scanning Electron Microscope (FEG-

SEM) equipped with an Oxford - Channel 5 HKL EBSD acquisition and analysis system. The FEG-SEM was operated at 20 kV with a probe current of 14 nA. Two different types of EBSD maps were acquired. The first one was performed over a relatively large area of 1905 x 1425 μm^2 with a step size of 1 μm to cover a sufficient number of grains for statistical calculations (grain size distribution, fraction of twins, etc.) of the austenitic grains. A minimum of 2000 grains were sampled in these larger maps. The annealing twins were defined in the Channel 5 software as having a misorientation of 60° along the <111> axis with a maximum deviation of 5°. The amount of twins corresponded to the linear percentage of special boundaries (60° <111>) in relation to the overall length of boundaries. Grain size distribution analyses were performed based on the EBSD maps following the ASTM E2627-13 standard. The grains were reconstructed using a critical misorientation angle of 15° between adjacent pixels, and all grains with an area smaller than 8 pixels were considered as noise and removed before the data evaluation. In order to reveal the subgrain structure, grain boundaries and subgrain boundaries were plotted as black lines: an arbitrary deviation of 5° was used as subgrain criterion. The grain size distributions were presented by cumulative plots. A second type of EBSD map was recorded over an area of 635 x 475 μm^2 with a step size of 0.25 μm to study both the austenite and martensite textures. The austenite texture resulting from both maps (large and small areas), when compared, was identical. In other words, the findings obtained in the small section of the sample were representative of the global texture. The pole figures reported in this work correspond to {100} and {111} planes of the austenite phase and the {100} and {110} planes of the strain induced martensite.

4.3.6 Measurement of the α'-martensite content

The α'-martensite content was measured using a Feritscope® (Model MP3C, Helmut Fisher GmbH), a non-destructive inspection (NDI) device based on a magnetic induction method that was originally designed to measure the δ-ferrite content in austenitic stainless steels welds. However, since all magnetisable structures are measureable with the Feritscope® instrument, ferromagnetic α'-martensite can be differentiated from paramagnetic austenite in

SS321. In this magneto-inductive test methodology, an electromagnetic field generated by a coil interacts with the magnetic constituents in the specimen, namely martensite in SS321. The magnetization of the martensite phase induces an electrical potential difference in the second coil and this output voltage is linearly related to the magnetic permeability of the specimen, which can then be related to the martensite content through the rule of mixtures (Beese andMohr, 2009; Fischer, 2006). It has been reported that this method is a direct and reliable way to quantify low amounts (e.g. between 0.1% and 40%) of α'-martensite (Talonen, Aspegren andHänninen, 2004; Talonen et al., 2005). To obtain a quantitative measure of the α'-martensite volume fraction from its magnetic permeability, Talonen et al.(2004) converted the measured voltage (feritscope readings) to an actual α'-martensite content in austenitic stainless steel using the following calibration equation:

$$Martensite\ \alpha' content = 1.71 \times Feritscope\ reading \quad (4.3)$$

In the present work, five Feritscope readings (output voltage) were measured on the surface of each tensile specimen along the gauge length; the readings were then converted (using Eq.4.3) to actual α'-martensite contents. The minimum, maximum, and average values of the α'-martensite content are reported for each tensile specimen.

4.4 Results

4.4.1 Mechanical properties

4.4.1.1 Cumulative stress-strain curves

The average cumulative engineering stress-strain curve, obtained from the interrupted tensile tests, is presented in Figure 4.3. The specimens that were cycled– pulled to the 40% limit strain, unloaded, and subjected to the SR heat treatment– twice before finally being reloaded to a strain of 20%, gave a total cumulative engineering strain of 100%. The cumulative strain was calculated by considering the "altered" dimensions of the specimen after each

deformation step as input values. The mechanical properties, i.e. the conventional 0.2% yield strength (YS) and the maximum strength reached at the limit strain (i.e. limit stress) of the specimens at each step of the process are listed in Table 4.3. It is important to note that it was a challenge to experimentally determine a value for the Young's modulus (E) due to the limited elastic range of SS321 and the equipment constraints that limited the number of data acquisition points obtained in this region of the stress-strain curves. As a consequence, the obtained results were not found to be reliable and, as such, were not used. Instead, the YS was calculated based on the Young's modulus of SS321 (184.5 GPa) that was measured previously by the current authors from tensile curves of macroscopic samples (Anderson et al., 2010).

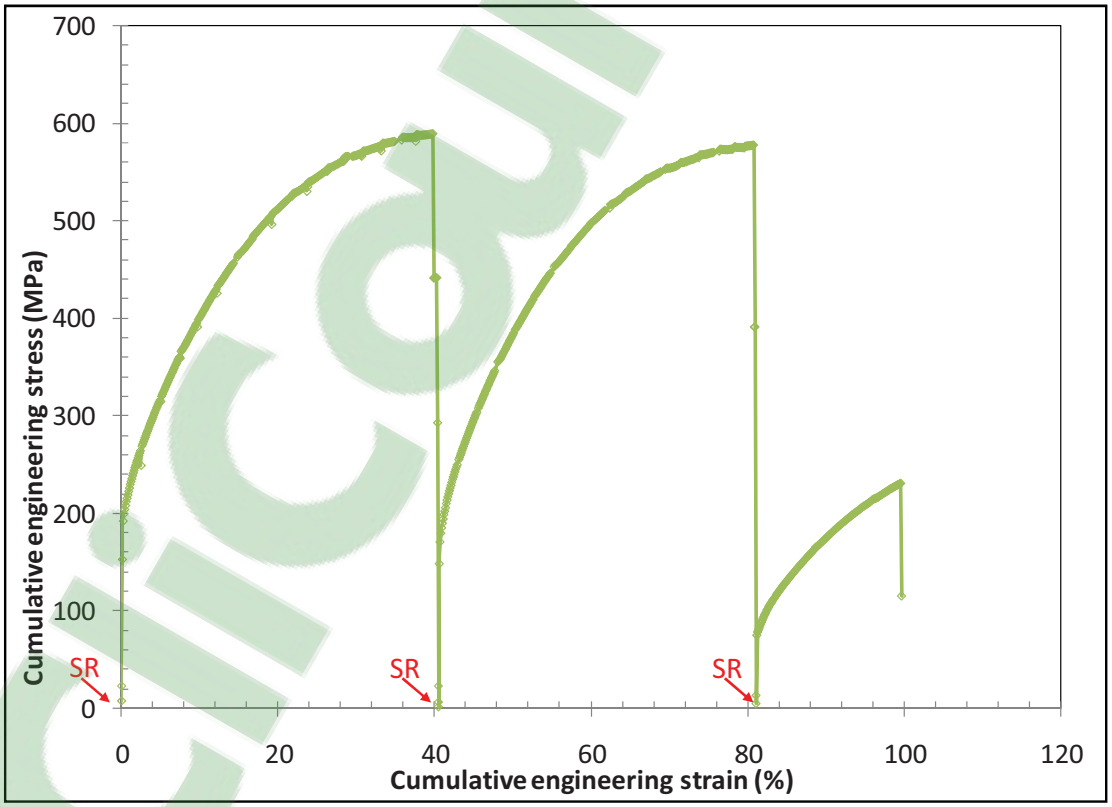

Figure 4.3 Average cumulative stress-strain curve for specimens subjected to interrupted tensile testing to simulate multistep forming. (Arrows show the SR heat treatment steps)

Table 4.3 Mechanical properties of specimens subjected to interrupted tensile testing

Properties	Step 1 (40% limit strain)		Step 2 (40% limit strain)		Step 3 (20% limit strain)	
	Average (4)	SE*	Average (3)	SE*	Average (2)	SE*
YS, MPa	193	0.58	187	16.22	157	0.85
Limit Stress**, MPa	588	0.74	583	5.89	464	0.49

*SE, the Standard Error, is given by $SE = SD/\sqrt{N}$, where SD is the Standard Deviation and N is the sample size, as given by the number in parentheses next to the average value of each property for steps 1, 2 and 3

**Maximum strength value reached when the test was interrupted and the specimen was unloaded.

Examining the stress-strain curves in Figure 4.3, it is evident that tensile loading at each step resulted in a similar mechanical response, though; a clear drop in the YS is obvious from the data presented in Table 4.3. The same level of deformation was reached without early necking, confirming that the SR heat treatment sufficiently restored the formability of material. The YS decreased with the number of heat treatment cycles. After the first loading and SR heat treatment cycle, the YS decreased by 3% (from ~193 MPa to ~187 MPa). When, an additional loading and SR heat treatment cycle was performed, the YS reduced by 16% (from ~187 MPa to ~157MPa), such that the overall decrease in the YS was 19% at 100% cumulative strain. This decrease in the YS is related to the improvement of the material ductility. For the limit stress, only the values obtained for steps 1 and 2 can be compared (due to the equivalent limit strain applied), since the last (third) step was intentionally stopped at 20% strain. The same level of limit stress (~585MPa) was reached in both steps 1 and 2 with a variation of less than 1%.

4.4.2 Microstructural analysis

4.4.2.1 Grain distribution

The analysis of the distribution in the austenite grain size, as illustrated in Figure 4, was performed based on the EBSD maps. It is noteworthy that for this analysis the number of grains sampled for each specimen, as listed in Table 4.4, should be suitable for a reliable statistical analysis, considering that typically a minimum set of 200 grains and a step size ten

times smaller than the grain diameter is recommended. Figure 4.4 relates the effect of both the deformation and heat treatment on the grain size evolution through an understanding of cumulative grain size distributions. In particular, the two curves left of the "reference" curve of the ‘SR’ material condition present the effect of deformation. It can be observed that as the applied strain increases, the austenite grain size decreases, as evidenced from the shift of the grain size distribution towards lower grain size values. During deformation, the grains are dislocated and their shape is changing due to local deformation gradients (triple points) and martensite formation. Thus, the microstructure is fragmented as the plastic strain increases and the average grain size decreases. When the SR heat treatment step is introduced, the average grain size increased and the cumulative distribution of the ‘SR + 40% + SR’ material condition significantly shifted to larger grain sizes. Specifically, the increase in the grain size observed for the ‘SR + 40% + SR’ material condition (having a full cycle of deformation and heat treatment) relative to the ‘SR’ material can be related to two phenomena: a recrystallization and a phase transformation from martensite to austenite. In fact, at the end of the first deformation, step1 (SR + 40%), the microstructure is mostly composed of severely deformed small austenite grains and martensite. After the SR heat treatment (SR+ 40% + SR), a new microstructure is generated with equiaxed austenitic grains, which are larger than the initial grains (SR). The level of deformation introduced (low compared to cold rolling) is known to produce larger grains due to the limited nucleation rate during recrystallization. When a second cycle is added (SR + 40% + SR + 40% + SR vs. SR + 40% + SR), the grain growth is maintained even if it is at a lower rate. The grain size increase from ‘SR’ to ‘SR + 40% + SR’ is 3 times greater than the grain growth observed from ‘SR + 40% + SR’ to ‘SR + 40% + SR + 40% + SR’ suggesting a quasi-stationary state of the microstructure once the first cycle is completed.

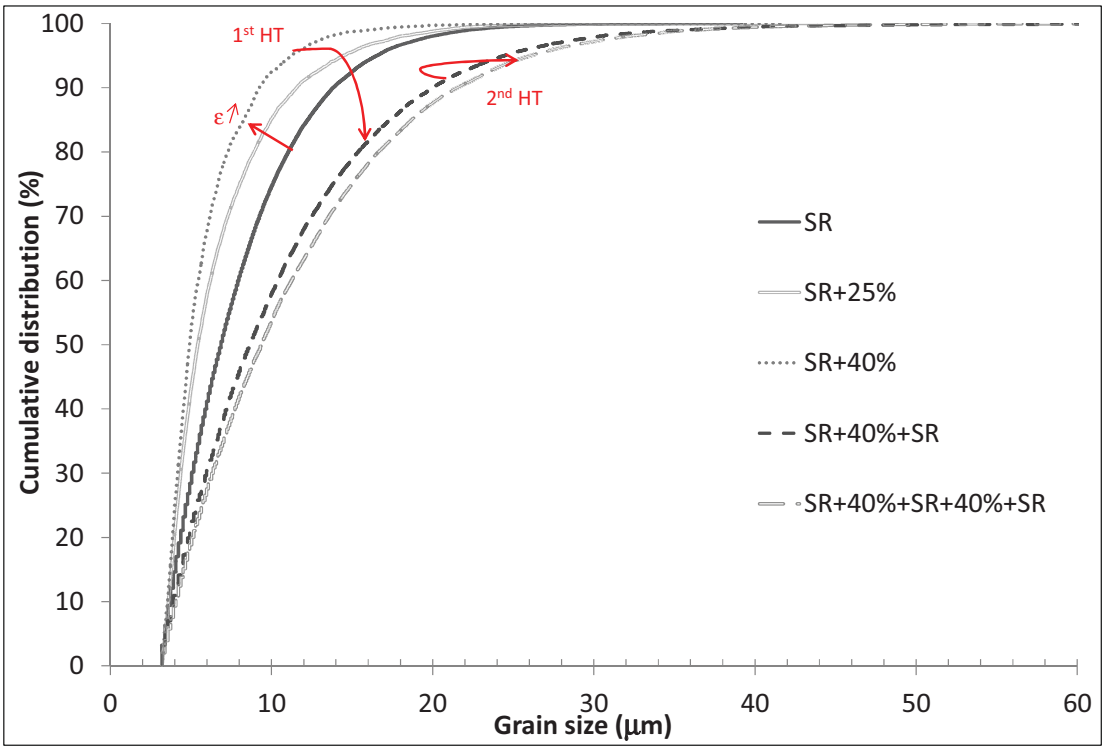

Figure 4.4 Cumulative distribution of grain size measured statistically by EBSD in the five specimens: 'SR', 'SR+25%', 'SR+40%+SR' and 'SR+40%+SR+40%+SR

Table 4.4 Grain population for statistical analyses of the grain size distribution

Specimens	SR	SR+25%	SR+40%	SR+40%+SR	SR+40%+SR+40%+SR
Number of grains	6670	6518	4237	2150	2271

4.4.2.2 Distribution of annealing twins

The distribution of the annealing twins was studied in order to document the effectiveness of recrystallization during the SR heat treatment. Figure 4.5 displays the fraction of twins at each stage of the multistep process on top of the cumulative engineering stress-strain curve and Table 4.5 details the fraction of twins for each step. Figure 4.6 shows the austenitic

matrix with the distribution of grain boundaries as black lines and 60°<111> twins as red lines. The amount of annealing twins in the SR sample is 44% and decreased to about 5% with deformation (no significant difference was observed between the 25% and 40% deformation conditions). The SR heat treatment applied at the beginning of the tests generated a large number of twins in the specimen (most likely the maximum). The presence of twins in the matrix usually provides a random texture as each twin changes the orientation of the grain. Specifically, stainless steels generally display weak-to-medium textures due to the slow migration of the large angle boundaries. This ensures that many orientations are available for plastic deformation and some of these can plastically deform earlier than others. As observed in Figure 4.6, when the applied strain is increased, it is increasingly difficult to distinguish twins as well as grains boundaries in the EBSD maps. When the heat treatment was applied, the amount of twins increased from 5% in the 'SR+40%' condition to 33% in the 'SR+40%+SR' condition, which provides evidence of some major grain boundary displacement. Likewise, when the complete cycle was repeated as in 'SR+40%+SR+40%+SR' condition, the percentage of twins was almost the same as in step 1-SR (36%). However, the amount of twins following a SR heat treatment after deformation (step 1-SR or 2-SR) remained below that in the starting SR material condition implying that the recrystallization was partial. In other words, the non-recrystallized zones (calculated as the ratio between the percentage of twins after the first and second completed cycles and the starting percentage of twins in the SR condition) was evaluated between 18% and 25%, depending on the number of cycles.

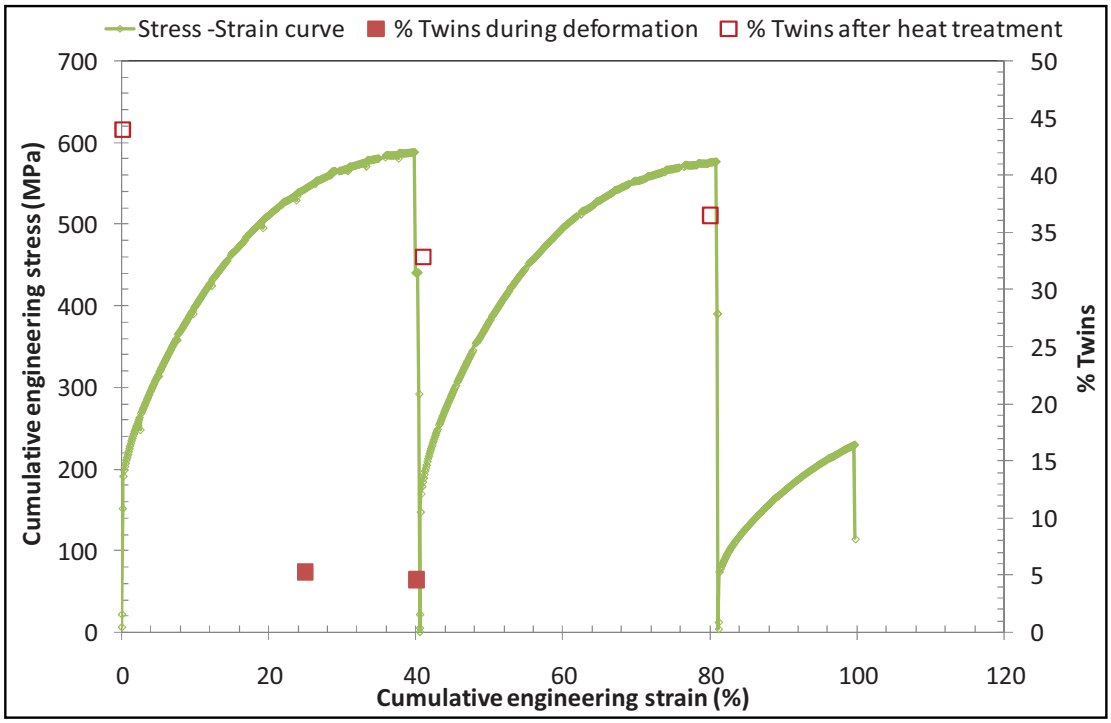

Figure 4.5 Fraction of twins superimposed on the average cumulative engineering stress-strain curve acquired through interrupted tensile testing

Table 4.5 Fraction of twins in specimens subjected to interrupted tensile testing

Specimens	SR	SR+25%	SR+40%	SR+40%+SR	SR+40%+SR+40%+SR
Twins fraction (%)	44.0	5.3	4.6	32.9	36.5

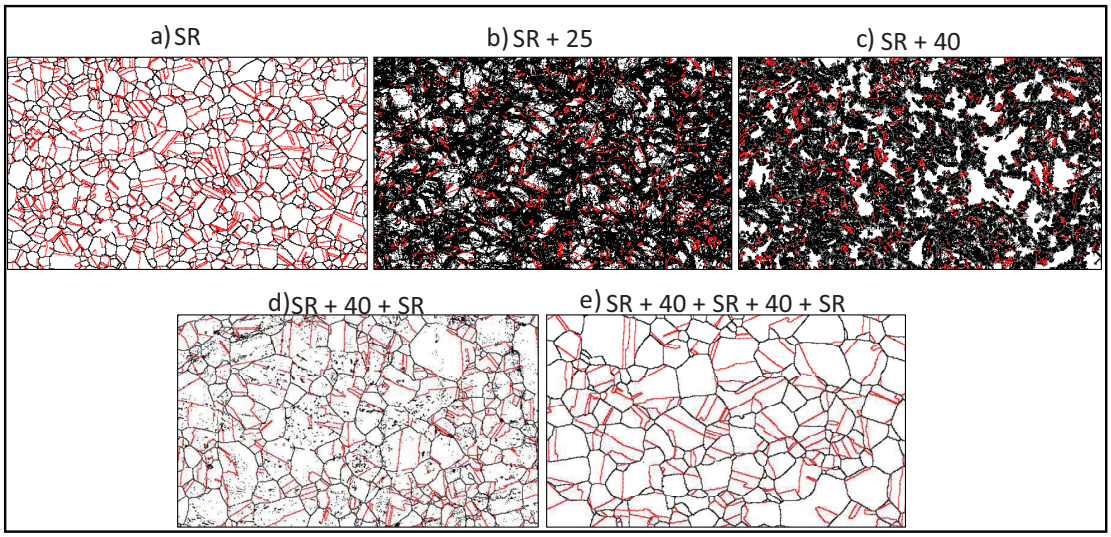

Figure 4.6 Austenitic matrix shown with a distribution of grain boundaries (black lines) and annealing twins (red lines)
a) SR, b) SR+25%, c) SR+40%, d) SR+40%+SR and e) SR+40%+SR+40%+SR

4.4.2.3 Austenitic texture

Figure 4.7a to c show the austenite {100} and {111} pole figures for the SR material and for the specimens deformed at 25% and 40% strain. The horizontal direction corresponds to the tensile direction and is parallel to the initial rolling direction (RD). On the pole figures of austenite, a weak <111> and <100> fiber along the tensile direction was found, the <100> fiber being weaker than the <111> one. A maximum MUD (Multiple of Uniform Distribution) of about 2.2 for <111> was found in the RD at 0% deformation and increased up to about 6 after 40% strain. The increase of the <100>//RD fiber was less significant (from 1.8 to 2.7 respectively). The samples that underwent one (SR+40%+SR) and two (SR+40%+SR+40%+SR) complete cycles are shown in Figure 4.7d and e, respectively. When the heat treatment was applied, the sharpness of both fibers slightly decreased (from 6 to 5.1 in the <111> pole figures and from 2.7 to 2.1 in <100> pole figures).

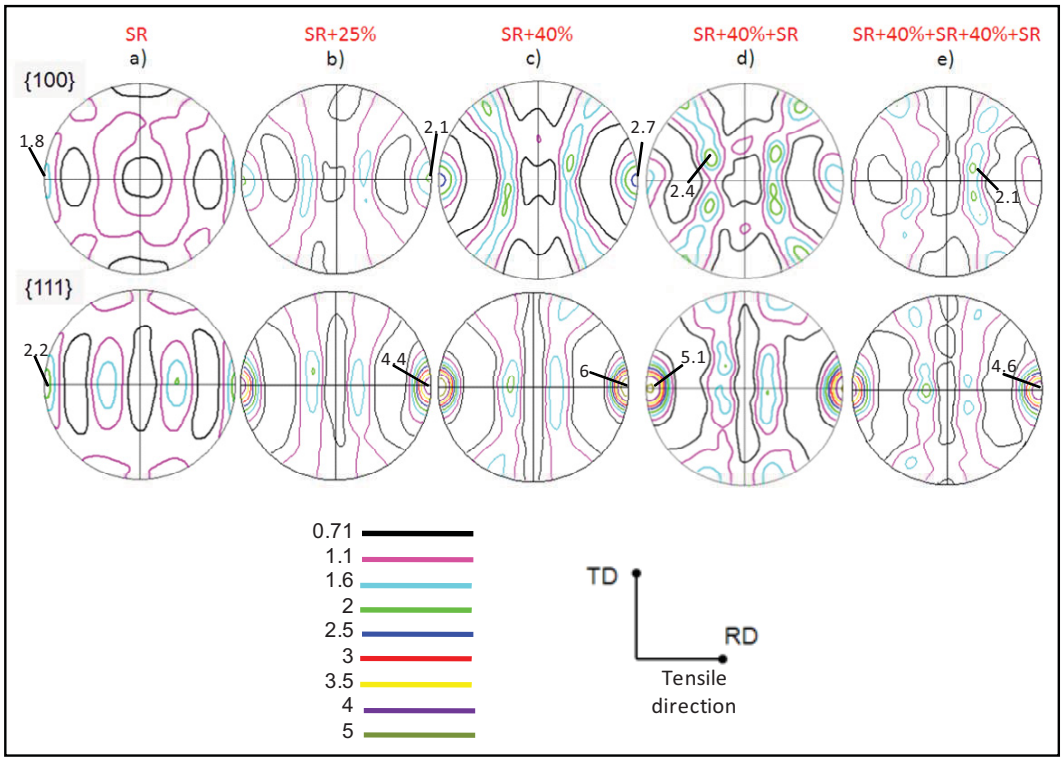

Figure 4.7 The {100} and {111} pole figures of austenite at various stages in the multistep forming process:
a) SR, b) SR+25%, c) SR+40%, d) SR+40%+SR and e) SR+40%+SR+40%+SR

Another method to represent the texture is the use of Inverse Pole Figures (IPF), as shown in Figure 4.8. The intensity in the IPF refers to the MUD associated with a particular crystallographic direction coinciding with a reference direction. The tensile direction (RD) was taken as the reference direction in Figure 4.8, as it is a direction of symmetry for the deformation process. Table 4.6 groups the maximum MUD obtained and the corresponding orientation after specific steps in the multi-step forming process. The effect of deformation in the austenite texture can be seen through Figure 4.8a to 8c. In Figure 4.8a, the starting state (SR) of the material presents a random texture, the MUD being rather very weak (maximum of 2.3). With this representation, the two fibers are clearly seen when increasing the amount of deformation (from 0% to 25%), reaching 3.9 and 2.1 for the component <111> and <001>, respectively (Figure 4.8b). After 40% strain, in Figure 4.8c, the <111> fiber component is

reinforced with a maximum of 5.1 against 2.4 for <001>. It is noteworthy that the <111> fiber texture is significantly stronger than the <101> fiber texture. Hence, a considerable portion of the microstructure becomes stabilized due to rotation towards the <111> fiber, whilst a relatively smaller fraction is represented by the <101> texture.

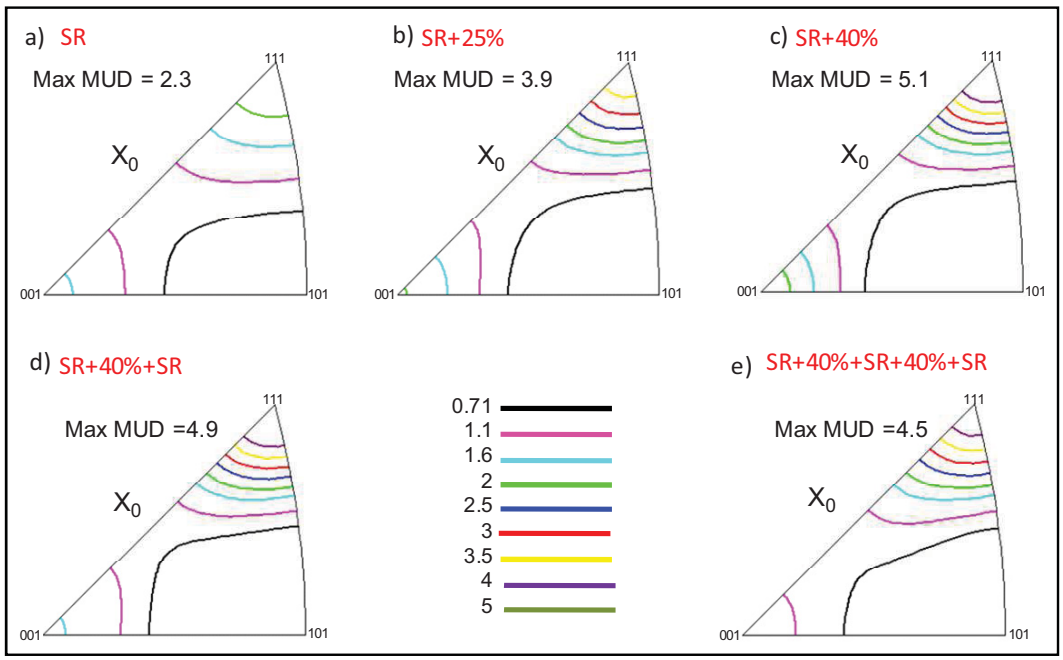

Figure 4.8 Rolling and tensile direction inverse pole figures of the austenite at various stages in the multistep forming process: a) SR, b) SR+25%, c) SR+40%, d) SR+40%+SR and e) SR+40%+SR+40%+SR

The effect of the SR heat treatment observed on the pole figures in Figure 4.7 is similar to the IPF results. The MUD decreases slightly for both fiber directions, displaying some randomization of the texture (Figure 4.8c versus Figure 4.8d). However, the material remains textured confirming that heat treatment resulted in partial recrystallization. The strongest texture component remains close to the <111> direction and extends from 5.1 to 4.9 whereas the texture component <001> decreased from 2.4 to 1.6.

Table 4.6 Maximum values of MUD and the corresponding orientation of SS321 after specific steps in the interrupted tensile tests

Steps of the process	IPF in RD (X_0) - AUSTENITE	
	Orientation	Maximum MUD
SR	<111>	2.3
SR+25%	<111>	3.9
SR+40%	<111>	5.1
SR+40%+SR	<111>	4.9
SR+40%+SR+40%+SR	<111>	4.5

Figure 4.9 is an illustration of the effect of deformation on the orientation maps. It represents the crystallographic orientation according to the tensile direction for the same area at respectively 0%, 25% and 40% deformation for the austenite phase; the reference color code used is shown in the IPF triangle for the tensile direction (initial RD). In this microstructure, the martensite phase (not indexed) is left blank (white). As the strain increased, the <101> texture component (grains demarcated by the green color) decreased and almost disappeared at 40% strain, whereas the texture component <111> (grains demarcated by the blue color) increased. At the same time, the texture component <001> (grains demarcated by the red color) increased, but not as much as the <111>.

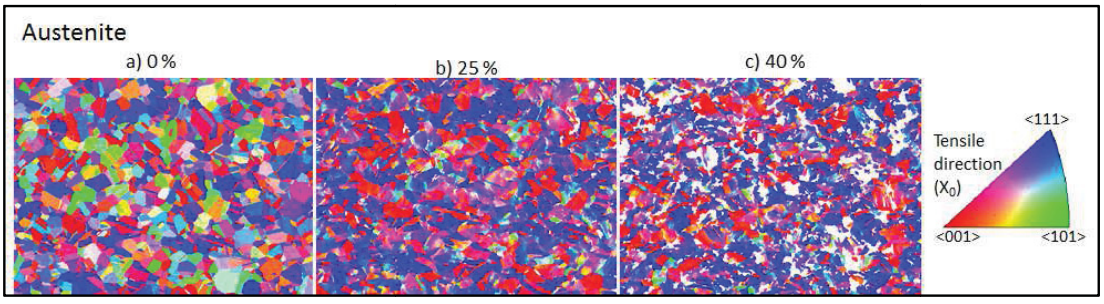

Figure 4.9 EBSD orientation maps of austenite (along the RD) in SS321 at different strain levels

4.4.3 Strain induced martensite

Figure 4.10 shows the α'-martensite content superimposed on the stress-strain curves. Specifically, the martensite volume fraction is presented as a function of the cumulative engineering strain. The error bars represent the minimum and maximum values measured for the martensite fraction at each strain level. The evolution in the average martensite content is very similar at each step of the multi-step forming process. The martensite amount increases with strain, but its rate of formation remains very low until a specific amount of deformation (around 20%) is accrued. When this level of strain is reached, the fraction of martensite starts to increase rapidly. The formability limit, in addition to the relative stability of the SS321 at room temperature, prevents the SIM content from reaching the saturation value, i.e. the maximum amount of martensite that can be strain-induced in the material depends on the chemical composition, temperature, strain rate, and/or austenite grain size. During the second deformation step, large variations in martensite content were recorded (larger error bars). At this point, the gauge length of the specimen had nearly doubled and the martensite content varied significantly from one location to another.

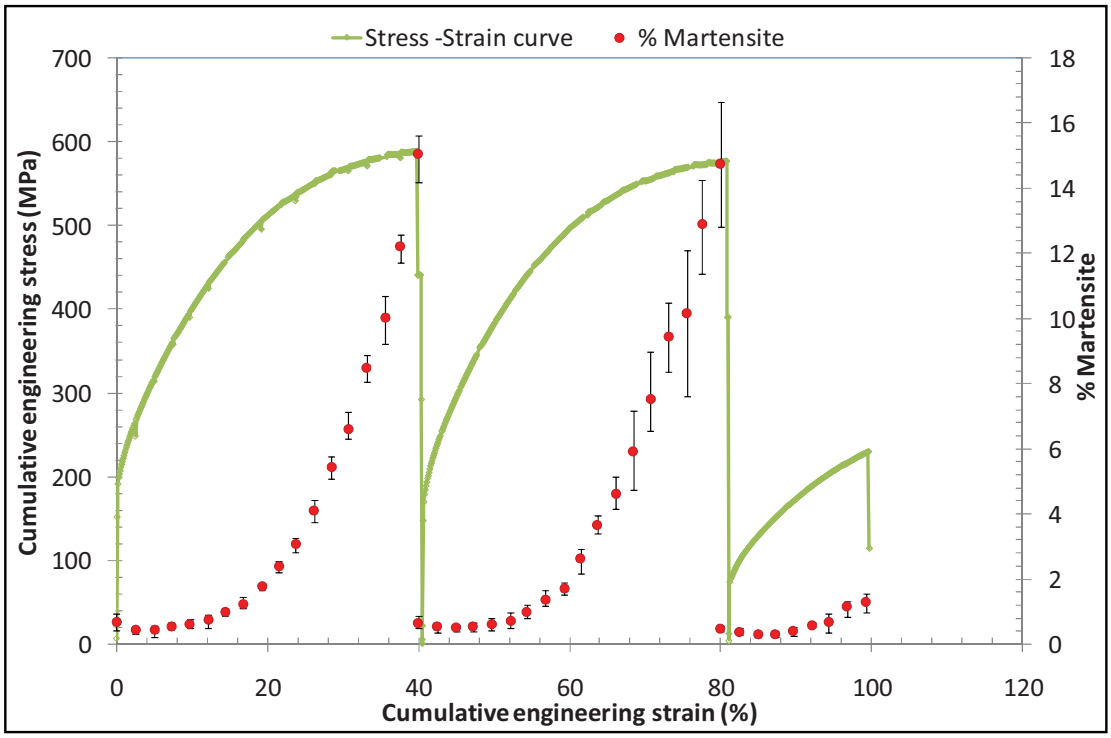

Figure 4.10 SIM evolution superimposed on the average cumulative engineering stress-strain curve for specimens subjected to interrupted tensile testing. The error bars represent the minimum and maximum values measured for the martensite content

In Figure 4.11, the typical evolution in the martensite content with strain distribution is presented for the case of one specimen subjected to multi-step deformation in which steps 2 and 3 were observed to superimpose on the step 1 data. For each step, the SIM formation curve had the general appearance of an initial sigmoidal-shape as it is expected for a SIM distribution but without a saturation phase (at the end) and could be separated into two parts, as a function of the slope change. For deformations up to 20% strain, the rate of martensite formation is rather linear, very low and with no difference observable amongst the 3 steps. At this point, when the total applied strain exceeds 20%, examining steps 1 and 2 only, the measured fraction of martensite rises sharply and continues to increase with a slope ten times greater than that below 20% strain. For a given strain value above 20%, the amount of martensite generated was observed to be consistently higher in the second forming step relative to the first. For instance, at a strain of ~35%, the amount of martensite in step 2 was

~20% higher when compared with that at step 1 and taking into account the standard deviation of the results.

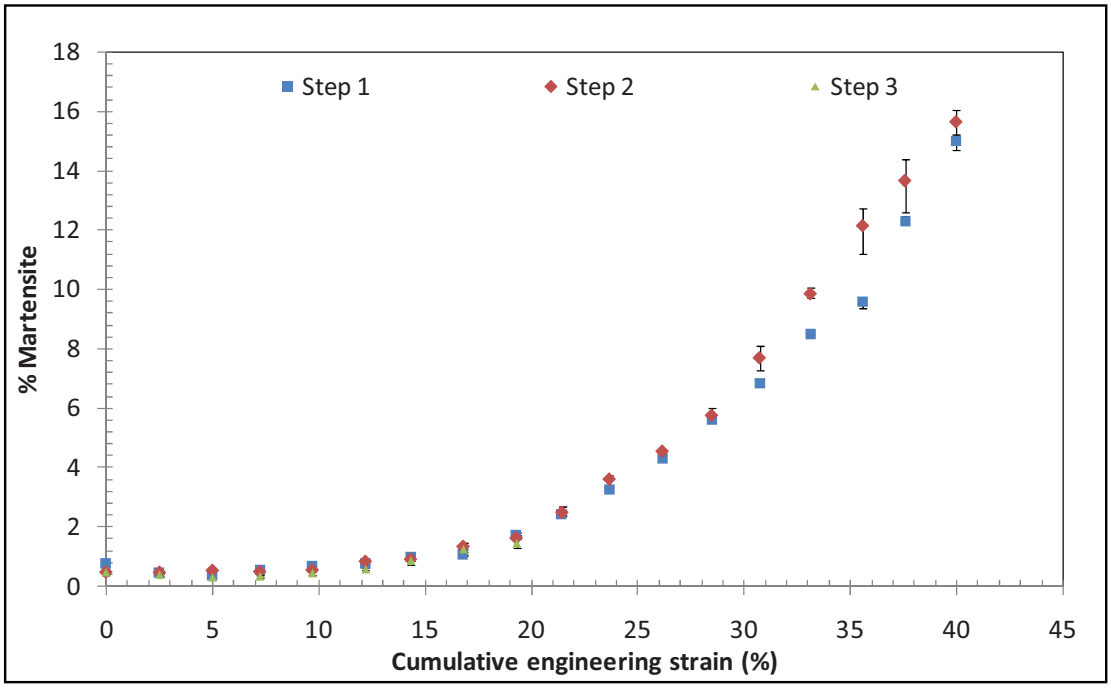

Figure 4.11 Typical evolution of the SIM content in one specimen deformed by interrupted tensile testing

Figure 4.12 presents the curves obtained after fitting the data with equations (1) and (2). The Olson-Cohen equation fits very well the experimental data. By contrast, the Tsuta-Grosse equation was unable to capture the trend of the SIM kinetics. In particular, the Tsuta-Grosse equation overestimates the martensite content at the start (early stage) of the deformation and fails to account for the abrupt increase in the rate of formation at around 20% strain. Hence, the Tsuta–Grosse equation, despite being generated for complex strain paths and low amounts of SIM, was not applicable in the present case. Thus, only the fitting parameters of the Olson-Cohen equation (α and β) were analyzed further to identify the best fit values for each stage of the multi-step process, as listed in Table 4.7. The α parameter is classically related to the rate of shear band formation as a function of the strain (Olson andCohen, 1975;

Ramirez et al., 1992). An increase in this parameter from 1.9 to 2.5 between steps 1 and 2 may be indicative of some interesting features related to shear band formation during multi-step forming. Specifically, the combination of deformation and heat treatment seems to facilitate shear band formation that then favors the intersection of shear bands for the nucleation of martensite. The SR heat treatment, despite decreasing the density of dislocations, allows nucleation sites for shear bands to reactivate earlier (at lower stress) in step 2, for instance. It is also possible that some orientations are more favorably oriented for early shear band activation. Research targeted to this understanding is currently ongoing to validate these postulations.

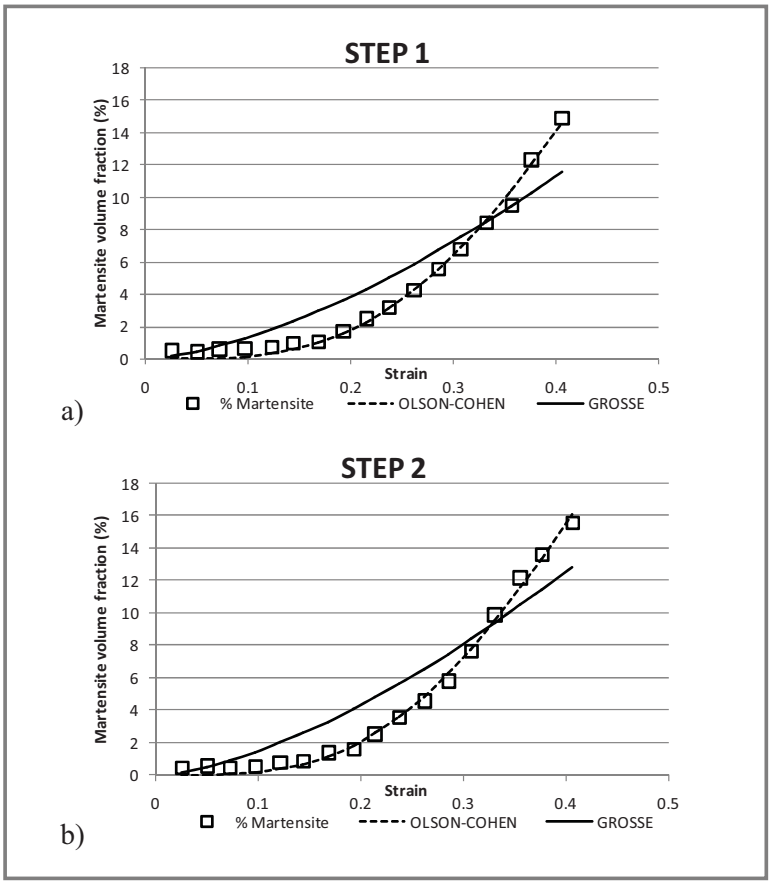

Figure 4.12 SIM formation as a function of the cumulative engineering strain in multistep forming:
a) Step 1and b) Step 2

In the Olson-Cohen model, the β parameter is proportional to the probability that a shear band intersection will become a martensite nucleation site. From step 1 to step 2, the β parameter is reduced from 4.7 to 2.3, decreasing the probability of α'-martensite nucleation from shear band formation. The earlier shear bands formed, as suggested by the increase in the α parameter, is therefore balanced by a reduction in the probability of these developing as martensite embryos.

Table 4.7 Olson-Cohen fitting parameters derived from the α'-martensite fraction measured in multistep forming

Olson - Cohen	α	β	R^2
Deformation step 1	1.89 ± 0.07	4.70 ± 0.64	0.997
Deformation step 2	2.50 ± 0.26	2.28 ± 0.76	0.992

4.4.3.1 Strain Induced Martensite texture

The spatial distribution of the SIM is illustrated in Figure 4.13 through orientation maps. In the present case, the austenite phase was left blank and thus appears as white regions in the microstructure. Up to 25% deformation, the volume fraction of SIM was too low (3%) to clearly identify a tendency on the color map, but at 40% deformation, the amount of martensite (~15%) generated was sufficient to describe a <101> texture component (green color). A second texture component was also observed, but to a lower extent, between <001> and <111>. Only very few grains were present with an orientation close to <111> according to the RD. In addition, the SIM was well-distributed throughout the microstructure, though some regions appeared almost fully transformed, whereas others had not transformed. These regions may likely be particular grains with specific orientations.

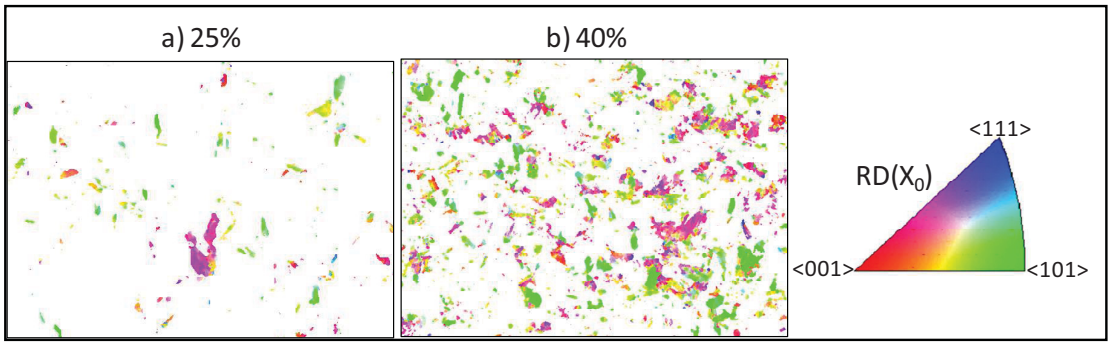

Figure 4.13 EBSD orientation maps of martensite (along RD) in SS321 at different strain levels

In studying the crystalline texture of the generated SIM, the martensite texture has been treated as BCC crystal structure because it was almost impossible to differentiate with 100% certainty the <100> and <001> poles using the EBSD method. Figure 4.14 shows the generated α'-martensite {100} and {110} pole figures for the deformed specimens during the first step (to be associated with Figure 4.7b and Figure 4.7c, respectively). The strain induced martensite formed in the 40% deformed sample is textured. Also the pole figures display clear evidence of symmetry expected in a rolled and tensile loaded material. This is not as clear in the 25% deformed specimen, most likely due to the low statistics of measurements as only 3% of this phase was found at this strain.

In the 40% strained specimen, the pole figures are symmetrical with the maximum texture residing on the <100> pole with an intensity around 2.6 (Figure 4.14). The maximum of the <110> pole figure did not correspond to the maximum found in the <111> austenite pole figure (Figure 4.7) as expected from the K-S type relationship, but rather to the second maximum of this <111> pole figure. At the maximum position of the <111> austenite pole figure, a rather low MUD value was found on the martensite <110> pole figure. This maximum position corresponded to the most stable orientations during tensile loading (the <111> fiber along the RD in Figure 4.7c). It is unlikely that these orientations undergo SIM transformation during the deformation process. On the other hand, other orientations not initially belonging to <111> fiber may generate SIM to compensate unfavorable slip activity.

The data in Figure 4.14 can be translated into an IPF, as presented in Figure 4.15. The main pole is around the <140> pole with a MUD around 2 for both specimens showing that the generated SIM remains stable during deformation.

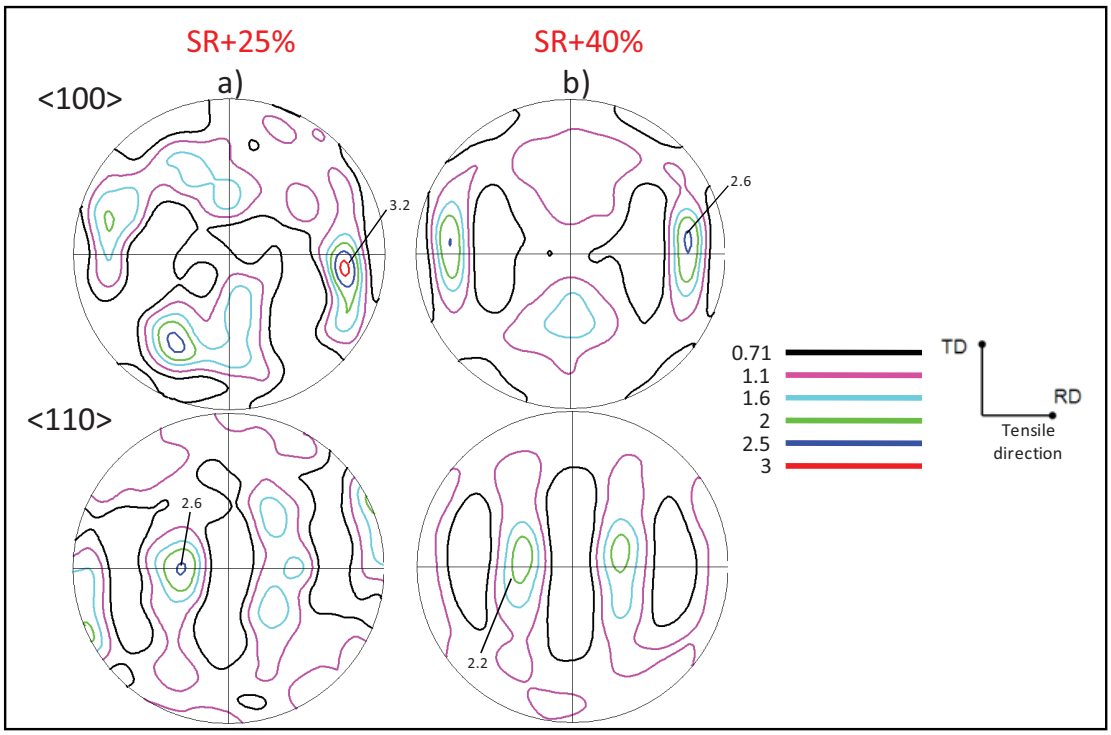

Figure 4.14 The {100} and {110} pole figures for martensite at different strain levels: a) SR+25% and b) SR+40%

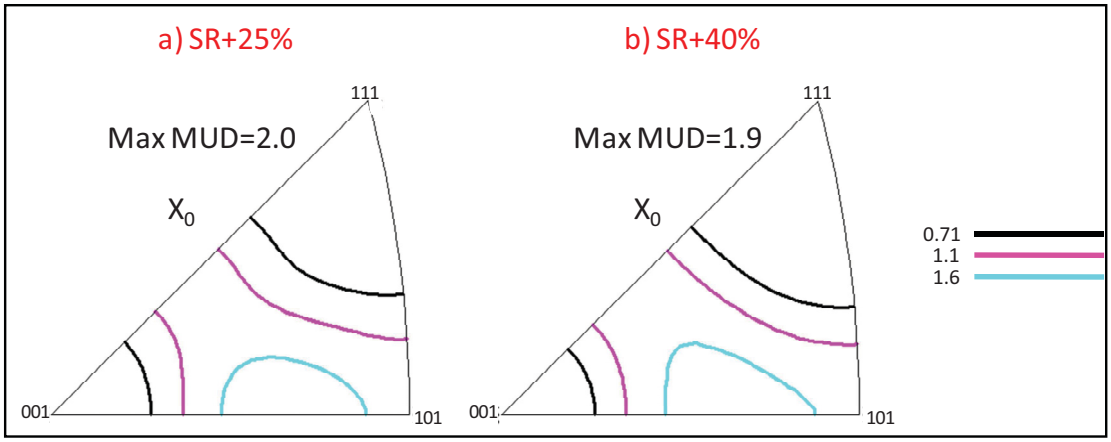

Figure 4.15 Rolling and tensile direction inverse pole figures of martensite at different strain levels: a) SR+25% and b) SR+40%

4.5 Discussion

The multi-step forming process applied to SS321 documented through the experimental results reveals several interesting phenomena. On the macroscopic scale, the intermediate SR heat treatment applied restores very well this material, which gives the possibility of deforming SS321 up to 100% strain in 3 steps, and probably higher deformation levels may be reached if additional heat treatment and deformation cycles were to be used. Also the observed decrease in the YS after the SR suggests that the SS321 is easier to deform with increasing number of deformation-heat treatment cycles. This behavior could be related to some texture evolution. It is important to note that the occurrence of SIM cannot be used to explain the YS variation, as it only influences levels of applied stress greater than the YS. It is most likely related to the small evolution in the texture. The texture development (grains reoriented with respect to the applied deformation) affects the mechanical properties, especially the YS, since it may facilitate or restrict the dislocation motion depending on the activated slip systems. In the present case it contributes to a reduction in the YS by several percentage points.

At the microscopic level, several processes were observed: SIM nucleation and growth during the deformation step, martensite transformation back into austenite during the SR heat treatment together with nucleation and growth in the deformed austenite phase (including the development of many orientations due to the formation of annealing twins). All these processes played a non-negligible role in the material response to the multi-step forming process as discussed below.

4.5.1 Strain induced martensite

A macroscopic indication that the microstructure behaves differently between the first and the second deformation steps can be found in the coefficient of the Olson-Cohen equation.

The first parameter, α, of this equation describes the rate of shear band formation as a function of the applied strain. The present data suggests that α increased significantly between steps 1 and 2, implying that the shear bands are generated more easily at the second step than in the first. This could be a consequence of the crystalline texture evolution of the starting material (in the SR condition before step 1) and the one at the onset of the second step of deformation. The stronger <111> fiber will favor the early generation of stable shear bands with multiple slips on almost equivalent primary and secondary maximum Schmidt factors (SF_2 / $SF_1 \approx 0.78$). By increasing significantly the number of shear bands during the second deformation step, one could expect to increase considerably the quantity of favorable SIM nucleation sites, as the number of shear bands intersections will increase. However, the evolution of the β parameter suggests that these intersections are not particularly suitable for martensite generation; specifically, the significant decrease in the value of β from step 1 to step 2 suggests that fewer shear band intersections generate α'-martensite embryos. Also, the results showed that the volume fraction of SIM is systematically higher in the second step for a given strain, indicating that the β parameter has less influence on SIM nucleation than the α parameter in the case of multi-step forming. However, this has to be experimentally confirmed with micro-scale analyses of deformed samples as in (Bridier et al., 2014) and (Stinville et al., 2015). In these studies, the grain-scaled deformation processes were tracked through a digital image correlation system combined with EBSD and in-situ tensile tests. The results permitted quantification of the strain fields within the grains as well as identifying the onset of deformation. In the case of SIM, this technique will have to be adapted, but it will allow identification of the specific grains and neighborhoods (orientation, texture, Schmidt factor) that are prone to the development of SIM.

4.5.2 Recrystallization

The objective of the intermediate heat treatment was to restore the material in order to allow continued deformation. Both, the level of deformation introduced in the material (40%) and the applied temperature and time during the heat treatment were sufficient to induce recrystallization. The enlargement of the grain size distribution after heat treatment suggested

that the recrystallization process was ongoing and some grain coarsening had started. The increased presence of annealing twins after heat treatment confirmed the occurrence of recrystallization even if a Strain Induced Boundary Migration phenomenon cannot be completely excluded. However, this amount was always lower than the one measured in a fully recrystallized structure, i.e. the starting material in the SR condition. Annealing twins are formed in FCC materials with low SFE, such as SS321, during recrystallization. They result from accidents associated with moving grain boundaries, and in particular with recrystallized grains formed from previously deformed material (Cahoon, Li andRichards, 2009; Song, Chun andHwang, 2007). As the volume fraction of twins measured after the complete deformation + heat treatment cycles did not reach the amount expected in a fully recrystallized material, partial recrystallization can be expected in the material. In fact, the percentage of non-recrystallized zones in the material after the first and second completed cycles was evaluated at 25% and 18%, respectively. The austenite texture analysis brought additional confirmation of the partial recrystallization, as, after a complete ‘SR + 40% + SR’ cycle, the material remained with a typical deformation texture. The generation of growth twins induces random textures unless some selective growth occurs during recrystallization (Gottstein, 1984; Saleh, Pereloma andGazder, 2011). A consequence of the latter would be that the texture of the larger grains would be different from that of the small ones, which was not the case in the present study. The observed randomization of the texture is therefore a consequence of the formation of growth twins and explains the lowering of the MUD intensity in Figure 8. Likewise, the weak deformation combined with the high solute content in the rolled stainless steels at medium deformation (60-80%) can explain the presence of weak recrystallization textures in this case. However, this decrease was not enough to erase the deformed material texture.

The SS321 microstructure developed during the multi-step forming process is quite complex at the end of a complete cycle (at 'SR + 40% + SR' for instance). Due to partial recrystallization, austenitic grains in a restored state (some dislocation structures were measured in some of the grains after SR, as seen in Figure 8d) as well as in a recrystallized state, coming from the previous martensite or deformed austenite grains, coexist in the

microstructure. Very low values of martensite were measured after one cycle, which implies that α'-martensite does not revert fully to create new austenitic grains. This suggests that the heat treatment temperature is too low to fully bring the material to its thermodynamic stability. Likewise, traces of remnant SIM also add complexity to the microstructure.

4.6 Summary and conclusions

The objective of this paper was to document the evolution of the mechanical and metallurgical properties of SS321 during a multi-step forming process that was simulated by a series of tensile tests with an intermediate softening heat treatment. A combination of 40% strain and stress relief heat treatments was applied to the tensile specimens so as to attain a cumulative strain of 100%. The mechanical properties were fully restored during the two inter-passes in the multi-step forming process by heat treating at 982°C for 1hour. This intermediate stress relief heat treatment was observed to decrease the yield strength and enhance the formability. The distribution in the fraction of twins indicated that the intermediate heat treatment led to partial recrystallization of the material at each step. Some grain growth was noted to occur as well. The texture analysis of the austenite showed that by increasing the level of deformation, the material develops a texture with the <111> component tending to align with the loading direction. A second component was found in the <110> fiber. Similar values of MUD were obtained in steps 1 and 2 of the multi-step forming process. The heat treatment applied randomized the deformed austenite texture thus confirming that recrystallization took place and was most likely incomplete.

A texture analysis of the deformed specimens was performed in order to study the impact of the deformation on the strain induced martensite texture evolution. The strain induced martensite was generated with a texture that slightly decreased with increasing deformation. The first orientation that formed was near the <140> pole.

The Olson-Cohen equation impeccably fitted the strain induced martensite data in the case of the multi-step forming process examined in this work. The evolution of the α and β

parameters related to this equation suggests that the multi-step forming process tends to promote shear band formation, but at the same time limits the probability that a shear band intersection becomes a martensite embryo. Such observations should be confirmed with more experimental data and micro-scale observations.

4.7 Acknowledgments

The authors would like to extend their gratitude to the Natural Sciences and Engineering Research Council of Canada (NSERC), the Consortium for Research and Innovation in Aerospace in Quebec under the CRIAQ 4.6 project and the Fonds Québécois de Recherche Nature et Technologies (FQRNT) for their financial support. The authors are also grateful to Mr. Daniel Turner at PWC for his assistance and support for the heat treatments.

4.8 References

Anderson, M. 2013. « Improving the formability of stainless steel 321 through multistep deformation for hydroforming applications ». *Transactions of the Canadian Society for Mechanical Engineering,* vol. 37, n° 1, p. 39.

Anderson, M., J. Gholipour, P. Bocher, F. Bridier, J. Savoie and P. Wanjara. 2010. « Formability extension of aerospace alloys for tube hydroforming applications ». *International Journal of Material Forming,* vol. 3, n° SUPPL 1, p. 303-306.

Angel, T. 1954a. « Formation of martensite in austenitic stainless steels ». *Iron and Steel Institute -- Journal,* vol. 177, n° Part 1, p. 165-174.

Barbier, D., N. Gey, S. Allain, N. Bozzolo and M. Humbert. 2009. « Analysis of the tensile behavior of a TWIP steel based on the texture and microstructure evolutions ». *Materials Science and Engineering: A,* vol. 500, n° 1–2, p. 196-206.

Beese, A. M., and D. Mohr. 2009. « Experimental Quantification of Phase Transformation in Austenitic Stainless Steel ». In *SEM 2009 Annual Conference & Exposition on Experimental & Applied Mechanics*. (Albuquerque New Mexico USA, June 1-4, 2009). Society for Experimental Mechanics.

Bridier, F., J-C. Stinville, N. Vanderesse, P. Villechaise and P. Bocher. 2014. « Microscopic strain and crystal rotation measurement within metallurgical grains ». *Key Engineering Materials,* vol. 592-593, p. 493-496.

Cahoon, J. R., Qiangyong Li and N. L. Richards. 2009. « Microstructural and processing factors influencing the formation of annealing twins ». *Materials Science and Engineering: A,* vol. 526, n° 1–2, p. 56-61.

Chandler, Harry. 1995. *Heat treater's guide : practices and procedures for irons and steels*, 2nd. Materials Park, OH: ASM International, vii, 903 p.

Chunchun, Xu, Hu Gang and Wing-Yan Ng. 2004. « Relationship between the martensite phase transition and pitting susceptibility of AISI-321 stainless steel in acidic solutions of NaCl ». *Materials Science,* vol. 40, n° 2, p. 252-259.

Dash, S., and N. Brown. 1963. « An investigation of the origin and growth of annealing twins ». *Acta Metallurgica,* vol. 11, n° 9, p. 1067-1075.

Durand-Charre, Madeleine. 1997. *The microstructure of superalloys*. Boca raton, Flor.: CRC Press, xiv, 124 p.

Fischer. 2006. *Operator's manual for feritscope MP30E-S.*

Fullman, R. L., and J. C. Fisher. 1951. « Formation of Annealing Twins During Grain Growth ». *Journal of Applied Physics,* vol. 22, n° 11, p. 1350-1355.

Gey, Nathalie, B. Petit and M. Humbert. 2005. « Electron backscattered diffraction study of / martensitic variants induced by plastic deformation in 304 stainless steel ». *Metallurgical and Materials Transactions A: Physical Metallurgy and Materials Science,* vol. 36, p. 3291-3299.

Ghosh, S., P. Mallick and P. Chattopadhyay. 2011. « Effect of reversion of strain induced martensite on microstructure and mechanical properties in an austenitic stainless steel ». *Journal of Materials Science,* vol. 46, n° 10, p. 3480-3487.

Gleiter, H. 1969. « The formation of annealing twins ». *Acta Metallurgica,* vol. 17, n° 12, p. 1421-1428.

Gottstein, G. 1984. « Annealing texture development by multiple twinning in f.c.c. crystals ». *Acta Metallurgica,* vol. 32, n° 7, p. 1117-1138.

Grosse, M., D. Kalkhof, M. Niffenegger and L. Keller. 2006. « Influencing parameters on martensite transformation during low cycle fatigue for steel AISI 321 ». *Materials Science and Engineering: A,* vol. 437, n° 1, p. 109-113.

Hecker, S., M. Stout, K. Staudhammer and J. Smith. 1982. « Effects of Strain State and Strain Rate on Deformation-Induced Transformation in 304 Stainless Steel: Part I.

Magnetic Measurements and Mechanical Behavior ». *Metallurgical and Materials Transactions A,* vol. 13, n° 4, p. 619-626.

Jiménez, J. A., and G. Frommeyer. 2010. « Analysis of the microstructure evolution during tensile testing at room temperature of high-manganese austenitic steel ». *Materials Characterization,* vol. 61, n° 2, p. 221-226.

Kumar, B. Ravi, A. K. Singh, B. Mahato, P. K. De, N. R. Bandyopadhyay and D. K. Bhattacharya. 2006. « Deformation-induced transformation textures in metastable austenitic stainless steel ». *Materials Science and Engineering: A,* vol. 429, n° 1–2, p. 205-211.

Kurc-Lisiecka, A., W. Ozgowicz and W. Ratuszek. 2012. « Development of deformation texture of austenitic Cr-Ni steel ». *Machines, Technologies, Materials virtual journal*, n° 9, p. 47-50.

Kurdjumow, G., and G. Sachs. 1930. « Über den Mechanismus der Stahlhärtung ». *Zeitschrift für Physik,* vol. 64, n° 5-6, p. 325-343.

Leban, Mirjam Bajt, and Robert Tisu. 2013. « The effect of TiN inclusions and deformation-induced martensite on the corrosion properties of AISI 321 stainless steel ». *Engineering Failure Analysis,* vol. 33, n° 0, p. 430-438.

Lula, R. A., J. Gordon Parr and Albert Hanson. 1989. *Stainless steel*, rev. Metals Park, Ohio: American Society for Metals, x, 173 p.

Mangonon Jr, P. L., and G. Thomas. 1970. « Structure and properties of thermal-mechanically treated 304 stainless steel ». vol. 1, p. 1587-1594.

Meetham, G. W. 1981. *The development of gas turbine materials*. New York, N.Y.: Halsted Press, J. Wiley and Sons., xi, 306 p.

Meyers, Marc A., and Lawrence E. Murr. 1978. « A model for the formation of annealing twins in F.C.C. metals and alloys ». *Acta Metallurgica,* vol. 26, n° 6, p. 951-962.

Olson, G. B., and Morris Cohen. 1975. « Kinetics of strain-induced martensitic nucleation ». *Metallurgical Transactions A,* vol. 6, n° 4, p. 791-795.

Olson, G., and Morris Cohen. 1976. « A general mechanism of martensitic nucleation: Part I. General concepts and the FCC → HCP transformation ». *Metallurgical and Materials Transactions A,* vol. 7, n° 12, p. 1897-1904.

Peterson, S., M. Mataya and D. Matlock. 1997. « The formability of austenitic stainless steels ». *JOM Journal of the Minerals, Metals and Materials Society,* vol. 49, n° 9, p. 54-58.

Ramirez, Jorge Armando Cortes, Toshio Tsuta, Yoshito Mitani and Kozo Osakada. 1992. « Flow Stress and Phase Transformation Analyses in the Austenitic Stainless Steel under Cold Working : Part 1, Phase Transformation Characteristics and Constitutive Formulation by Energetic Criterion ». *JSME international journal. Ser. 1, Solid mechanics, strength of materials,* vol. 35, n° 2, p. 201-209.

Ravi Kumar, B., S. K. Das, B. Mahato and R. N. Ghosh. 2010. « Role of strain-induced martensite on microstructural evolution during annealing of metastable austenitic stainless steel ». *Journal of Materials Science,* vol. 45, p. 911-918.

Ray, R. K., J. J. Jonas, Butr, oacute, Guill n, eacute, M. P. n and J. Savoie. 1994. « Transformation Textures in Steels ». *ISIJ International,* vol. 34, n° 12, p. 927-942.

Rosen, A., R. Jago and T. Kjer. 1972. « Tensile properties of metastable stainless steels ». *Journal of Materials Science,* vol. 7, n° 8, p. 870-876.

Saleh, Ahmed A., Elena V. Pereloma and Azdiar A. Gazder. 2011. « Texture evolution of cold rolled and annealed Fe–24Mn–3Al–2Si–1Ni–0.06C TWIP steel ». *Materials Science and Engineering: A,* vol. 528, n° 13–14, p. 4537-4549.

Smaga, M., F. Walther and D. Eifler. 2008. « Deformation-induced martensitic transformation in metastable austenitic steels ». *Materials Science and Engineering A,* vol. 483-484, n° 1-2 C, p. 394-397.

Solomon, N., and I. Solomon. 2010. « Deformation induced martensite in AISI 316 stainless steel ». *Revista de metalurgia,* vol. 46, n° 2, p. 121-128.

Song, K. H., Y. B. Chun and S. K. Hwang. 2007. « Direct observation of annealing twin formation in a Pb-base alloy ». *Materials Science and Engineering: A,* vol. 454–455, p. 629-636.

Stinville, J. C., N. Vanderesse, F. Bridier, P. Bocher and T. M. Pollock. 2015. « High resolution mapping of strain localization near twin boundaries in a nickel-based superalloy ». *Acta Materialia,* vol. 98, p. 29-42.

Talonen, J., P. Aspegren and H. Hänninen. 2004. « Comparison of different methods for measuring strain induced α-martensite content in austenitic steels ». *Materials Science & Technology,* vol. 20, n° 12, p. 1506-1512.

Talonen, Juho, Pertti Nenonen, Gersom Pape and Hannu Hanninen. 2005. « Effect of strain rate on the strain-induced , &rarr -martensite transformation and mechanical properties of austenitic stainless steels ». *Metallurgical and Materials Transactions A: Physical Metallurgy and Materials Science,* vol. 36 A, n° Compendex, p. 421-432.

Tsuta, Toshio, and Jorge Cortes R. A. 1993. « Flow Stress and Phase Transformation Analyses in Austenitic Stainless Steel Under Cold Working : Part 2, Incremental Theory Under Multiaxial Stress State by the Finite-Element Method ». *JSME international journal. Ser. A, Mechanics and material engineering,* vol. 36, n° 1, p. 63-72.

Venables, J. A. 1962. « The martensite transformation in stainless steel ». *Philosophical Magazine,* vol. 7, n° 73, p. 35-44.

CHAPTER 5

PAPER 3: INCREASING THE HYDROFORMABILITY OF STAINLESS STEEL 321 BY MULTISTEP PROCESSING

M. Anderson[1,2], P. Bocher[1], J. Gholipour[2], M. Jahazi[1], J. Savoie[3], P. Wanjara[2]

[1]Ecole de Technologie Superieure, Mechanical Engineering Department, Montreal, Canada
[2]National Research Council Canada, Aerospace Manufacturing, Montreal, Canada
[3]Pratt & Whitney Canada, Special Process Development Group, Longueuil, QC, Canada

Conference paper published in Special Issue of *Steel Research International*, p. 1243-1246, Krakow, Poland (Proceedings of the 14th International Conference on Metal Forming "Metal Forming 2012", September 16-19, 2012).

5.1 Abstract

The application of the tube hydroforming process for the manufacture of aerospace components is relatively new and challenging due to the limited formability of high strength alloys used for aerospace applications. A multistep forming process, including intermediate heat treatment steps, has been proposed as a viable solution for increasing the hydroformability of these alloys. Interrupted free expansion tests were used in this study to emulate the multistep forming. Initially, free expansion tests were performed up to the burst point to determine the maximum pressure. An automated 3D deformation measurement system, ARAMIS®, was used to measure the strain distribution along the tube length as well as to measure the bulge height (expansion) as a function of time. Based on the strain distribution results obtained from ARAMIS®, a pause pressure corresponding to about 80% of the burst or maximum pressure was selected as the interruption point of the free expansion test in order to apply a softening heat treatment to restore the formability of the material. After this free expansion and softening cycle, the tube was then hydroformed up to the burst point. The results indicated that the inclusion of an intermediate heat treatment before the second forming step increased the expansion from 9.5 mm to 12 mm, a 26% increase.

Interestingly, in addition to the higher expansion, the pressure required to reach a specific level of expansion was reduced by half due to the softening effect of the intermediate heat treatment and thinning of the tubes from the first forming step.

5.2 Introduction

Tube hydroforming (THF) is an innovative forming process that uses a pressurized fluid (liquid or gas) to plastically deform a given straight or pre-bent tube into a desired shape. This technique presents many advantages compared to the traditional stamping and welding processes. It allows a lower weight/rigidity ratio as well as a reduction in the number of welds in an assembly. Moreover, hydroforming provides higher strength and quality in a part with a complex geometry. This process is also known for its reduced tooling cost and fewer number of secondary operations (Zhang, 1999). With all these advantages, hydroforming has become a widely used forming process in many industries such as automotive, marine, sanitary and electronic (Lang et al., 2004). In the case of the aerospace industry, the application of the THF process is limited due to the complexity of the aerospace components, the tight tolerance allowable, as well as the relative limited formability of the aerospace alloys. Tackling these exigent challenges, particularly the limited formability, corresponds to the main purpose of the present study. In order to increase the hydroformability of aerospace alloys, the application of an intermediate heat treatment after forming has been considered in this work.

The application of a multistep forming process on stainless steel 321 (SS321) sheet material has already been demonstrated (Anderson et al., 2010). Particularly, interrupted tensile testing of SS321 sheets, which was used to emulate multistep forming, increased noticeably the formability of the material, rendering about 120% deformation after four forming and heat treatment steps. The same grade was used in the present study to validate the feasibility of such a process under a biaxial strain condition.

Specifically, in the present study, the multistep forming process has been conducted by interrupted free expansion (FX) testing. Under these conditions, contrary to the uniaxial tensile test, the deformation of the tube is biaxial. Many authors (Chen, Soldaat andMoses, 2004; Gholipour, Worswick andOliviera, 2004; Koç, Aue-u-lan andAltan, 2001; Kuwabara et al., 2003; Levy, Van Tyne andStringfield, 2004) consider that the flow curve representing the biaxial behavior of the tube during FX is more accurate than the use and extrapolation of a stress-strain curve obtained from tensile testing. However, the later is a method commonly used in simulating forming processes for simplicity reasons. In fact, FX tests allow the determination of the mechanical properties in a biaxial state of strain, but involve greater effort and cost for experimentation. The FX tests have been performed on SS321 tubes with a 50.8 mm outside diameter and 0.9 mm thickness in order to be as close as possible to a realistic hydroforming process for an aerospace component.

5.3 Experimental procedure

Figure 5.1 shows the schematic of the FX test. The geometrical parameters illustrated in the figure are r_o the initial tube radius, w the bulge width and h the bulge height.

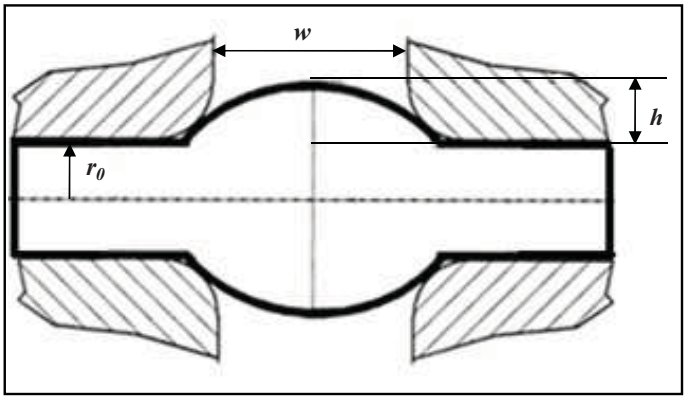

Figure 5.1 Schematic view of a FX test

The FX test is conducted by placing the original tube into an open die in a hydroforming press. Then the tube is clamped by the upper and lower dies. Two end plungers (not shown

here) seal the tube ends during the FX process. Then the tube is pressurized internally by a fluid, generally water, which deforms (bulges) the tube in the unclamped region and ultimately leads to bursting of the tube at the burst pressure. In this study, the FX tests were performed in the "no end feeding" condition; that is, no material from the clamped area was pushed into the deformation zone because axial displacement was prohibited during testing. To maintain high consistency and accuracy in the results, end feeding had to be restricted, as it increases the formability (bulge height) during hydroforming.

As FX testing is controlled by the internal pressure, it was necessary to determine the maximum pressure by initially conducting the FX tests up to the burst point. Based on these results, a pause pressure (Ppause) was defined that ensured homogeneous deformation in the bulged region of the tube. In the present investigation, the pause pressure was determined to be ~18 MPa, about 80% of the maximum pressure (Pmax). At this level of pressure, even though the tube expansion was significant, it remained uniform around the tube. The tube was then heat treated to fully restore the material properties. FX testing of the tube was then conducted to the burst point.

5.3.1 Material

SS321 is a chromium-nickel austenitic grade stabilized by titanium against intergranular chromium carbide precipitation. It possesses a relatively good formability and high corrosion resistance. It was chosen as a case study because of its wide applicability in the aerospace industry and relative inexpensiveness as compared to superalloy grades with which it shares some characteristics (FCC structure for example). It is noteworthy that SS321 can only be strengthen by cold working as no precipitation hardening or phase changes occur during heat treatment or quenching. Additionally, as the tubes were seamless, thermal cycling from welding does not factor into the results. The nominal tube diameter (2r0 in Figure 5.1) and thickness were 50.8 mm and 0.9 mm, respectively. The average tube thickness and diameter were recorded prior to testing to adjust the bulge height accordingly. The tubes were tested in their As-received condition.

5.3.2 Strain measurement

In order to evaluate the expansion of the tube during the FX test, a non-contact optical 3D deformation measurement system (Aramis®) was used to record images at a rate of 6 frames per second. This system comprises a sensor with two CCD cameras connected to a trigger box and a high performance PC system. Figure 5.2 shows the setup of the Aramis® system for the FX tests. The two stereoscopic cameras placed in front of the hydroforming press allowed capturing the in-plane strains during testing. After processing the Aramis data, it was possible to extract the strain distribution along the tube during the test as well as the bulge height as a function of the time. Additional details concerning the setup of the Aramis® system can be found in (Anderson et al., 2010).

The internal pressure in the tubes during the FX test was measured from the hydroforming press control system. The hydroforming equipment comprised of a 1000-Ton press with 413 MPa pressure intensifiers. A programmable pressure load and position control ensured repeatability of the tests. The associate control system recorded the different process parameters during the tests.

5.3.3 Intermediate heat treatment

Considering that SS321 can only be hardened by cold working, the heat treatment conducted in this study was a stress relief (SR). The SR performed on the interrupted free expanded tubes consisted of holding the tube for one hour at 982°C followed by rapid cooling at a rate $\geq$ 19°C/min. This heat treatment was conducted with the intent to fully anneal (static recovery and/or recrystallization) the SS321, which resulted in a drastic reduction in the yield stress and a significant increase in the ductility. Moreover, full annealing (at temperatures in the range of 928°C to 1093°C) is known to prevent chromium carbide formation, which may cause sensitization in SS321 (Chandler, 1995).

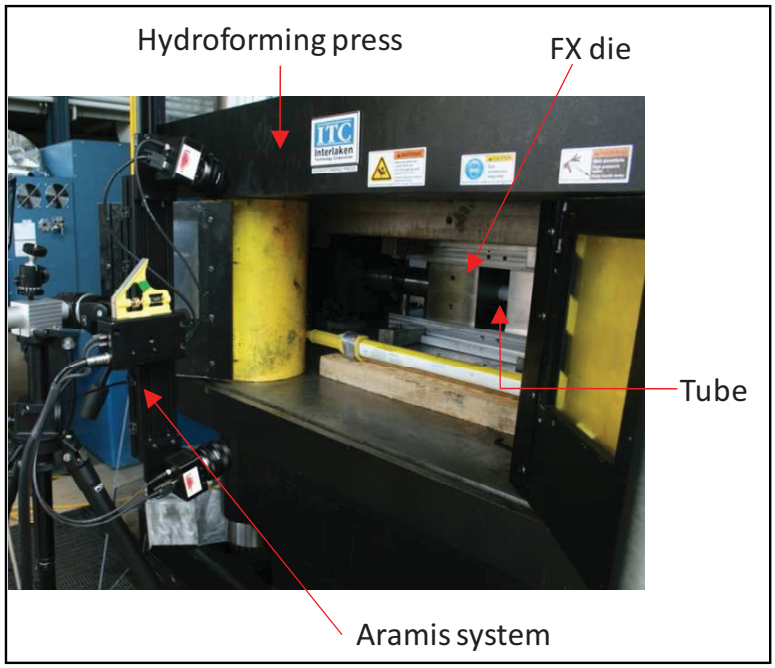

Figure 5.2 Set up for the FX testing

5.4 Results and discussion

5.4.1 Free expansion tests up to the burst (Single FX)

As mentioned before, to find the appropriate pause pressure, FX tests were conducted to the burst point. The bulge height or expansion, i.e. the difference between the maximum radius in the bulged area and the initial radius (h in Figure 5.1), was monitored during the test. Figure 5.3 shows two curves representing the expansion versus pressure obtained from the FX tests for two tubes up to the burst pressure. From Figure 5.3, it can be seen that the dependence of the bulge height on the internal pressure is highly reproducible. In both cases, the expansion reached to almost 10 mm with a maximum pressure around 20 MPa.

The strain distribution along the tube length at several stages of the FX test is plotted in Figure 5.4 to correlate the deformation to the pressure. From this figure, the pressure that retains homogeneous deformation in the bulged area can be identified. This pressure was

used as the pause pressure in this work. As can be seen from Figure 5.4, the major strain remains nearly constant in the section of the bulge width (w in Figure 5.1) between 30 mm and 70 mm, which was considered as the effective free expansion area in this work, beyond which the deformation was not uniform due to the tube/die contact regions at the edges. As the pressure was increased the effective free expansion area decreased rapidly to a point. To this end, at the maximum pressure (21.6 MPa) the maximum major strain was about 41% (Table 5.1) at the mid-section of the bulge width (~50 mm). Based on these results the value selected for the pause pressure was 17.7 MPa, about 4 MPa below the maximum pressure. At this pause pressure value, the difference in the maximum strain between the centre of the bulge width and at the edges is about 8% and is less than 1% within the effective free expansion area (30 mm ≤ bulge width ≤ 70mm).

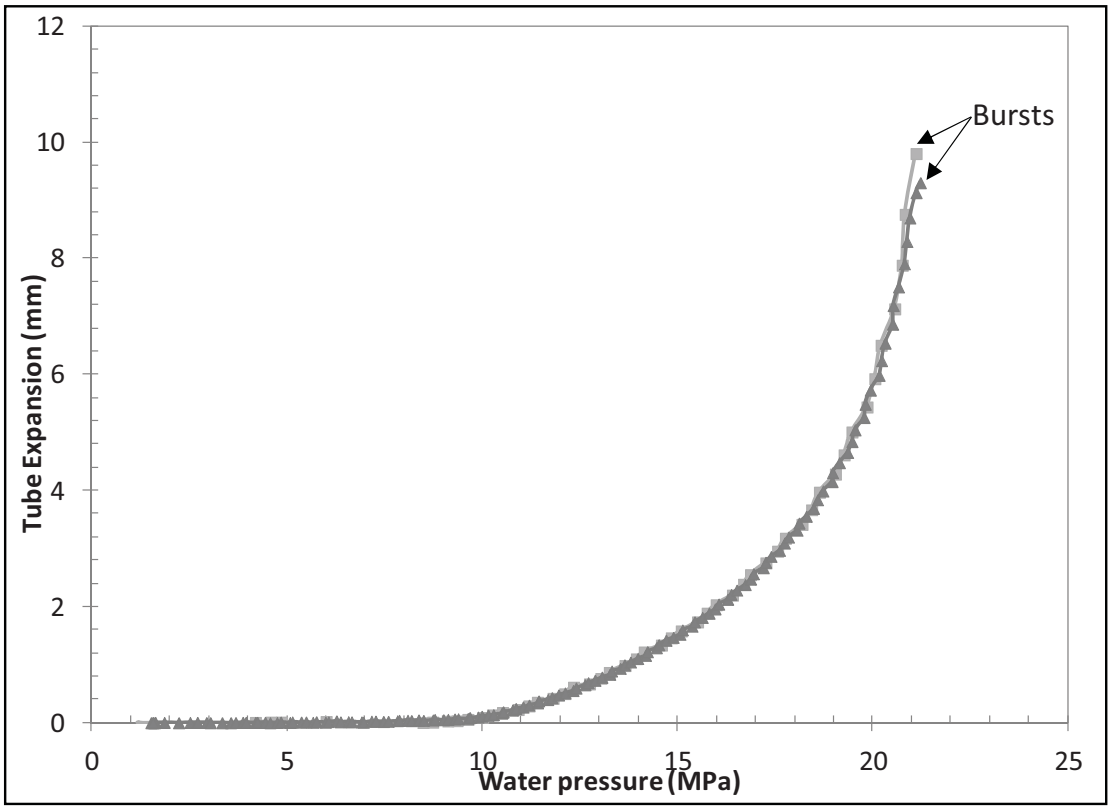

Figure 5.3 Bulge height versus internal pressure curve of two single FX tests to the burst point

Table 5.1 Pressure and strain reached during a single FX test (no intermediate heat treatment)

FX test up to burst	P_{Max} (MPa)	Maximum Strain (%)
	21.6	41

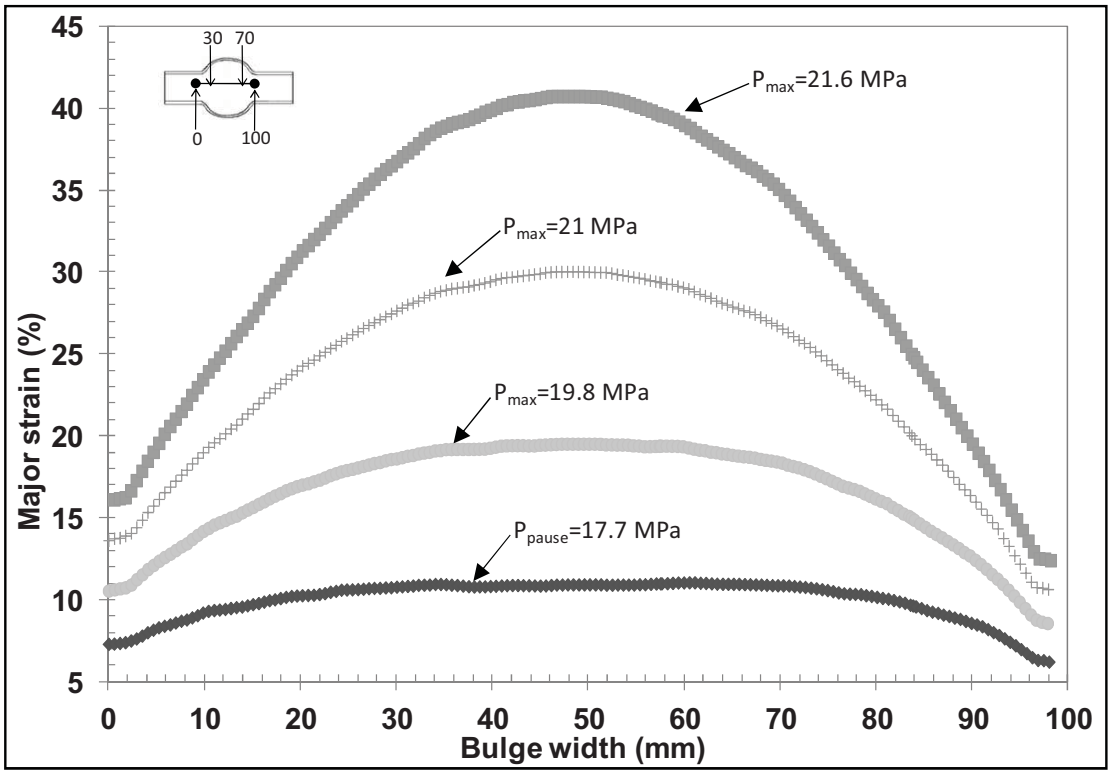

Figure 5.4 Strain distribution at various pressures during a single FX test conducted up to the burst point

5.4.2 Interrupted free expansion tests

The expansion results for an interrupted FX test are displayed in Figure 5.5. The lower curve represents the bulge height as a function of the pressure for the first forming step (Step 1) that was arrested at the pause pressure. The bulge height at the pause pressure reached about 3 mm before the SR heat treatment was applied. The upper curve shows the expansion during the second forming step (Step 2) which was conducted up to the burst point. In Step 2, the

maximum bulge height was determined to be about 9 mm, roughly equivalent to that observed for the single FX tests (Figure 5.3). This confirms the effectiveness of the intermediate heat treatment to almost fully restore the formability of the alloy. It is noteworthy that the maximum expansion in the Step 2 (~ 9mm) supplements the expansion obtained in Step 1, since the initial radius applied for the calculation of the bulge height was the final geometry after Step 1. Thus, when cumulating the bulge heights from Step 1 and Step 2, the final expansion of the tube is about 12 mm, which represents a gain of 26%. In addition, by comparing the curves before and after the SR heat treatment in Figure 5.5, it can be observed that at the same pressure, 15 MPa for example, the bulge height is doubled in Step 2 relative to Step 1. Also, the difference between the Ppause after Step 1 and the burst pressure for the interrupted FX test was relatively small (3.5 MPa). This can be explained by the fact that after Step 1, the tube is thinner than but as soft as the original tube, so less pressure is required to reach the same deformation in the tube. This behavior has been previously noted to occur during forming of aluminum and magnesium alloys (Groche et al., 2002; Kleiner, Geiger andKlaus, 2003).

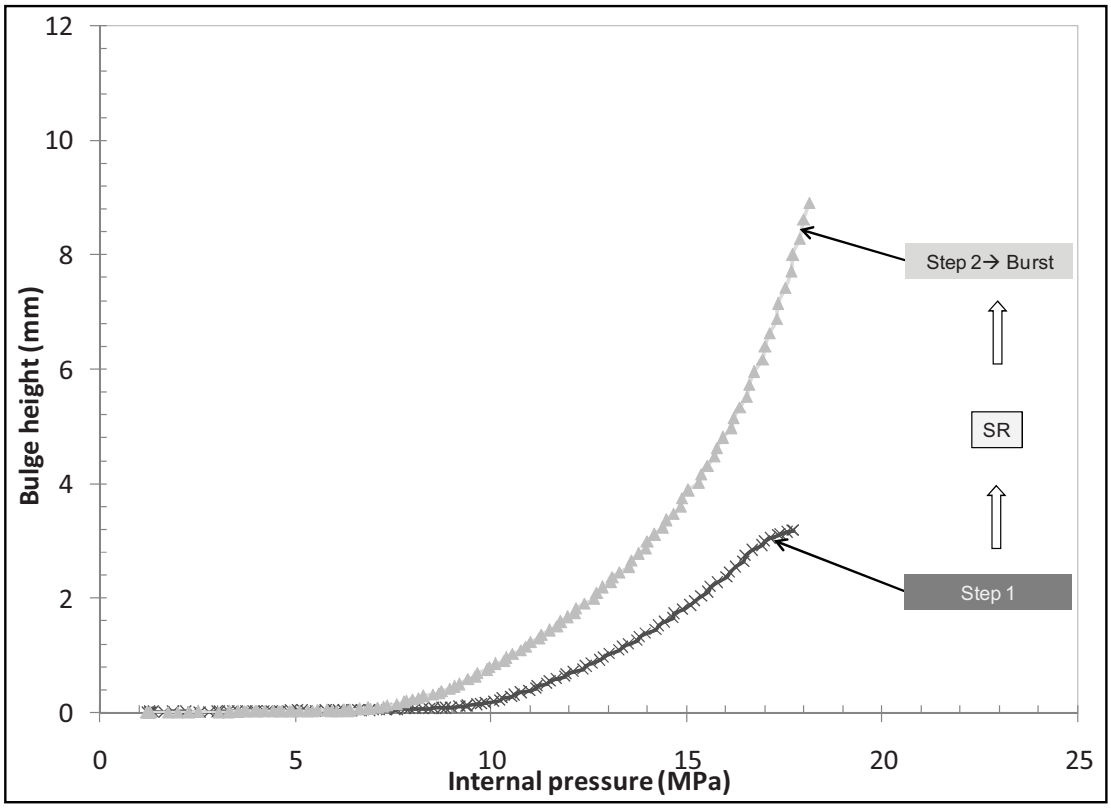

Figure 5.5 Bulge height versus internal pressure curve of interrupted FX tests

The strain distribution along the tube length in Step 1 and Step 2 of the interrupted FX test is displayed in Figure 5.6. The lower curve represents the strain distribution along the tube length for Step 1 of the interrupted FX test at the pause pressure. The upper curve corresponds to the strain distribution along the tube length at the burst point for a tube that was subjected to an interrupted FX test. At a pause pressure of 17.9 MPa (Step 1), the maximum strain was determined to be 13.7%. After an interrupted FX test (Step 2), the maximum strain at the burst pressure of 18.1 MPa was 36.4%. Table 5.2 shows the burst pressure and the maximum strain in Step 1 and Step 2 of the interrupted FX test. The maximum strain value of 36.1% that was attained in Step 2 is lower than that obtained for the single FX test (41%), as given in Figure 5.4 and Table 5.1. But, when the deformations from both steps are combined, the maximum cumulative deformation is greater than that from the single FX test.

Table 5.2 Pressures and strains reached during the interrupted FX test

Interrupted FX test	Step 1		Step 2	
	P_{Pause} (MPa)	Reached strain (%)	P_{Burst} (MPa)	Maximum strain (%)
	17.9	13.7	18.1	36.4

This increased formability between the single FX test and the interrupted FX test can be observed in the hydroformed tubes, as illustrated in Figure 5.7. Specifically, the maximum diameter of the bulged tube after bursting is considerably greater in the case of the interrupted FX test (~74.9 mm after Step 2) than at the end of a single FX test (~70.4 mm).

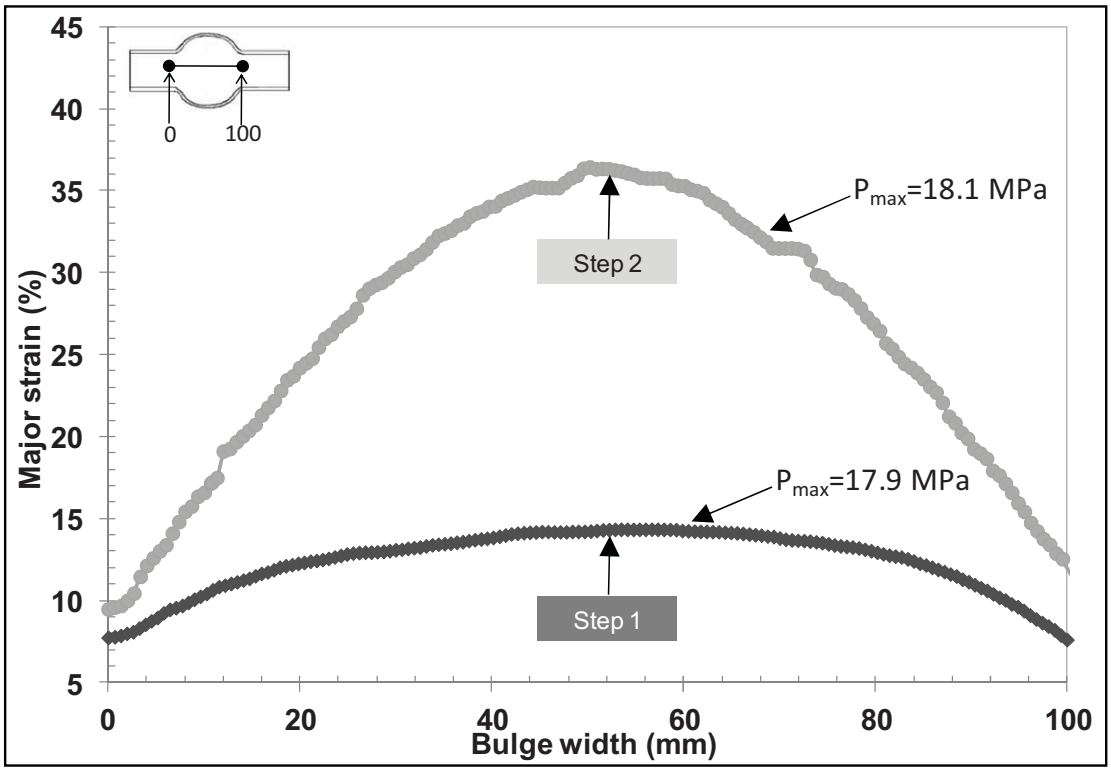

Figure 5.6 Strain distribution along a 0.9 mm thick tube during an interrupted FX test

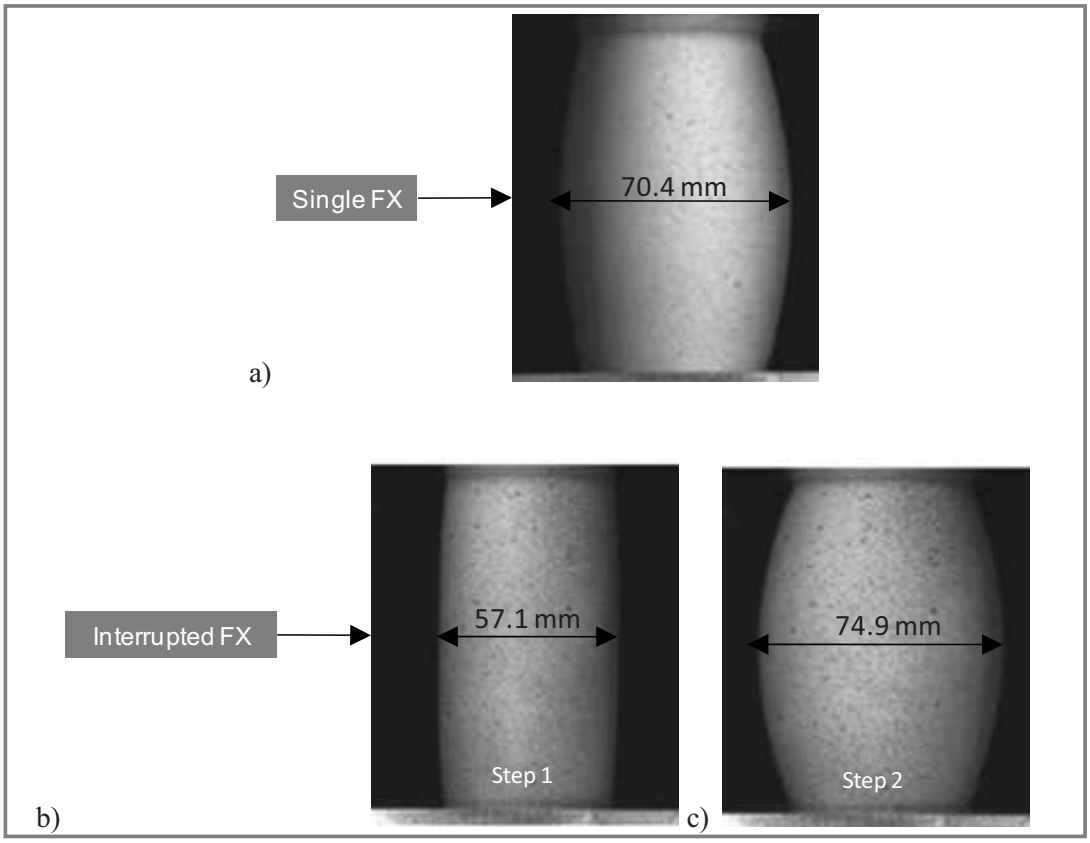

Figure 5.7 Comparison of the hydroformed tubes in the single and interrupted FX tests (From Aramis): a) at P_{Max} of the single test; b) at P_{Pause} of the interrupted test (step 1); c) at P_{Max} of the interrupted test (step 2)

5.5 Conclusions

In this study, a multistep forming method was developed to increase the formability of stainless steel 321 for hydroforming applications. Interrupted free expansion tests combined with an intermediate heat treatment were conducted as a representation of the multistep forming process. It was shown that by adding a stress relief heat treatment in between the two forming steps, the radial expansion of the 50.8 mm diameter tube increased by 26%. This indicates that multistep forming is an effective approach to reach higher levels of deformation. Also it was observed that the internal pressure required to deform the tubes up to the burst point in the second forming step was reduced by almost 20%.

5.6 References

Anderson, M., J. Gholipour, P. Bocher, F. Bridier, J. Savoie et P. Wanjara. 2010. « Formability extension of aerospace alloys for tube hydroforming applications ». *International Journal of Material Forming,* vol. 3, n° SUPPL 1, p. 303-306.

Chandler, Harry. 1995. *Heat treater's guide : practices and procedures for irons and steels*, 2nd. Materials Park, OH: ASM International, vii, 903 p.

Chen, K. K., R. J. Soldaat et R.M. Moses. 2004. *Free expansion bulge testing of tubes for automotive hydroform applications*. SAE technical paper No. 2004-01-0832. Warrendale, Pennsylvania.

Gholipour, Javad, Michael J. Worswick et D. Oliviera. 2004. *Application of damage models in bending and hydroforming of aluminum alloy tube*. SAE technical paper No. 2004-01-835. Warrendale, Pennsylvania.

Groche, P., R. Huber, J. Dörr et D. Schmoeckel. 2002. « Hydromechanical Deep-Drawing of Aluminium-Alloys at Elevated Temperatures ». *CIRP Annals - Manufacturing Technology,* vol. 51, n° 1, p. 215-218.

Kleiner, M., M. Geiger et A. Klaus. 2003. « Manufacturing of Lightweight Components by Metal Forming ». *CIRP Annals - Manufacturing Technology,* vol. 52, n° 2, p. 521-542.

Koç, Muammer, Yingyot Aue-u-lan et Taylan Altan. 2001. « On the characteristics of tubular materials for hydroforming - experimentation and analysis ». *International Journal of Machine Tools and Manufacture,* vol. 41, n° 5, p. 761-772.

Kuwabara, T., M. Ishiki, M. Kuroda et S. Takahashi. 2003. « Yield locus and work hardening behavior of a thin-walled steel tube subjected to combined tension-internal pressure ». *J. Phys. IV France,* vol. 105, p. 347-354.

Lang, L. H., Z. R. Wang, D. C. Kang, S. J. Yuan, S. H. Zhang, J. Danckert et K. B. Nielsen. 2004. « Hydroforming highlights: sheet hydroforming and tube hydroforming ». *Journal of Materials Processing Technology,* vol. 151, n° Copyright 2004, IEE, p. 165-77.

Levy, B. S., C. J. Van Tyne et J. M. Stringfield. 2004. « Characterizing steel tube for hydroforming applications ». *Journal of Materials Processing Technology,* vol. 150, n° 3, p. 280-289.

Zhang, S. H. 1999. « Developments in hydroforming ». *Journal of Materials Processing Technology,* vol. 91, n° 1-3, p. 236-244.

Anderson, M., J. Gholipour, P. Bocher, F. Bridier, J. Savoie and P. Wanjara. 2010. « Formability extension of aerospace alloys for tube hydroforming applications ». *International Journal of Material Forming,* vol. 3, n° SUPPL 1, p. 303-306.

Chandler, Harry. 1995. *Heat treater's guide : practices and procedures for irons and steels*, 2nd. Materials Park, OH: ASM International, vii, 903 p.

Chen, K. K., R. J. Soldaat and R.M. Moses. 2004. *Free expansion bulge testing of tubes for automotive hydroform applications*. SAE technical paper No. 2004-01-0832. Warrendale, Pennsylvania.

Gholipour, Javad, Michael J. Worswick and D. Oliviera. 2004. *Application of damage models in bending and hydroforming of aluminum alloy tube*. SAE technical paper No. 2004-01-835. Warrendale, Pennsylvania.

Groche, P., R. Huber, J. Dörr and D. Schmoeckel. 2002. « Hydromechanical Deep-Drawing of Aluminium-Alloys at Elevated Temperatures ». *CIRP Annals - Manufacturing Technology,* vol. 51, n° 1, p. 215-218.

Kleiner, M., M. Geiger and A. Klaus. 2003. « Manufacturing of Lightweight Components by Metal Forming ». *CIRP Annals - Manufacturing Technology,* vol. 52, n° 2, p. 521-542.

Koç, Muammer, Yingyot Aue-u-lan and Taylan Altan. 2001. « On the characteristics of tubular materials for hydroforming - experimentation and analysis ». *International Journal of Machine Tools and Manufacture,* vol. 41, n° 5, p. 761-772.

Kuwabara, T., M. Ishiki, M. Kuroda and S. Takahashi. 2003. « Yield locus and work hardening behavior of a thin-walled steel tube subjected to combined tension-internal pressure ». *J. Phys. IV France,* vol. 105, p. 347-354.

Lang, L. H., Z. R. Wang, D. C. Kang, S. J. Yuan, S. H. Zhang, J. Danckert and K. B. Nielsen. 2004. « Hydroforming highlights: sheet hydroforming and tube hydroforming ». *Journal of Materials Processing Technology,* vol. 151, n° Copyright 2004, IEE, p. 165-77.

Levy, B. S., C. J. Van Tyne and J. M. Stringfield. 2004. « Characterizing steel tube for hydroforming applications ». *Journal of Materials Processing Technology,* vol. 150, n° 3, p. 280-289.

Zhang, S. H. 1999. « Developments in hydroforming ». *Journal of Materials Processing Technology,* vol. 91, n° 1-3, p. 236-244.

CHAPTER 6

PAPER 4: δ PHASE PRECIPITATION IN INCONEL 718 AND ASSOCIATED MECHANICAL PROPERTIES

M. Anderson[1], A-L. Thielin[1], F. Bridier[1,2], P. Bocher[1], J. Savoie[3]

[1]Ecole de Technologie Superieure, Mechanical Engineering Department, Montreal, Canada
[2]DCNS Research, DCNS Nantes-Indret, France
[3]Pratt & Whitney Canada, Special Process Development Group, Longueuil, QC, Canada

Article published in Materials Science & Engineering A, Volume 679, No. 1, pp.48-55, 2017.

Abstract

Microstructures generated by δ phase precipitation in Inconel 718 (IN718) and related mechanical properties were investigated in this paper. Several heat treatments enabling the precipitation of the δ phase in various proportions were conducted. Heat treatments were performed in a temperature range between 875°C and 975°C with time durations from 0.5 to 24 hours. For each test, the microstructures were characterized and the volume fraction of the δ precipitates quantified. In parallel, uniaxial tensile tests were conducted in order to determine the mechanical properties of the alloy, namely the elongation at necking (N%), the yield strength (YS), the Vickers hardness (HV) and strain hardening coefficients (K, n). The results revealed that when γ'' and δ precipitates coexist, the material remains hardened regardless of the amount of δ phase. However, when only δ phase were presented in the matrix, its volume fraction did not significantly affect the formability of the material. It was observed that the ratio between intragranular and intergranular precipitates could be a critical parameter. Intergranular precipitates, when in sufficient amount, led to a better formability of the material. On the contrary, when the intragranular precipitates were maximized, they tend to harden the material. A solution treatment at 975°C for 2 hours was finally suggested as the best compromise to improve the formability of IN718.

6.1 Introduction

IN718 is a Nickel-Iron base superalloy belonging to the medium to high temperature class. It is widely used in gas turbines and aerospace engines because of its excellent mechanical properties as well as its corrosion resistance from cryogenic to elevated temperatures (~650°C) (Li et al., 2002; Slama andAbdellaoui, 2000). However, its complex microstructure combined with the tight tolerances required in the aerospace industry restricts its usage in several forming processes. The purpose of the present publication is to correlate microstructural features of IN718 with several heat treatment conditions and associate them with specific static mechanical properties in order to reach higher ductility. In particular, the effect of d phase precipitation state will be investigated and related to the mechanical properties of the obtained microstructure.

IN718 consists of a FCC γ–matrix with δ phase, MC carbides, few γ' and a high volume fraction of embedded γ'' precipitates (Slama andCizeron, 1997; Song andHuh, 2007; Totten, 2007). Contrarily to most of the superalloys, its main hardening phase is the coherent γ'' (Ni_3Nb) phase with body-centered tetragonal crystal structure. The γ' [$Ni_3(Al,Ti)$] with $L1_2$ structure brings additional strength to the alloy but at a lower degree (Paulonis, Oblak andDuvall, 1969; Slama andCizeron, 1997; Totten, 2007). For longer ageing time or for temperatures higher than 650°C, the metastable phase γ'' transforms into the stable δ phase (Ni_3Nb) with orthorhombic structure. The δ phase precipitates at grain and twin boundaries and in an intragranular manner with a plate shaped or globular morphology (Cai et al., 2007; Sundararaman, Mukhopadhyay andBanerjee, 1988). Since γ'' and δ have the same composition, the growth of the δ phase occurs with the corresponding loss of the γ'' phase (Azadian, Wei andWarren, 2004). Several authors have detailed the precipitation ranges for the main phases of IN718 and a few TTT diagrams (Temperature-Time-Transformation) have been drawn (Garcia et al., 1992; Geng, Na andPark, 1997; Niang, Viguier andLacaze, 2010; Oradei-Basile andRadavich, 1991). According to many authors, the γ' and γ'' phases precipitate between 600 and 900°C, whereas the highest level of δ precipitation is found

around 900°C (Azadian, Wei andWarren, 2004; Niang, Viguier andLacaze, 2010; Sundararaman, Mukhopadhyay andBanerjee, 1988). Beaubois et al. (Beaubois et al., 2004) have found the "nose" of the TTT curve for δ precipitation between 910 to 920°C after 0.2 and 0.4 hours, respectively. The effect of cooling rates have been studied by Geng et al. (Geng, Na andPark, 1997) and Slama et al. (Slama andCizeron, 1997) and they concluded that cooling rates between 5 and 100°C/s should be considered in order to precipitate maximum amount of δ phase.

It has been reported that the formation of large amounts of coarse δ plates degrades the strength of the superalloys hardened by γ'' precipitates due to the corresponding depletion of the γ'' phase (Sundararaman, Mukhopadhyay andBanerjee, 1988). The morphology of the δ phase is not known to allow any significant contribution to the hardening of these alloys (Azadian, Wei andWarren, 2004; Valle et al., 2013). It had also been reported that the presence of the δ phase decreases yield and tensile strengths but has a beneficial effect on the rupture ductility (Corporation, 2007, p. 9; Rao et al., 2003). Similar conclusion were drawn for creep and fatigue properties (Desvallées et al., 1994; Huang andLangdon, 2007; Kuo et al., 2009). However, very few studies report the possible relationship between the δ phase content and the formability of the material at room temperature. Only Valle et al. (Valle et al., 2013) studied the influence of the volume fraction of δ–phase obtained from aged samples on the mechanical properties such as yield and tensile strengths, elongation, and hardness. They have shown that 0.2 to 1.5% δ phase do not influence the mechanical properties of aged samples. No study has been conducted for higher amount of δ precipitates to confirm the general assumption that the presence of δ phase precipitation in IN718 induced a ductility improvement in the material.

The present work partly aims at studying this particular point. Several heat treatments generating the δ precipitation have been performed. In the present investigation, δ volume fraction range between 0 to 15.5% is targeted as in (Talonen et al., 2005). Microstructures

analysis as well as δ phase quantification by image analysis had been performed and related to the tensile testing results in order to determine their interrelations.

6.2 Experimental procedure

6.2.1 Materials

The chemical composition of the IN718 used in the present work is given in Table 6.1. The material was provided in 0.9 mm thick sheet form by Pratt & Whitney Canada. The microstructure of the as-received material is presented in **Erreur ! Source du renvoi introuvable.**. The average grain size is about 10 µm. It can be observed that no precipitates were present in the as-received material indicating that the matrix is supersaturated in alloying elements. This state of material is the result of a very high cooling rate from high temperature (Niang, Viguier andLacaze, 2010).

Table 6.1 Chemical composition of as-received IN718 sheet

Element	Ni	Fe	Cr	Nb	Mo	Ti	Al	Si
Wt. %	52.85	17.81	18.74	5.18	3.02	1.1	0.35	0.07

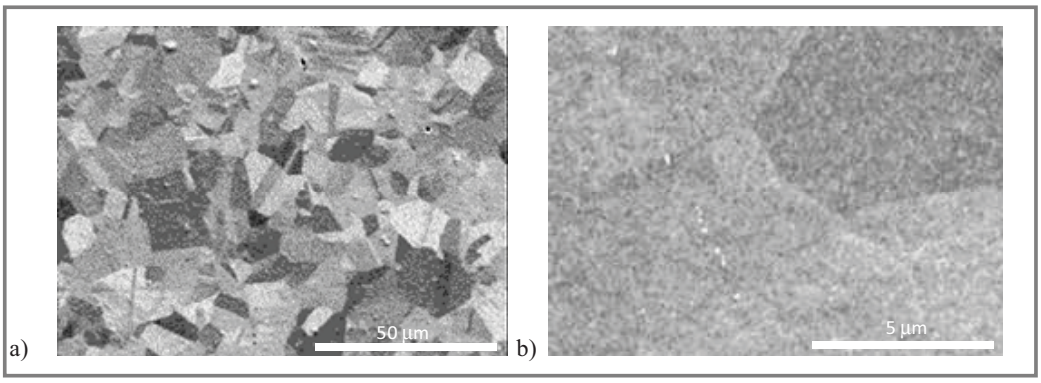

Figure 6.1 SEM images of IN718 in as received conditions (a) as polished x 500, (b) Etched (8ml H2SO4, 100ml H_2O) x 5000

6.2.2 Heat treatments

The heat treatment sequences conducted were established based on δ phase precipitation rate to ensure its maximization. They were performed between 875°C and 975°C for time durations from 0.5 to 24hours (Table 6.2). Due to the limited amount of test pieces, some durations have been deliberately bypassed. It has been considered that they will be covered by the global trend. The heat treatments were carried out in an air furnace on samples of dimensions 10 x 15 x 0.9 mm3. A type K thermocouple was spot welded to a test sample with close geometry as the objective specimens to accurately control the temperature. The heat treatment duration was timed as soon as the sample entered the hot furnace. A heating time of 5 min from room temperature to the required temperature was noted. At the end, the specimens were water quenched. The sequences tested made possible to reach δ volume fractions from 0.3 to 15.5% as detailed later.

Table 6.2 Heat treatments performed on Inconel 718 specimens

	875°C	900°C	925°C	950°C	975°C
0.5h	✓	✓	✓	✓	✓
2h	✓	✓	✓	✓	✓
6h		✓		✓	
12h		✓		✓	
24h	✓	✓	✓	✓	✓

6.2.3 Metallographic preparation

The specimens prepared for microstructural characterization were polished using conventional metallographic preparation techniques. A final polishing was performed in a Vibrometer® for 24 hours with colloidal silica. To reveal the γ' and γ'' phases some of the specimens underwent an electrolytic etch (8 ml H_2SO_4 + 100 ml H_2O) at 10V for ten seconds

as per (Chamanfar et al., 2013). All the metallographic investigations and microstructure analyses were performed with a high resolution Hitachi SU-70 field emission gun - scanning electron microscope (FEG-SEM) operated at 20kV with a probe current of 14nA.

6.2.4 Image analysis

The δ phase particles were quantified by image analysis from a series of backscattered electron (BSE) micrographs. The images were taken at a magnification of x1000 and 5120 x 3585 pixels which had been found appropriate to clearly detect the δ precipitates with sufficient image resolution for analysis. The methodology applied has been detailed elsewhere (Vanderesse et al., 2016). The free, open-source image analysis software application Fiji, based on ImageJ, was used (Schneider, Rasband andEliceiri, 2012). A specific code applying a sequence of various processing operations was implemented, making it possible to analyze automatically a large series of images. This sequence involved background correction by means of an FFT-based bandpass filter, denoising using a mean shift filter (Barthel, 2007), manual thresholding, and removal of extra small particles with a size of 3x3 pixels (being ~ 0.075 μm^2). Furthermore, it was possible to separate intergranular and intragranular precipitates using the structure tensor properties of the images (Grannlund andKnutsson, 1995). It was found that a number of 3 images of 121 x 85 μm^2 was enough for statistical analyses of each treatment. The area fraction and the local thickness, i.e., the average size of the particles, were measured. In 2D, the local thickness is defined as the median diameter of the disc that fits inside the particle. This method is similar to the classical intercept method generally used in quantitative metallography but does not require prior estimation of the orientation.

6.2.5 Uniaxial micro tensile tests and micro hardness measurements

The deformation under mechanical loading was studied through uniaxial tensile tests. Tests were done with a microtesting machine using flat micro tensile specimens with 13 mm gauge length for 4 mm width (Figure 6.2). A mechanical extensometer with a maximum

displacement of 1 mm was installed. The strain rate was 0.03 s^{-1} with a sampling period of 20 ms. Because of the limited range of the extensometer, the tests were performed in several steps which correspond to a relocation of the extensometer. Former microscale tensile tests showed that the interruption does not affect the curve values: the stress-strain curves obtained with the microtensile machine are close to the ones acquired with standard ASTM specimens (Figure 6.3). The yield strength (YS), the ultimate tensile strength (UTS) as well as the necking strain (N %) were evaluated for all performed tensile stress-strain curves.

Vickers microhardness (HV) testing was also conducted according to ASTM E92. The load applied was 300 g for 30s. The hardness values were an average of 5 measurements per sample.

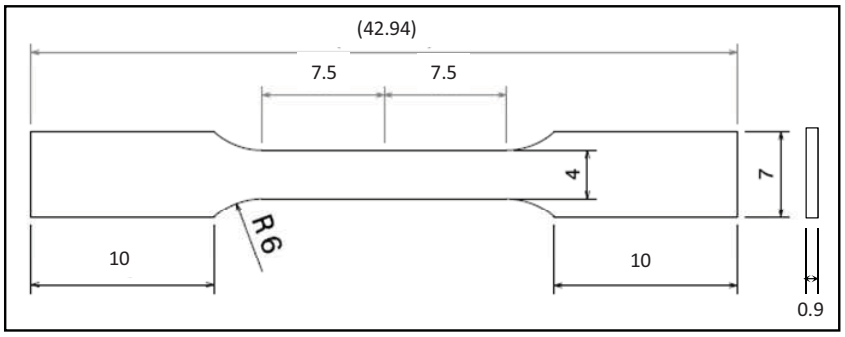

Figure 6.2 Microscale tensile specimen

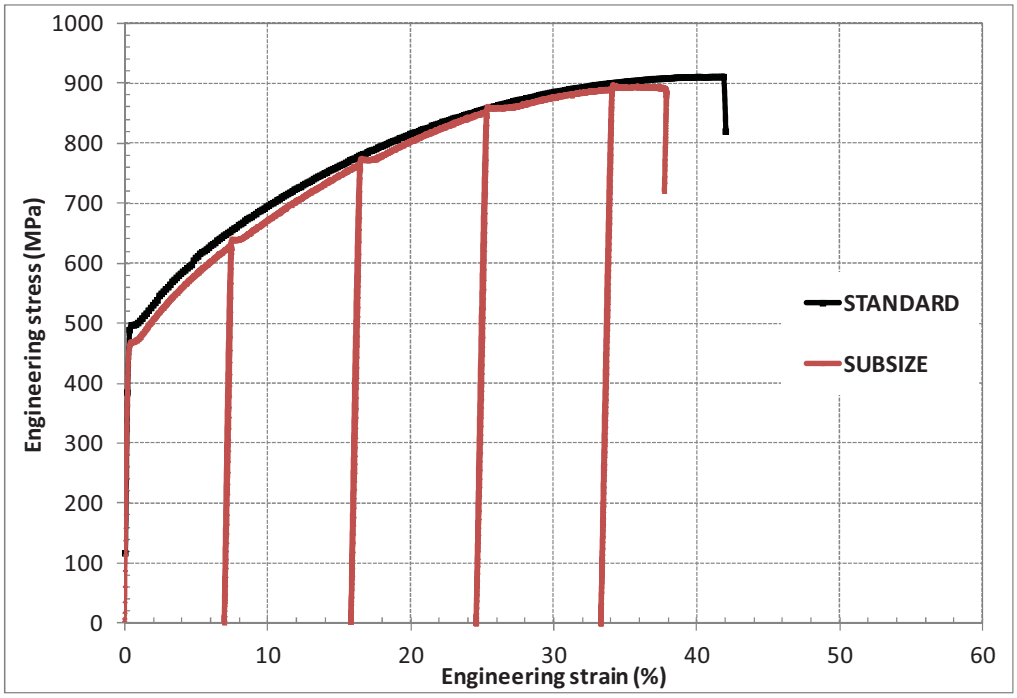

Figure 6.3 Stress strain curves comparison: ASTM standard specimen vs. microscale tensile test

6.3 Results and discussion

6.3.1 Microstructures analysis

The general sequence of δ phase precipitation is illustrated in Figure 6.4. The total amount of δ precipitates varied considerably with the heat treatment. At the minimum temperature tested (875°C), very few precipitates are observed regardless of the duration time. At 900°C, the amount of δ phase seems maximized. With further increased temperatures, the δ phase quantity decreased. Two types of δ precipitates are observed and have been identified thanks to SEM imaging at high magnification. In a given grain, the intragranular δ precipitates were organized in clusters of parallel plates whereas the intergranular were most of the time isolated at grain boundaries. In addition, the intergranular were brighter than the intragranular ones because of their larger size. The δ precipitation seems to start as intergranular single

precipitates at the grain boundaries. As the temperature and/or heat treatment duration increase, the intragranular δ precipitates appear. In Figure 6.4-a, which corresponds to the lowest temperature and heating duration, few δ phase precipitates are present. The intergranular precipitates are spread across the matrix and are very small (138 ± 20 nm). Few intragranular precipitates are also found. Their size is about 83 ± 25 nm. On top of that, at this temperature (875°C), γ'' precipitates have been found as shown in Figure 6.5 and not at higher temperatures. In Figure 6.4-b corresponding to a 900°C/24h, a very high amount of δ precipitates are observed both at the grains boundaries and within the grains and no γ'' were found. The intergranular precipitates are thicker (280 ± 20 nm) and the intragranular (181 ± 20 nm), more elongated, growing from the boundaries inside the grains in various directions and in some cases across the whole grain. As the temperature increases, in Figure 6.4-c corresponding to a 950°C/6h, the amount of δ precipitates decreases. The intergranular precipitates presented are very thick (379 ± 25 nm) as well as the intragranular ones (153 ± 20 nm). Finally, Figure 6.4-d corresponding to a 975°C/2h presents thick intergranular precipitates (296 ± 20 nm) well distributed at the grain boundaries whereas the matrix was almost exempt of intragranular (99 ± 20 μm).

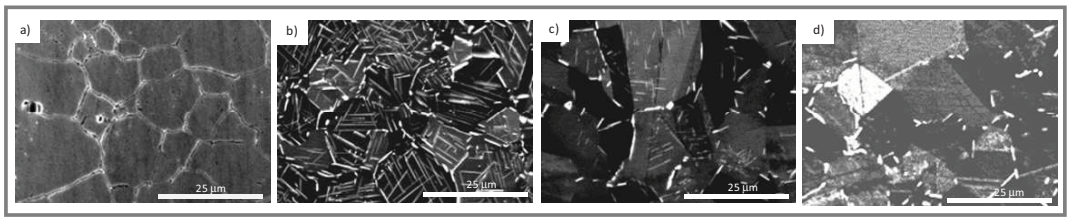

Figure 6.4 SEM images of IN718 after heat treatments showing the δ phase precipitation variation:
a) 875ºC / 0.5h, b) 900ºC / 24h, c) 950ºC / 6h and d) 975ºC / 2h

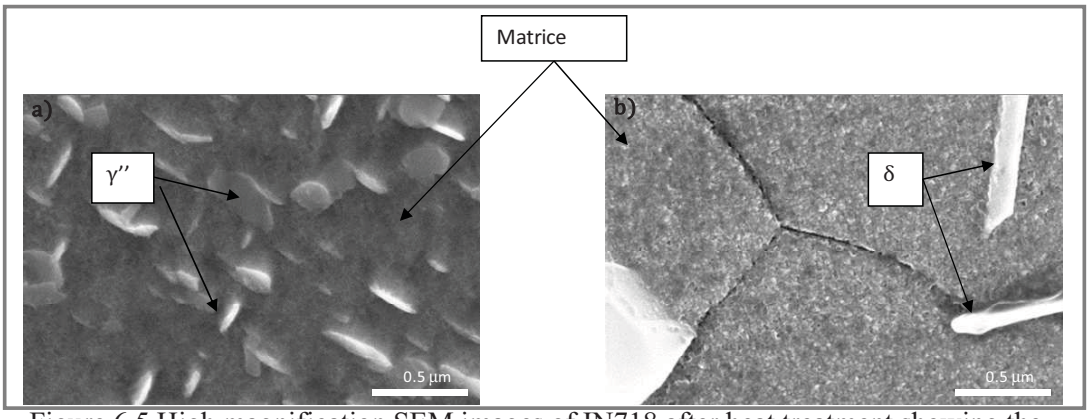

Figure 6.5 High magnification SEM images of IN718 after heat treatment showing the presence of γ'' precipitates in a) 875°C / 2h, or not in b) 925°C / 2h

6.3.2 Quantitative analysis of δ phase precipitation

In the studied time/temperature ranges, the δ precipitates volume fractions were high enough to make quantitative measurements possible. The general sequence of δ precipitation illustrated in Figure 6.4 is plotted in Figure 6.6. As detailed earlier, certain conditions of time and temperature have been ignored but this gap does not impacted the general trend of δ phase precipitation. Error bars correspond to the minimum and maximum values measured at each step. For very short heat treatment times or low temperatures, very few δ precipitates are present. As time increases at a given temperature, some δ precipitates appear within the matrix. The highest precipitation volume is reached at 900°C during 24h and is about 15%. The treatments at 950 and 975°C exhibit lower precipitation rates and amounts. These results are in good agreement with Azadian et al. (Azadian, Wei andWarren, 2004) (added in Figure 6.6). The conclusions of Azadian et al. (Azadian, Wei andWarren, 2004) who tested longer times suggest that the equilibrium fractions were not reached for the treatment durations tested in the present work.

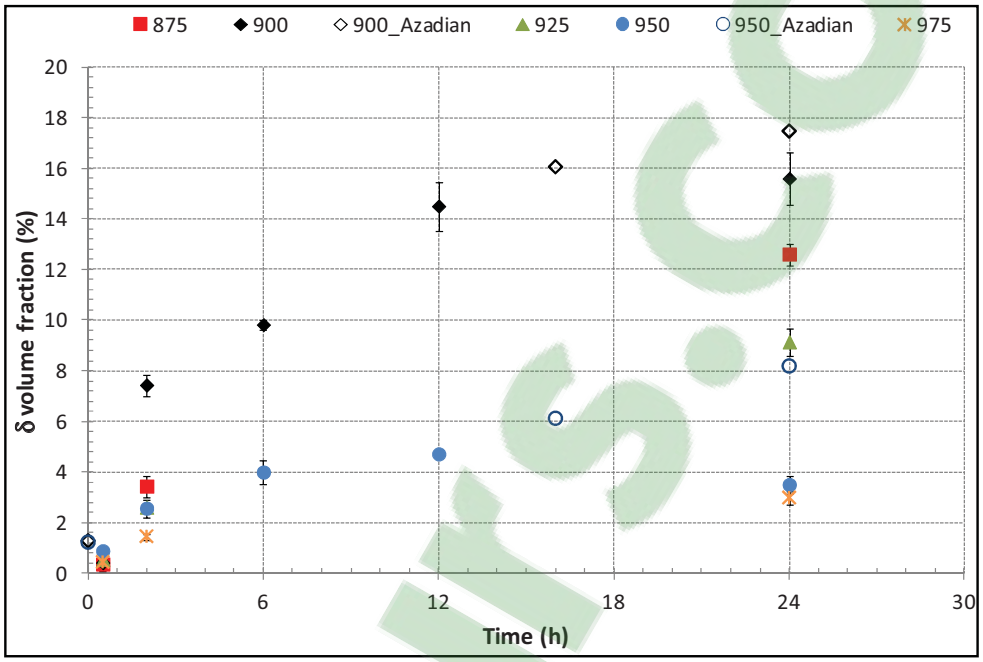

Figure 6.6 δ phase volume fraction evolution as a function of time and temperature. Data from Azadian, Wei and Warren. (2004) added

The δ phase quantification has been extended to the identification of the precipitate morphology and position in the grain structure. It has previously been detailed that two types of precipitates can be distinguished, globular and elongated at the grain boundaries and acicular inside the grains. The histograms in Figure 6.7 show the δ volume fractions specific to each type of precipitates for the 0.5, 2 and 24 hours heat treatments. They can be linked to the SEM micrographs in Figure 6.8 used through image analysis for δ quantification. For each type of precipitates, the volume fraction increases with the treatment duration. At 0.5 hours, a very small amount of δ phase is present, regardless of the temperature. As the heat treatment time increases, at a given temperature, the rate of intragranular δ precipitation is more pronounced than the one of intergranular precipitates until 925°C. In other words, the total amount of δ phase obtained comes from the intragranular precipitates. At higher temperatures (950 and 975°C), not only the volume fraction of δ phase is globally reduced but also the ratio between intergranular and intragranular precipitates decreases. The intergranular δ volume fraction increases rapidly and do not vary much after several hours,

while the volume fraction of intragranular precipitates continues to increase with the treatment duration. For short heating times, except at 875°C, the amount of intergranular precipitates is greater compared to the intragranular ones; this corresponds to the nose of the precipitation curve in the TTT diagram (Niang, Viguier andLacaze, 2010).

The highest ratio of intergranular over intragranular volume fraction is obtained at 975°C/2h despite the relatively low level of total δ precipitates. For this heat treatment, the amount of intergranular precipitates is predominant relative to the intragranular ones. On the contrary, the 900°C/24h heat treatment presents the maximum volume fraction of δ and reveals a majority of intragranular δ precipitates

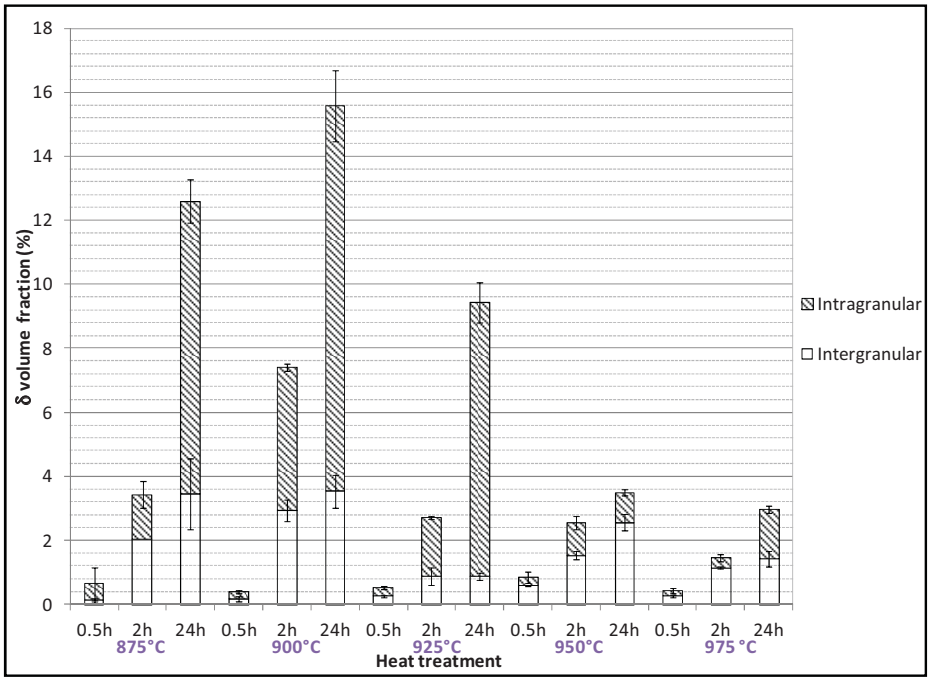

Figure 6.7 δ phase volume fraction distribution as a function of the heat treatment

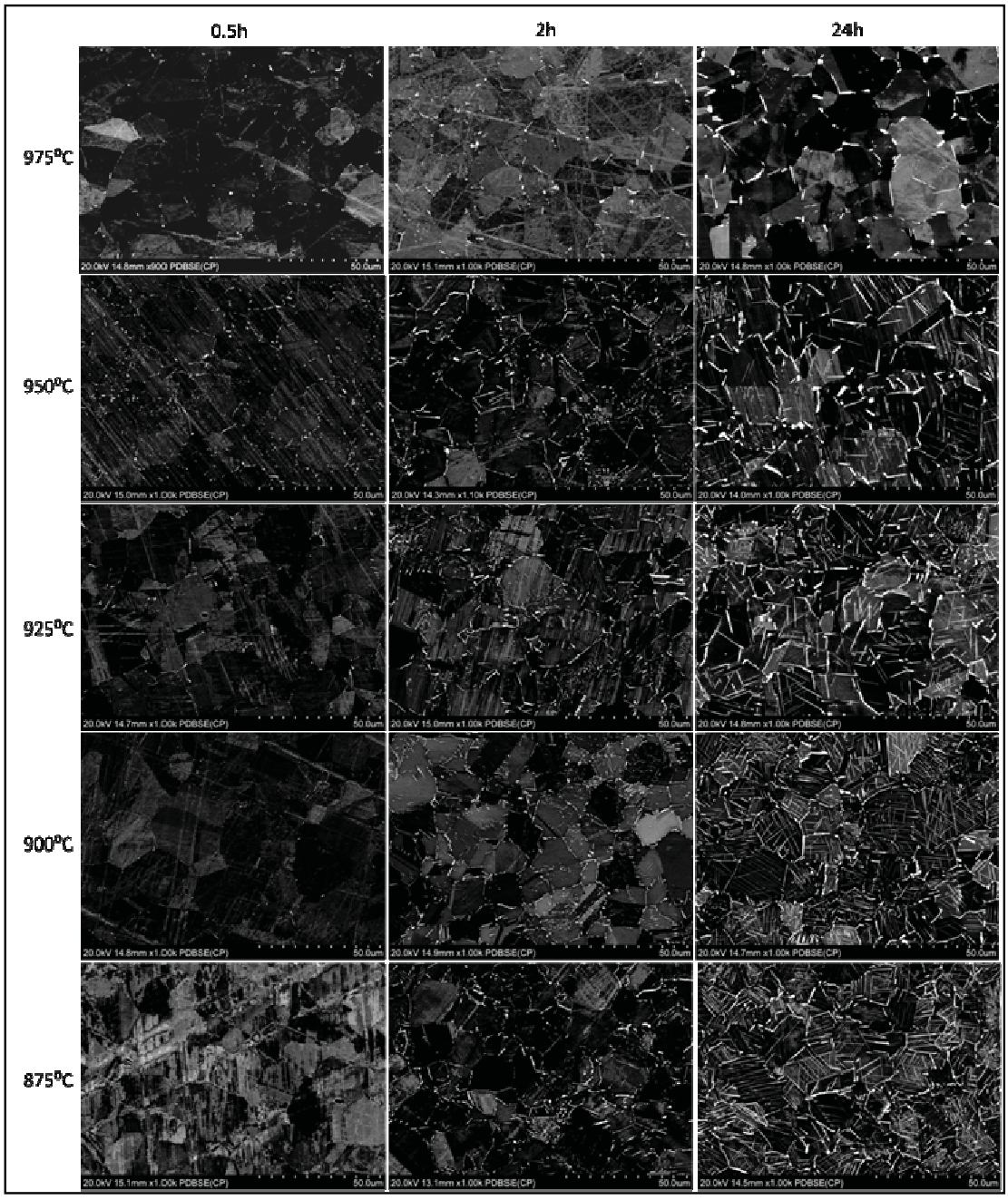

Figure 6.8 SEM images (before image analysis) of IN718 after heat treatments using for δ phase quantification

6.3.3 Stress-strain curves

The stress strain curves for all the heat treatment conditions had been acquired to determine the formability potential of the obtained microstructures. In this study, the limit of formability is defined as to the level of deformation (N%) corresponding to the onset of localized necking in tensile test (Panda et al., 2007). This method represents the easiest way to measure formability even if a test done under a uniaxial strain field may not necessarily represent the actual manufacturing process to be documented.

Figure 6.9 shows the stress-strain curves of the specimens at various temperatures for 2 hours heat treatment durations. The purpose of this figure is to study the temperature impact on mechanical properties. Comparing these five samples shows that YS decreases with increasing heat treatment temperatures but, the change in N% is not systematic. The minimum N% is obtained for the lowest temperature whereas the maximum N% is reached with the highest temperature tested. However, in between, for 900, 925 and 950°C, N% is very close from each other (represented in Figure 6.9 by the arrows) and the 925 and 950°C N% are almost identical.

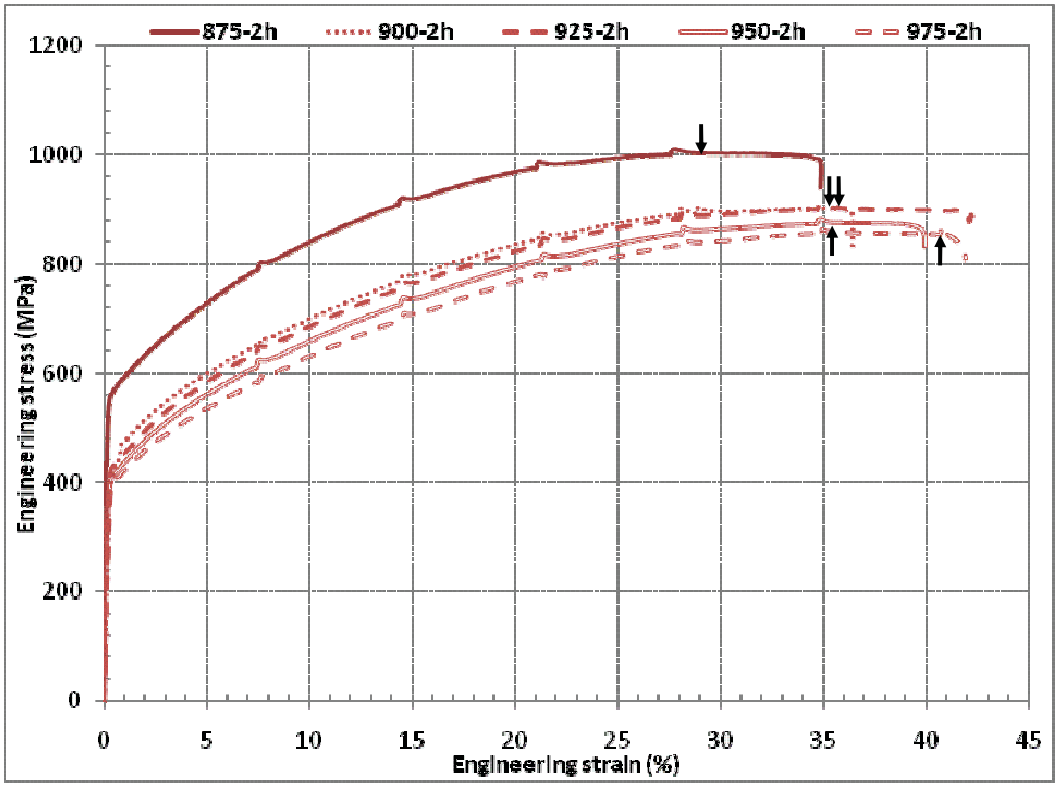

Figure 6.9 Stress strain curves comparison for various temperatures at 2h heating time

Table 6.3 details the YS and N% obtained for all the heat treatments performed. It can be observed that the heat treatments with the less formability enhancement are at 875°C and the values are far from the others: the YS is 20% higher and the N% 30% lower than the average at any given heat treatment duration. Actually, this microstructural condition (875°C, any duration) gives the minimum formability. This results from the fact that the material is hardened because of the presence of the hardening γ'' precipitates as evidenced in the microstructure analysis (Figure 6.5). At this temperature, the γ'' phase coexisting with the δ phase can explain the limited formability of the material. Based on the TTT diagram, it actually corresponds to conditions for which the precipitation curves of δ and γ'' precipitates cross each other (Beaubois et al., 2004). Conversely, the formability is maximized for the heat treatment at 975°C / 2 hours. Based on the microstructural analysis, the main specificity

of this heat treatment is its highest ratio of intergranular δ precipitates over intragranular ones. For the other heat treatments, YS and N% remain globally in the same range.

Table 6.3 Tensile mechanical properties (YS, N%), as a function of the heat treatment

	YS					N%				
	875°C	900°C	925°C	950°C	975°C	875°C	900°C	925°C	950°C	975°C
0.5h	613	469	443	413	424	25.4	34.9	36.6	34.9	35.0
2h	572	477	431	409	403	27.7	35.6	34.8	34.8	40.8
24h	531	505	450	439	383	27.6	31.6	35.2	34.5	34.9

In Figure 6.10, three relevant stress-strain curves were compared: the curve giving the lowest formability (875°C/ 0.5 hours), the curve giving the maximum formability (975°C/ 2 hours) and the curve obtained when the δ phase amount is maximized (900°C/ 24 hours). The heat treatment resulting in the maximization of the amount of δ phase does not bring any formability improvement. Actually, the mechanical hardening behavior appears very close to the stress strain curve with minimum formability. The N% of 32% is among the lowest values obtained in the campaign and the YS relatively low (505 ± 4 MPa). The process leading to the highest formability (975°C/2h) does not contain a large amount of δ precipitates, only 1.4%. This means that even if the precipitation of δ phase is associated with the loss of hardenability of IN718, the type and amount of δ precipitates should be taken into account specifically when formability improvement is targeted.

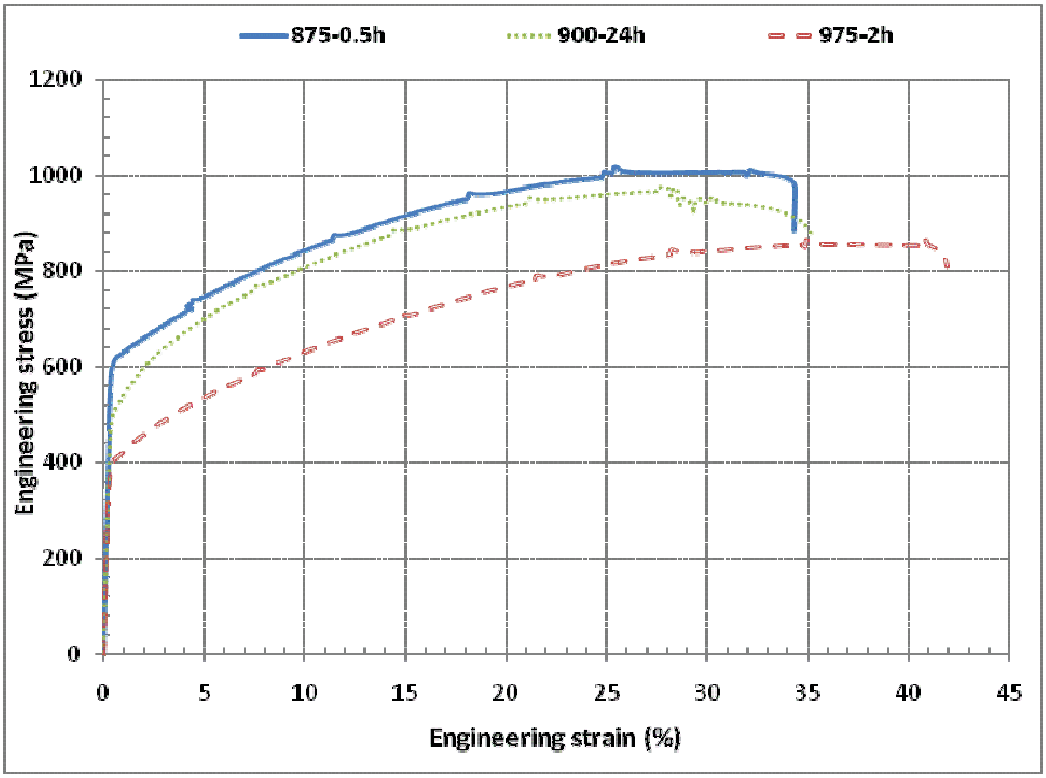

Figure 6.10 Stress strain curves comparison: 875°C / 0.5h (Minimum N% - Maximum YS), 975°C / 2h (Maximum N% - Minimum YS) and 900°C / 24h (Maximum δ)

6.3.4 Mechanical properties

To better document the relationship between δ phase precipitation and mechanical properties, YS, N%, and HV variations were plotted as a function of the heating temperatures for various heat treatment durations in Figure 6.11, Figure 6.12 and Figure 6.13, respectively.

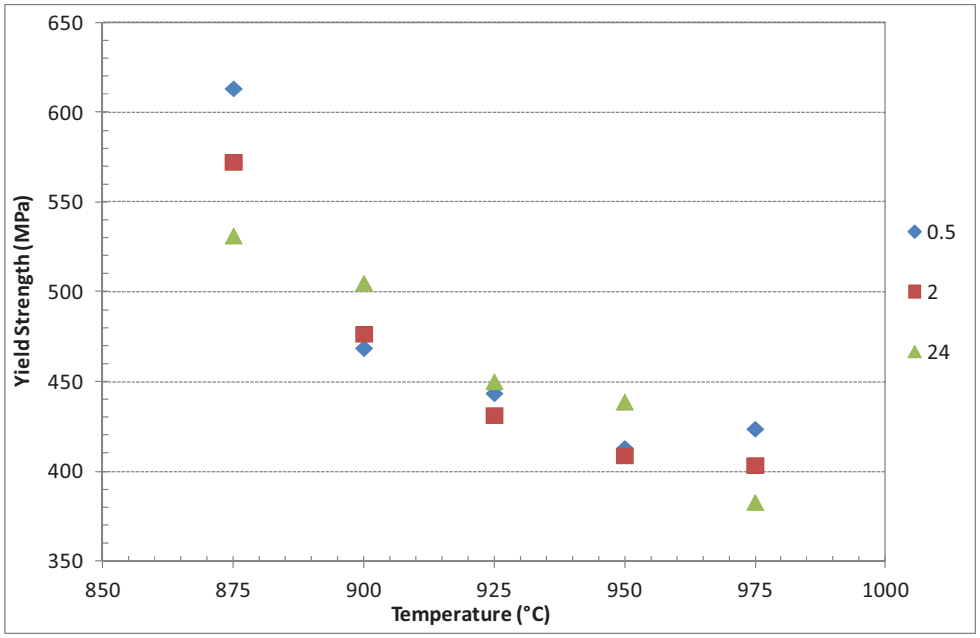

Figure 6.11 Yield strength (YS) evolution as a function of the heat treatment

It can be observed in Figure 6.11 that for a given heat treatment duration, YS decreased with the temperature. At the minimum and maximum temperatures (875°C and 975°C), YS decreased with the time. On the contrary, at 900, 925 and 975°C, the highest level of YS is reached after 24 hours heat treatment. At 875°C, the longer the heat treatment duration, the more likely it is to transform γ'' precipitates to non-hardening δ phase which shortens YS. Starting at 950°C, at each temperature, the ratio between the types of δ precipitates (intergranular vs. intragranular) had an influence on YS evolution as a function of heat treatment time. The longest heat treatments (24 hours) induced an important precipitation of intragranular δ precipitates which prevented the dislocation motion. As a result, YS is increased. Beyond 900°C, the global volume fraction of δ precipitates decreased which implies a decrease in the detrimental effect of intragranular δ precipitates on mechanical properties. At 975°C, regardless of the heat treatment duration, few δ precipitates are generated within the matrix, especially the prejudicial intragranular ones which precipitate afterwards.

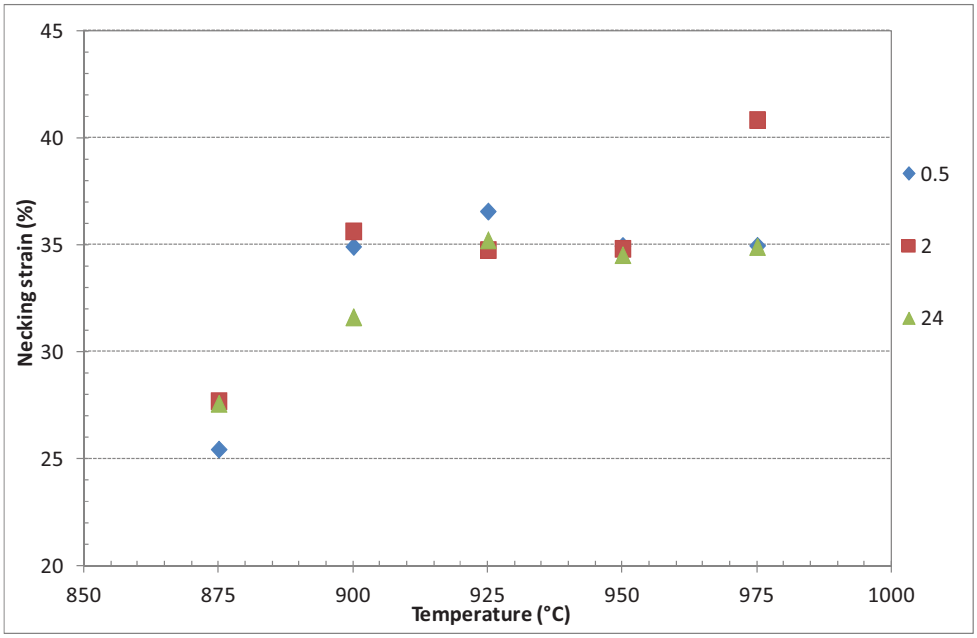

Figure 6.12 Necking strain (N%) evolution as a function of the heat treatment

In Figure 6.12, the necking strain varies from 25% to 41% depending on the heat treatment. Nevertheless, the majority of the measurements are around 35%, except for the treatment at 975°C for 2 hours and lower values obtained at 875°C as γ'' precipitates are present (as discussed earlier). Thus, the δ precipitation does not appear to have a notable effect on N% except for its maximum value which is obtained for a very low value of δ phase volume fraction. However, when the total amount of δ phase is maximized, its impact on the formability is deleterious and comparable to the γ'' precipitates effect. This can be explained by the fact that high amounts of lamellar shape δ precipitates inside the grains stopped the dislocation movements and decreased the material formability.

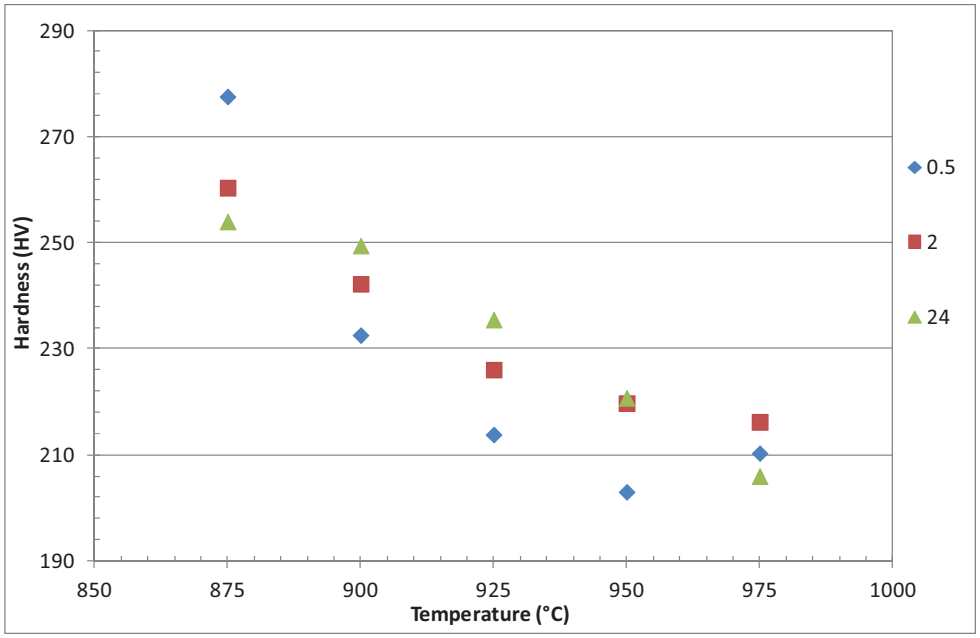

Figure 6.13 Vickers hardness (HV) evolution as a function of the heat treatment

Likewise, HV properties were studied as a function of the heat treatment to correlate their evolution with the δ phase precipitation in Figure 6.13. Both YS and HV presented a similar behavior. In the same way as YS, HV decreases with increasing the temperature. At 875°C as well, the transformation from γ'' to δ phase as the heat treatment duration increased resulted in the drop of HV. At 900°C, when the δ phase is maximized, HV is high because of the large amount of intragranular precipitates which pinned the dislocations and hindered their movement. At higher temperatures, as the total amount of δ precipitates globally decreased, the effect of the heat treatment duration on HV measurements is lowered. These measurements being completely independent of the stress-strain curves, it confirms the formability behavior of IN718 when subjected to δ phase precipitation.

6.3.5 Hardening behavior

The stress-strain curves and strain hardening behavior of metallic materials are usually described by mathematical expressions like $\sigma_P = f(\varepsilon_P)$. The most common expression is the

Hollomon hardening law but in case of cold working materials, the Swift law is assumed to be more appropriate (Anderson, 2010; Saboori et al., 2014). It consists in a power law relation $\sigma = K \times (\varepsilon_0 + \varepsilon_P)^n$ where *n* is a strain hardening exponent, ε_0 an initial strain and *K* a strength coefficient. The strain hardening coefficient has a physical meaning as it represents the susceptibility of a material to work hardening (the higher is the coefficient, the more the material hardens and the lower is the necking strain). Table 6.4-a brings together the K and n values obtained for all the tensile tests performed whereas Table 6.4-b shows the ε_0 as well as the coefficient of determination (R^2) calculated by ordinary least-squares regression method. As expected, the minimum n values are reached when the material contains γ''. On the contrary, the highest levels of strain hardening coefficient are obtained for very low δ volume fractions.

Figure 6.14 presented the δ volume fraction of each type of precipitates as a function of the strain hardening coefficient. The data corresponding to 875°C had been represented with empty bullet points. The effect of the type of precipitates is highlighted. The minimum n values, even at 875°C, are reached when the intragranular δ precipitates are maximized. As the amount of intragranular δ precipitates decreased in favor of the intergranular, the n values increased.

Table 6.4 Best fit coefficients of the Swift hardening equation a) K and n values

Swift $\sigma = K(\varepsilon_0+\varepsilon_P)^n$	K					n				
	875°C	900°C	925°C	950°C	975°C	875°C	900°C	925°C	950°C	975°C
0.5h	275	194	149	166	153	0.455	0.525	0.597	0.551	0.572
2h	339	206	219	183	164	0.400	0.508	0.489	0.529	0.552
24h	373	307	296	269	173	0.370	0.423	0.420	0.442	0.536

Table 6.5 (Cont'd): Best fit coefficients of the Swift hardening equation b) ε_0 and R^2

Swift $\sigma = K(\varepsilon_0+\varepsilon_P)^n$	ε_0					R^2				
	875°C	900°C	925°C	950°C	975°C	875°C	900°C	925°C	950°C	975°C
0.5h	5.046	4.531	5.760	4.542	4.830	0.9984	0.9981	0.9992	0.9980	0.9979
2h	2.887	4.199	3.338	4.210	4.463	0.9982	0.9985	0.9980	0.9982	0.9980
24h	2.089	2.999	2.437	2.523	4.297	0.9981	0.9986	0.9986	0.9961	0.9940

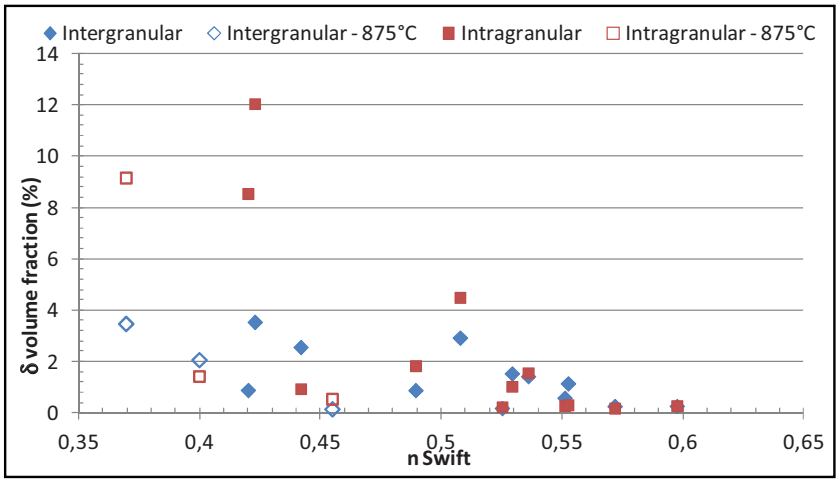

Figure 6.14: δ volume fraction as a function of the Swift strain hardening coefficient n

6.4 Conclusions

The objective of this work was to document the mechanical properties of IN718 when δ phase precipitation is at interest. Various δ phase precipitation microstructures were obtained using temperature ranging from 875°C to 975°C with durations from 0.5 to 24hours. Microstructural analysis combined with the mechanical tests results pointed out several facts. First, when both γ'' and δ phases are present in the matrix, after low temperature heat treatments (875°C), the material showed a limited formability due to the presence of γ'' precipitates and this was true regardless of the amount and morphology of the δ phase that

had formed. Secondly, two types of δ phase precipitates were found in the microstructure (intergranular and intragranular) and they had different influences on the mechanical properties of IN718. Thirdly, maximizing the amount of δ phase tends to harden the material because of the way δ precipitates grow intragranularly in the matrix (in parallel clusters) when higher temperatures and treatment times are used. Maximizing the volume fraction of intergranular δ precipitates (compared to the intragranular)tends to increase the ductility of the material by lowering the YS. On the other hand high amounts of intragranular precipitates lead to a significant hardening of IN718 and lower the ductility of the alloy. In order to increase IN718 ductility using heat treatments, the best conditions have been identified as 975°C for 2h followed by fast quench leading to a microstructure of no hardening γ'' phase, few δ precipitates with most of them intergranular.

6.5 Acknowledgements

The authors would like to extend their thanks to the Natural Sciences and Engineering Research Council of Canada (NSERC) CRD372801-08, the Consortium for Research and Innovation in Aerospace in Quebec under the CRIAQ 4.6 project and the Fonds Québécois de Recherche Nature et Technologies (FQRNT) 146549 for their financial support. The authors are also grateful to Dr Nicolas Vanderesse for his assistance and help on the image analysis software as well as Dr Jonathan Cormier for the meaningful discussions conducted during this work.

6.6 References

Anderson, Mélissa. 2010. « Tube hydroforming of aerospace alloys : material characterization methods ». Montréal, Canada, École de technologie supérieure.

Azadian Saied, Liu-Ying Wei and Richard Warren. 2004. « Delta phase precipitation in Inconel 718 ». *Materials Characterization,* vol. 53, n^{o} 1, p. 7-16.

Barthel, Kai Uwe. 2007. « http://rsbweb.nih.gov/ij/plugins/mean-shift.html ». Consulted on 2013/11/20.

Beaubois, V., J. Huez, S. Coste, O. Brucelle and J. Lacaze. 2004. « Short term precipitation kinetics of delta phase in strain free Inconel* 718 alloy ». *Materials Science and Technology,* vol. 20, n° 8, p. 1019-1026.

Cai, Dayong, Weihong Zhang, Pulin Nie, Wenchang Liu and Mei Yao. 2007. « Dissolution kinetics of δ phase and its influence on the notch sensitivity of Inconel 718 ». *Materials Characterization,* vol. 58, n° 3, p. 220-225.

Chamanfar, A., L. Sarrat, M. Jahazi, M. Asadi, A. Weck and A. K. Koul. 2013. « Microstructural characteristics of forged and heat treated Inconel-718 disks ». *Materials & Design,* vol. 52, n° 0, p. 791-800.

Corporation, Special Metals. 2007. « Inconel alloy 718 ». < www.specialmetals.com/documents/ >. Consulted on october 31st

Desvallées, Y., M. Bouzidi, F. Bois and N. Beaude. 1994. « Delta pahse in inconel 718 : Mechanical properties and forging requirements ». In *Superalloys 718, 625, 706 and Various Derivatives*. sous la dir. de Loria, E.A., p. 281-91. The Minerals, Metals & Materials Society.

Garcia, C. I., Lis A.K., Loria E.A. and DeArdo A.J. 1992. « Thermomechanical processing and continuous cooling transformation behavior of IN-718 ». In *Superalloys 1992*. sous la dir. de Antolovich, S.D., R.W. Stusrud, R.A. MacKay, D.L. Anton, T. Khan, R.D. Kissinger et D.L. Klarstrom, p. 527-36. Warrendale, PA: The Minerals, Metals & Materials Society.

Geng, L., Young-Sang Na and Nho-Kwang Park. 1997. « Continuous cooling transformation behavior of Alloy 718 ». *Materials Letters,* vol. 30, n° 5–6, p. 401-405.

Grannlund, Gösta H., and Hans Knutsson (Eds). 1995. *Signal processing for computer vision*. Dordrecht; Boston: Kluwer Academic Publishers, 437 p.

Huang, Yi, and Terence G Langdon. 2007. « The evolution of delta-phase in a superplastic Inconel 718 alloy ». *Journal of Materials Science,* vol. 42, n° 2, p. 421-427.

Kuo, C. M., Y. T. Yang, H. Y. Bor, C. N. Wei and C. C. Tai. 2009. « Aging effects on the microstructure and creep behavior of Inconel 718 superalloy ». *Materials Science and Engineering: A,* vol. 510–511, n° 0, p. 289-294.

Li, R. B., M. Yao, W. C. Liu and X. C. He. 2002. « Isolation and determination for δ, γ′ and γ″ phases in Inconel 718 alloy ». *Scripta Materialia,* vol. 46, n° 9, p. 635-638.

Niang, Aliou, Bernard Viguier and Jacques Lacaze. 2010. « Some features of anisothermal solid-state transformations in alloy 718 ». *Materials Characterization,* vol. 61, n° 5, p. 525-534.

Oradei-Basile, A., and J.F. Radavich. 1991. « A current TTT diagram for wrought alloy 718 ». In *Superalloys 718, 625 and Various Derivatives*. sous la dir. de Loria, E.A., p. 325-35. The Minerals, Metals & Materials Society.

Panda, Sushanta Kumar, D. Ravi Kumar, Harish Kumar and A. K. Nath. 2007. « Characterization of tensile properties of tailor welded IF steel sheets and their formability in stretch forming ». *Journal of Materials Processing Technology,* vol. 183, n° 2–3, p. 321-332.

Paulonis, D.F., J.M. Oblak and D.S. Duvall. 1969. « PRECIPITATION IN NICKEL-BASE ALLOY 718 ». *Journal Name: ASM (Amer. Soc. Metals), Trans. Quart., 62: 611-22(Sept. 1969).; Other Information: Orig. Receipt Date: 31-DEC-70*, p. Medium: X.

Rao, G. Appa, Mahendra Kumar, M. Srinivas and D. S. Sarma. 2003. « Effect of standard heat treatment on the microstructure and mechanical properties of hot isostatically pressed superalloy inconel 718 ». *Materials Science and Engineering: A,* vol. 355, n° 1–2, p. 114-125.

Saboori, M., H. Champliaud, J. Gholipour, A. Gakwaya, J. Savoie and P. Wanjara. 2014. « Evaluating the flow stress of aerospace alloys for tube hydroforming process by free expansion testing ». *The International Journal of Advanced Manufacturing Technology,* vol. 72, n° 9-12, p. 1275-1286.

Schneider, C. A., W. S. Rasband and K. W. Eliceiri. 2012. « NIH Image to ImageJ: 25 years of image analysis ». *Nature methods,* vol. 9, n° 7, p. 671-675.

Slama, C., and M. Abdellaoui. 2000. « Structural characterization of the aged Inconel 718 ». *Journal of Alloys and Compounds,* vol. 306, n° 1-2, p. 277-284.

Slama, C., and G. Cizeron. 1997. « Structural behaviour of INC 718 (Etude du comportement structural de l'alliage NC 19 Fe Nb (Inconel 718)) ». *Journal de physique. III,* vol. 7, n° 3, p. 665-688.

Song, Jung Han, and Hoon Huh. 2007. « The effect of strain rate on the material characteristics of nickel-based superalloy inconel 718 ». *Key Engineering Materials,* vol. 340-341 I, p. 283-288.

Sundararaman, M., P. Mukhopadhyay and S. Banerjee. 1988. « Precipitation of the δ-Ni3Nb phase in two nickel base superalloys ». *Metallurgical Transactions A,* vol. 19, n° 3, p. 453-465.

Talonen, Juho, Pertti Nenonen, Gersom Pape and Hannu Hanninen. 2005. « Effect of strain rate on the strain-induced α-martensite transformation and mechanical properties of austenitic stainless steels ». *Metallurgical and Materials Transactions A: Physical Metallurgy and Materials Science,* vol. 36 A, n° Compendex, p. 421-432.

Totten, George E. 2007. *Steel heat treatment : metallurgy and technologies*, 2nd. Boca Raton, FL: Taylor & Francis, 833 p.

Valle, L. C. M., L. S. Araújo, S. B. Gabriel, J. Dille and L. H. Almeida. 2013. « The Effect of δ Phase on the Mechanical Properties of an Inconel 718 Superalloy ». *Journal of Materials Engineering and Performance,* vol. 22, n° 5, p. 1512-1518.

Vanderesse, N., M. Anderson, F. Bridier and P. Bocher. 2016. « Inter- and intragranular delta phase quantitative characterization in Inconel 718 by means of image analysis ». *Journal of Microscopy,* vol. 261, n° 1, p. 79-87.

Anderson, Mélissa. 2010. « Tube hydroforming of aerospace alloys : material characterization methods ». Montréal, Canada, École de technologie supérieure.

Azadian, Saied, Liu-Ying Wei and Richard Warren. 2004. « Delta phase precipitation in Inconel 718 ». *Materials Characterization,* vol. 53, n° 1, p. 7-16.

Barthel, Kai Uwe. 2007. « http://rsbweb.nih.gov/ij/plugins/mean-shift.html ». Consulté le 2013/11/20.

Beaubois, V., J. Huez, S. Coste, O. Brucelle and J. Lacaze. 2004. « Short term precipitation kinetics of delta phase in strain free Inconel* 718 alloy ». *Materials Science and Technology,* vol. 20, n° 8, p. 1019-1026.

Cai, Dayong, Weihong Zhang, Pulin Nie, Wenchang Liu and Mei Yao. 2007. « Dissolution kinetics of δ phase and its influence on the notch sensitivity of Inconel 718 ». *Materials Characterization,* vol. 58, n° 3, p. 220-225.

Chamanfar, A., L. Sarrat, M. Jahazi, M. Asadi, A. Weck and A. K. Koul. 2013. « Microstructural characteristics of forged and heat treated Inconel-718 disks ». *Materials & Design,* vol. 52, n° 0, p. 791-800.

Corporation, Special Metals. 2007. « Inconel alloy 718 ». < www.specialmetals.com/documents/ >. Consulté le october 31st

Desvallées, Y., M. Bouzidi, F. Bois and N. Beaude. 1994. « Delta pahse in inconel 718 : Mechanical properties and forging requirements ». In *Superalloys 718, 625, 706 and Various Derivatives*. sous la dir. de Loria, E.A., p. 281-91. The Minerals, Metals & Materials Society.

Garcia, C. I., Lis A.K., Loria E.A. and DeArdo A.J. 1992. « Thermomechanical processing and continuous cooling transformation behavior of IN-718 ». In *Superalloys 1992*. sous la dir. de Antolovich, S.D., R.W. Stusrud, R.A. MacKay, D.L. Anton, T. Khan, R.D. Kissinger et D.L. Klarstrom, p. 527-36. Warrendale, PA: The Minerals, Metals & Materials Society.

Geng, L., Young-Sang Na and Nho-Kwang Park. 1997. « Continuous cooling transformation behavior of Alloy 718 ». *Materials Letters,* vol. 30, n° 5–6, p. 401-405.

Grannlund, Gösta H., and Hans Knutsson (Eds). 1995. *Signal processing for computer vision*. Dordrecht; Boston: Kluwer Academic Publishers, 437 p.

Huang, Yi, and TerenceG Langdon. 2007. « The evolution of delta-phase in a superplastic Inconel 718 alloy ». *Journal of Materials Science,* vol. 42, n° 2, p. 421-427.

Kuo, C. M., Y. T. Yang, H. Y. Bor, C. N. Wei and C. C. Tai. 2009. « Aging effects on the microstructure and creep behavior of Inconel 718 superalloy ». *Materials Science and Engineering: A,* vol. 510–511, n° 0, p. 289-294.

Li, R. B., M. Yao, W. C. Liu and X. C. He. 2002. « Isolation and determination for δ, γ′ and γ″ phases in Inconel 718 alloy ». *Scripta Materialia,* vol. 46, n° 9, p. 635-638.

Niang, Aliou, Bernard Viguier and Jacques Lacaze. 2010. « Some features of anisothermal solid-state transformations in alloy 718 ». *Materials Characterization,* vol. 61, n° 5, p. 525-534.

Oradei-Basile, A., and J.F. Radavich. 1991. « A current TTT diagram for wrought alloy 718 ». In *Superalloys 718, 625 and Various Derivatives*. sous la dir. de Loria, E.A., p. 325-35. The Minerals, Metals & Materials Society.

Panda, Sushanta Kumar, D. Ravi Kumar, Harish Kumar and A. K. Nath. 2007. « Characterization of tensile properties of tailor welded IF steel sheets and their formability in stretch forming ». *Journal of Materials Processing Technology,* vol. 183, n° 2–3, p. 321-332.

Paulonis, D.F., J.M. Oblak and D.S. Duvall. 1969. « PRECIPITATION IN NICKEL-BASE ALLOY 718 ». *Journal Name: ASM (Amer. Soc. Metals), Trans. Quart., 62: 611-22(Sept. 1969).; Other Information: Orig. Receipt Date: 31-DEC-70*, p. Medium: X.

Rao, G. Appa, Mahendra Kumar, M. Srinivas and D. S. Sarma. 2003. « Effect of standard heat treatment on the microstructure and mechanical properties of hot isostatically pressed superalloy inconel 718 ». *Materials Science and Engineering: A,* vol. 355, n° 1–2, p. 114-125.

Saboori, M., H. Champliaud, J. Gholipour, A. Gakwaya, J. Savoie and P. Wanjara. 2014. « Evaluating the flow stress of aerospace alloys for tube hydroforming process by free expansion testing ». *The International Journal of Advanced Manufacturing Technology,* vol. 72, n° 9-12, p. 1275-1286.

Schneider, C. A., W. S. Rasband and K. W. Eliceiri. 2012. « NIH Image to ImageJ: 25 years of image analysis ». *Nature methods,* vol. 9, n° 7, p. 671-675.

Slama, C., and M. Abdellaoui. 2000. « Structural characterization of the aged Inconel 718 ». *Journal of Alloys and Compounds,* vol. 306, n° 1-2, p. 277-284.

Slama, C., and G. Cizeron. 1997. « Structural behaviour of INC 718 (Etude du comportement structural de l'alliage NC 19 Fe Nb (Inconel 718)) ». *Journal de physique. III,* vol. 7, n° 3, p. 665-688.

Song, Jung Han, and Hoon Huh. 2007. « The effect of strain rate on the material characteristics of nickel-based superalloy inconel 718 ». *Key Engineering Materials,* vol. 340-341 I, p. 283-288.

Sundararaman, M., P. Mukhopadhyay and S. Banerjee. 1988. « Precipitation of the δ-Ni3Nb phase in two nickel base superalloys ». *Metallurgical Transactions A,* vol. 19, n° 3, p. 453-465.

Talonen, Juho, Pertti Nenonen, Gersom Pape and Hannu Hanninen. 2005. « Effect of strain rate on the strain-induced , &rarr -martensite transformation and mechanical properties of austenitic stainless steels ». *Metallurgical and Materials Transactions A: Physical Metallurgy and Materials Science,* vol. 36 A, n° Compendex, p. 421-432.

Totten, George E. 2007. *Steel heat treatment : metallurgy and technologies*, 2nd. Boca Raton, FL: Taylor & Francis, 833 p.

Valle, L. C. M., L. S. Araújo, S. B. Gabriel, J. Dille and L. H. Almeida. 2013. « The Effect of δ Phase on the Mechanical Properties of an Inconel 718 Superalloy ». *Journal of Materials Engineering and Performance,* vol. 22, n° 5, p. 1512-1518.

Vanderesse, N., M. Anderson, F. Bridier and P. Bocher. 2016. « Inter- and intragranular delta phase quantitative characterization in Inconel 718 by means of image analysis ». *Journal of Microscopy,* vol. 261, n° 1, p. 79-87.

CHAPTER 7

THESIS SUMMARY AND CONTRIBUTIONS

This chapter presents a discussion of the results as a whole and aims to link the results detailed in previous chapters with the objectives of the thesis.

7.1 Introduction

The principal research objectives of this project were to study the mechanical and metallurgical behavior of designated aerospace alloys in order to improve their formability for hydroforming application. Aerospace alloys are known for their limited formability whereas hydroforming requires high and uniform elongation.

The first section and main part of the work performed was focused on Stainless Steel 321. The mechanical properties of this alloy subjected to hydroforming-type deformation have been studied as well as its metallurgical response to such type of forming process. The experimental data could become a useful input for Finite Elements analysis of hydroforming process.

The second part was pointed at Inconel 718. The objective for this complex material was focused on the formability improvement of the alloy. Thus, investigating the most appropriate heat treatment allowing formability improvement was the main goal.

7.2 Stainless Steel 321

The work on SS321 was detailed in chapters 2 to 4.The first step of the study of this alloy was to define the appropriate method to improve its formability. A multistep process combining series of deformation and subsequent heat treatment was considered. It consists of interrupted tensile tests up to a limit very close to the onset of the necking followed by a stress relief heat treatment. Through the first paper, it has been proven that this method was

relevant for formability improvement purposes. In fact, by appropriate selection of forming and heat treatment cycles, very high levels of deformation are reached. However, microstructure analysis revealed the formation of Strain Induced Martensite (SIM) after the first of deformation + heat treatment cycle. It was therefore crucial to carry out in depth a metallurgical study and identify the governing mechanisms of SIM development during thermo-mechanical multistep processes. Thus, the metallurgical evolution of SS321 during multistep forming was investigated to understand its impact on the formability enhancement, as detailed in the second paper. Microstructural features such as twins and texture evolution were studied as a function of the selected multistep process. As previously established, it has been confirmed that the mechanical properties were restored after a complete deformation + heat treatment cycle. From a metallurgical point of view, it was demonstrated that the intermediate heat treatment led to partial recrystallization of the material after each step of deformation. The distribution of twins fraction through the multistep process combined with the texture analysis of austenite at each step substantiated the occurrence of partial recrystallization. The restoration of mechanical properties observed through the process was related to recrystallization. The SIM generated during the multistep process is textured and tends to become random with increasing deformation. The SIM evolution was plotted as a function of deformation and it was shown that the Olson-Cohen equation fits very well the experimental data giving an opportunity to predict SIM formation as a function of deformation.

Finally, to validate the formability improvement of SS321 for hydroforming applications, a case study was considered. Instead of tensile testing, a multistep process was performed with hydroforming-type deformation. Thus, interrupted free expansion tests combined with intermediate heat treatment were performed on tubes in the hydroforming press. It was demonstrated that the multistep process is a viable method to improve the hydroformability of SS321. It was shown that, introducing an intermediate stress relief heat treatment not only restores the material to reach higher levels of deformation, but also reduces the level of pressure required to deform the investigated alloy.

The work documented in paper 1 provided responses to the objectives 1 & 3 of this thesis. In fact, by focusing on the mechanical behavior of SS321 under multistep forming process, it has been possible to determine the appropriate combination of deformation and heat treatment for extensive deformation of the alloy. At the same time, an important amount of experimental data have been collected and constitutes a useful database of mechanical properties under various scenarios or deformation + heat treatment cycles. The study behind paper 2 addressed objectives 2 & 4 whereas feeding the experimental database with metallurgical properties (objective 3). In other words, the study of different microstructural phenomena has allowed to better understand the metallurgical response of SS321 under multistep forming as well as the interrelation between the macroscopic mechanical properties and the microscopic data. To finalize the work conducted on SS321, it is necessary to ensure that the formability improvement observed through multistep tensile tests, is transposable to the hydroforming process. That was the purpose of the work behind paper 3. At the same time, the experimental data generated in real hydroforming conditions clearly corresponds to objective 3. Those data (strain distributions, burst pressures...) have been directly incorporated in Finite Elements analyses of multistep hydroforming process (Saboori, 2015).

7.3 Inconel 718

IN718 has been discussed in chapter 5. This material is known to be very complex, with very high strengths (in its usual state) combined with low formability. The multistep method has demonstrated its relevance in the case of performing hydroforming on aerospace alloys such as IN718 if and only if the intermediate heat treatment performed is able to restore the initial microstructure of the material. Thus, it was mandatory to define the most appropriate heat treatment for that purpose. In the fourth paper, several heat treatments leading to δ phase precipitation were investigated. The transformation from the main hardening phase γ'' to the stable phase δ occurred for specific ageing time and/or temperature and was accompanied by a decrease of the hardening properties of IN718. Consequently, maximizing the amount of δ phase would led to minimize the hardening properties while increasing the formability. The results showed that the relation between δ phase precipitation and ductility enhancement is

not as simple as presented in the published mainstream. Several specificities have to be taken into account such as the coexistence of γ'' and δ phases which implies an hardened material regardless of the amount of δ phase. In addition, when there is only δ precipitates, the proportion between intergranular and intragranular precipitates has a critical impact on the formability improvement because they have contradictory effects.

Paper 4 highlighted important elements referring to the effect of δ phase amounts and morphologies on mechanical properties. It mainly addressed objective 5 of the thesis but also objective 3 since the collected data will be helpful for upcoming work on multistep forming process of IN718. Preliminary multistep hydroforming tests using the defined intermediate heat treatment have been performed and the results are documented in Appendix 1.

7.4 Thesis contributions

The thesis contributions are related to the objectives settled at the beginning of this work and can be summarized in the following main points:

1. Extensive study of Stainless steel SS321 in both mechanical and metallurgical points of view. The main part of the thesis was focused on this material and this led to a comprehensive analysis of its mechanical properties and microstructural behavior. This material, until then, was not the subject of many researches and remained rather underestimated. Through the work performed here, useful data have been published which showed the versatility of this material.
2. Knowledge improvement on material behavior under multistep forming method, specifically the combination of deformation and heat treatment. From the metallurgical point of view, the study of various properties such as twins evaluation, texture analysis, phases distribution has allowed the in depth study of interrelations between heat treatments and forming. This enabled to better understand important metallurgical concepts in line with the required properties and contributed to the

advancement of knowledge in the case of metallurgical response to multistep forming processes.

3. Important experimental data acquisition in the context of hydroforming process of two main aerospace alloys which will be used as a database to feed Finite Elements Analyses. In fact, instead of using theoretical mechanical data such as hardening coefficient or yield strength in the various configurations (pre-forming, after HT...), the real properties have been measured and documented.

Saboori, Mehdi. 2015. « Material modeling for multistage tube hydroforming process simulation ». D.Eng. Ann Arbor, Ecole de Technologie Superieure (Canada), 191 p. In ProQuest Dissertations & Theses Global.

CONCLUSIONS

The purpose of this PhD was to increase the formability of some aerospace alloys for tube hydroforming applications. Hydroforming is a very interesting manufacturing process widely used in various industries such as automotive because of its multiple advantages. But, it remains under represented in the aerospace industry mainly because of the limited formability of the aeronautical alloys. Thus, it is crucial to improve the formability of these alloys to allow the exploitation of this technique in the aerospace sector. The methodology suggested was a multistep forming procedure which combines a deformation step followed by an appropriate heat treatment in order to restore the material and continue forming without any failure. The investigated aerospace materials were the austenitic stainless steel SS321 and the Nickel-Iron based superalloy Inconel 718.

The first step was to validate the methodology of multistep forming process. This has been conducted on SS321. The multistep forming process steps were simulated through interrupted uniaxial tensile tests followed by a softening heat treatment. The limit strain decided for interruption was chosen close to the onset of the necking in order to maximize the deformation at each step. It has been demonstrated that the applied stress relief heat treatment led to a major restoration of the material which confirmed the relevance of the multistep forming process to improve material formability. In fact, with a judicious combination of deformation and appropriate heat treatment, very high levels of deformation was reached by this approach. A preliminary study of the SS321 metallurgical response to multistep forming had brought out interesting research paths. In fact, SS321 is subjected to Strain Induced Martensite (SIM) and this has to be taken into account during the process because it may affect the material behavior. Thus, the governing mechanisms around the formation and the stabilization of the SIM under multistep forming process have been investigated in more details to fully document the mechanical as well as metallurgical behavior of this material.

The next step of the work was mainly focused on the metallurgical properties evolution of SS321 during multistep forming process. The restoration of mechanical properties after intermediate heat treatments has been confirmed. The metallurgical mechanisms behind the formability improvement of SS321 have been examined. The twins fraction examination indicated the occurrence of partial recrystallization at each step, even if some grain growth was observed. The austenitic phase texture analyses confirmed the presence of incomplete recrystallization. In fact, the intermediate heat treatment tends to randomize the texture by decreasing the MUD before and after heat treatment. The texture analysis was also performed on the SIM and it was concluded that the generated martensite is textured. Finally, the SIM evolution during multistep forming process was fitted by Olson-Cohen equation which ensured that its evolution can be predicted with the identified appropriate α and β parameters. Now that it has been demonstrated that the mechanical properties of SS321 can be fully restored during multistep forming process and the metallurgical response to the process is deeply understood, the final point was to validate the process in real hydroforming conditions.

The last study aimed at SS321 was a case study of the multistep hydroforming process. Interrupted free expansion tests were performed combined with the stress relief heat treatment on SS321 seamless tubes. The results were very convincing. It was shown that by deforming in 2 steps with an intermediate heat treatment instead of 1 step, the radial tube expansion was increased by more than 25%. In addition, the required pressure to deform the tube was also reduced by almost 20% due to the improved ductility of the material after the first cycle. These experiments completed the work on the SS321.

The superalloy IN718, more complex than the SS321, was subjected to a different work scope. The objective of the IN718 study was to identify the most appropriate intermediate heat treatment to allow formability improvement of this alloy while maintaining interesting mechanical properties. A complete experimental design was put in place to ensure that all heat treatment possibilities leading to potential ductility improvement were captured through the implemented experiments. Microstructural analysis led to the identification of two types

of δ precipitates as well as their quantification. In parallel, the associated mechanical properties were measured to investigate the relationship between δ phase precipitation and mechanical response of the material. This study clarified some preconceived ideas around IN718 formability. Notably, to improve its formability, it is not appropriate to maximize δ phase; on the contrary, a balance between intergranular and intragranular δ precipitates should be privileged. The most interesting heat treatment for multistep hydroforming purpose has been identified as 975°C for 2h followed by fast quenching.

RECOMMENDATIONS

The following research directions have been identified as interesting paths for future investigation in the continuity of this PhD :

- The microstructural analysis of SS321 should be continued to understand in-depth the governing mechanisms of SIM formation and evolution when subjected to multistep forming process. The preliminary work on the Olson-Cohen parameters (α and β) evolution as a function of the applied strain showed surprising results. The α parameter significantly increased from step 1 to step 2 indicating that the shear bands are generated more easily in the second step. However, the β parameter decreased from step 1 to step 2 implying a reduction of shear bands intersections leading to α'-martensite embryo. Several hypotheses have been put forward and need to be experimentally validated through microscale analysis of deformed samples and extensive EBSD studies of local grains misorientation during deformation.
- The multistep hydroforming process of SS321 tubes has been performed as a case study to validate the method with a single interruption. Further researches should be conducted around multistep hydroforming process of SS321 tubes including several steps to validate how far we can go with this method. The objective would be to reach a maximum expansion with a minimum thickness reduction. In parallel, the metallurgical properties of specimens deformed in biaxial direction would be confirmed. Finally, an extended correlation between levels of deformation reached and the expected microstructural behavior could be established for Finite Element Analysis purposes.
- The optimized heat treatment for formability improvement of IN718 has been identified in this PhD work. The metallurgical investigation should be pursued to study the impact of this heat treatment on IN718 global microstructure (progressive dissolution of precipitates and kinetics of phases formation, grain size effect, orientation distribution, texture evolution, etc.).

- Multistep hydroforming process on IN718 tubes using the appropriate HT has been started and should be completed. The experimental procedure for FX tests has been optimized through SS321 campaign and has to be adapted to IN718 tubes.
- The multistep forming process has been set up experimentally. The next step would be to simulate a real hydroformed part, i.e. Round to V shape or Round to square shape using material model developed by CRIAQ 4.6 project team members. The distinctive feature here will be the multistep character with introduction of the intermediate heat treatment. This will be translated by new material properties (i.e. work hardening coefficients, YS, etc.) at each step.

APPENDIX I

MULTISTEP HYDROFORMING OF INCONEL 718 TUBES

1) Tube details

The FX tests were performed on tubes with the following characteristic following the end feeding method, i.e. some material was pushed into the deformation zone from the clamped areas. The objective was to maximize the formability (bulge height) by combining internal pressure with axial displacement.

- Tube thickness = 0.9 mm (0.035")
- End Feeding tube length = 254.0 mm (10")

2) Heat treatments

Before deformation, an initial heat treatment (detailed below) had been conducted on the tubes to standardize the metallurgical initial state of the material in its As-received condition. Then, the intermediate heat treatment which has been demonstrated as the best compromise for formability improvement of IN718 was conducted between the deformation steps.

- As-received starting condition (AR) = 1005°C (±5°C) / 2h + Forced cooling Argon – P = 2bars
- Intermediate HT (HT) = 975°C (±3°C) / 2h + Water Quenching

3) End feeding method

Several tests had been conducted to identified the best parameters in the End feeding condition to ensure that an uniform bulge is reached, the seal at both ends is maintained along the process and no premature burst occurred.

- Pressure rate = 1.25 MPa/s
- EF rate = 0.25 mm/s
- Sealing force = 37 kN
- Maximum pressure (test with EF) = 28.6 MPa
- Aramis image rate = 6 images / s

4) Experimental design

As detailed before, the first step consisted on a single FX up to burst in order to measure the burst pressure and therefore, calculate the appropriate pause pressure.

The second test series were a multistep FX test with 1 intermediate HT. The first step was conducted up to 80% of the Burst pressure (corresponding to the pause pressure). Then, the tubes underwent the intermediate HT before being deformed up the burst.

Finally, the third stage corresponded to a multistep FX with 2 intermediate HT before burst.

For each stage, a minimum of 2 tubes were tested and at each intermediate step , 1 tube was kept for further analyses.

IN 718		CONDITION	STEP 1	STEP 2	STEP 3
Stage 1	A→B	AR	Burst		
Stage 2	B'→C	AR+FX+HT	80% P^{A}_{Burst}	Burst	
Stage 3	C'→D	AR+FX+HT+FX+HT	80% P^{A}_{Burst}	80% P^{B}_{Burst}	Burst

Table-A 1: Multistep FX tests on IN718 methodology

5) Procedure

- Tubes from the beginning in the AR heat treatment condition
- 1 tube is burst at each step
- The stop pressure is calculated based on the burst pressure of the previous step (80% P_{Burst})

6) Results

a) Single FX

In order to determine the appropriate pause pressure, FX tests were conducted up to the burst point. The maximum bulge height before burst was measured and plotted as a function of the internal pressure in Figure A-1.

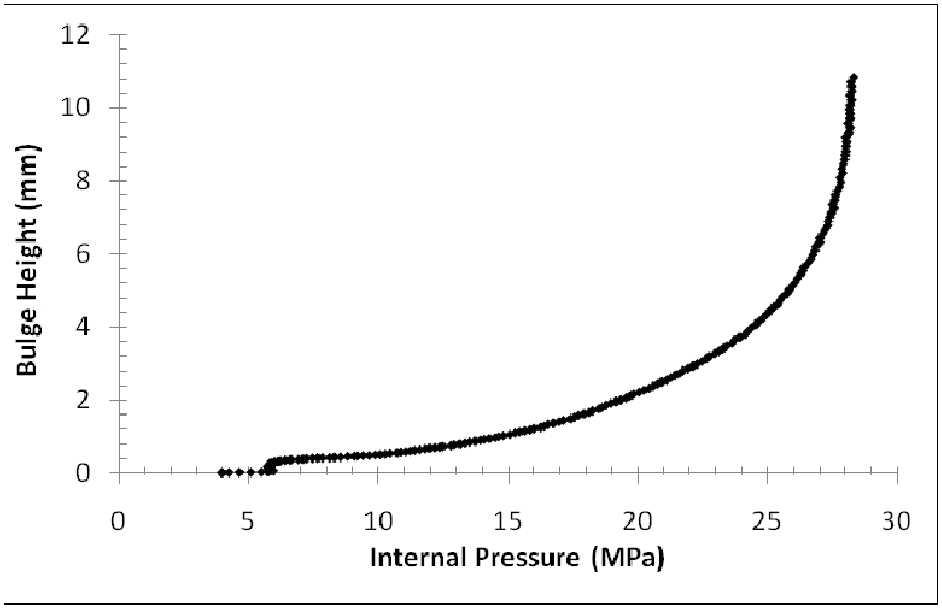

Figure-A 1: Bulge height versus internal pressure curve of a typical single FX test up to the burst point

From Figure A-1, it can be seen that the bulge height (expansion) is increasing with the internal pressure starting at the early stage of the process. This comes from the end feeding method used. The axial displacement introduced at the beginning at the same time as the pressure induced an increase of the bulge height even a at very low pressure. The maximum expansion reached was about 10.5 mm for a burst pressure of 28.5 MPa.

b) Interrupted FX tests - 1 step

The bulge height results for an interrupted (1 time) FX test are displayed in Figure A-2. The black curve (lower curve) represents the bulge height as a function of the internal pressure for the first forming step. This step has been stopped at the pause pressure. Then, the tube was heat treated before a second forming step up to the burst (upper grey curve).

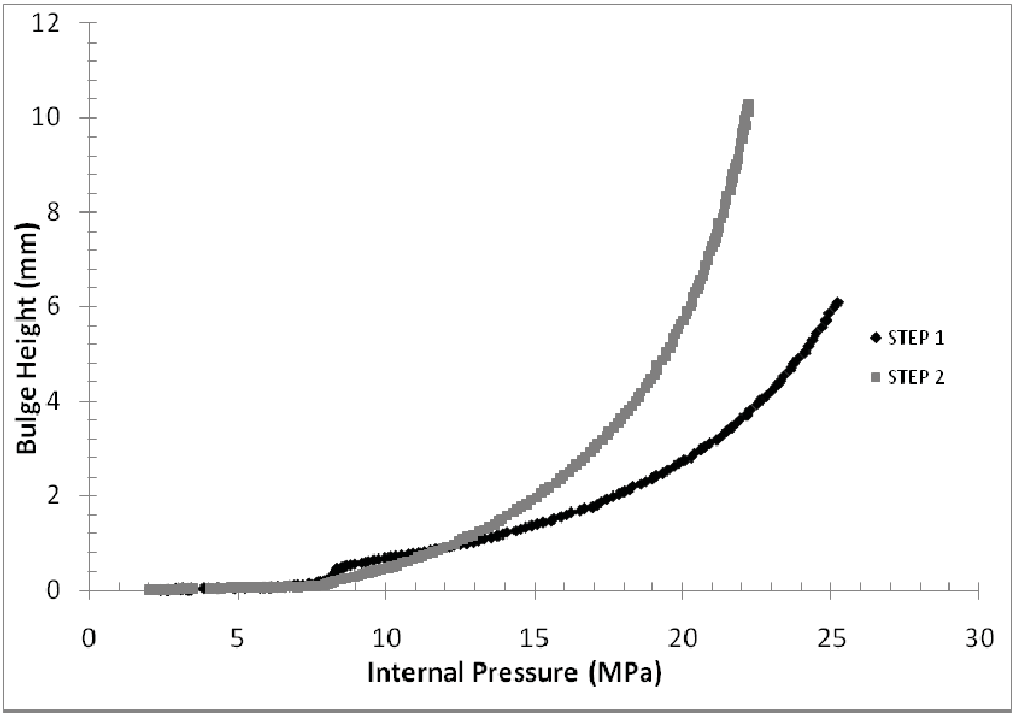

Figure-A 2: Bulge height versus internal pressure curve of interrupted FX tests (2 steps)

The bulge height reached at the pause pressure was about 6 mm before the SR heat treatment was applied. In step 2, the maximum bulge height at burst was about 10.5 mm. This corresponds to the expansion obtained after a single FX test. As observed for SS321, the intermediate heat treatment restores the formability of the alloy. In addition, the bulge height in step 2 supplements the bulge height obtained in Step 1, for a cumulative maximum expansion around 16.5 mm. This represents a gain of almost 60%. By comparing the two curves (before and after SR heat treatment), it has been observed that the required pressure to deform the part up to a specific level is reduced. In fact, at a specific internal pressure (20MPa for instance), the bulge height is doubled in step 2 relative to step 1. Not only that the heat treatment restore the material formability, but also, the tube thickness decreased which made easier the 2nd step deformation.

c) Interrupted FX tests - 2 steps

The bulge height results for an interrupted (2 times) FX test are displayed in Figure A-3. The same approach as previous interrupted tests had been followed. The black curve (lower curve) represents the bulge height as a function of the internal pressure for the first forming step, stopped at the pause pressure. Then, the tube was heat treated before a second forming step u (grey medium curve). The tubes were heat treated for a second time before final test up to burst (light gray curve).

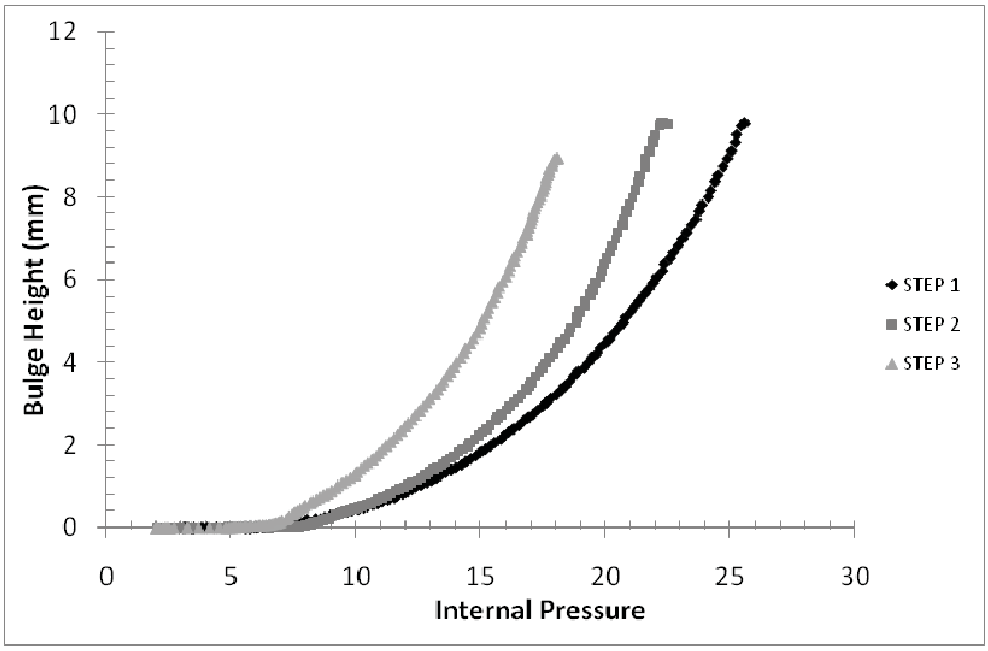

Figure-A 3: Bulge height versus internal pressure curve of interrupted FX tests (3 steps)

The results obtained were aligned where the expectations. The interrupted forming steps allowed a cumulative maximum expansion of 19.6 mm. At the last step of forming, the expansion at burst slightly decreased to 8.5 mm, demonstrating a beginning of localization (thinning of the material) in the tube. After 3 forming steps, the maximum expansion reached for IN718 is about 28.1 mm. The internal pressure continue to decrease with the increase of forming step to attain 18MPa burst pressure after 3 steps compared to 28,5MPa burst pressure during a single FX.

BIBLIOGRAPHY

Ahmetoglu, M., and T. Altan. 2000. « Tube hydroforming: state-of-the-art and future trends ». *Journal of Materials Processing Technology,* vol. 98, n° 1, p. 25-33.

Allen, Dell K. 1969. *Metallurgy theory and practice*. Chicago: American Technical Society, 663 p.

Anderson, M. 2013. « Improving the formability of stainless steel 321 through multistep deformation for hydroforming applications ». *Transactions of the Canadian Society for Mechanical Engineering,* vol. 37, n° 1, p. 39.

Anderson, M., J. Gholipour, P. Bocher, F. Bridier, J. Savoie and P. Wanjara. 2010. « Formability extension of aerospace alloys for tube hydroforming applications ». *International Journal of Material Forming,* vol. 3, n° SUPPL 1, p. 303-306.

Anderson, Mélissa. 2010. « Tube hydroforming of aerospace alloys : material characterization methods ». Montréal, Canada, École de technologie supérieure.

Angel, T. 1954a. « Formation of martensite in austenitic stainless steels ». *Iron and Steel Institute -- Journal,* vol. 177, n° Part 1, p. 165-174.

Angel, T. 1954b. « Formation of martensite in austenitic stainless steels ». *The journal of the Iron and Steel Institute* vol. 177, n° Part 1, p. 165-174.

Azadian, Saied, Liu-Ying Wei and Richard Warren. 2004. « Delta phase precipitation in Inconel 718 ». *Materials Characterization,* vol. 53, n° 1, p. 7-16.

Barbier, D., N. Gey, S. Allain, N. Bozzolo and M. Humbert. 2009. « Analysis of the tensile behavior of a TWIP steel based on the texture and microstructure evolutions ». *Materials Science and Engineering: A,* vol. 500, n° 1–2, p. 196-206.

Barthel, Kai Uwe. 2007. « http://rsbweb.nih.gov/ij/plugins/mean-shift.html ». Consulté le 2013/11/20.

Beaubois, V., J. Huez, S. Coste, O. Brucelle and J. Lacaze. 2004. « Short term precipitation kinetics of delta phase in strain free Inconel* 718 alloy ». *Materials Science and Technology,* vol. 20, n° 8, p. 1019-1026.

Beese, A. M., and D. Mohr. 2009. « Experimental Quantification of Phase Transformation in Austenitic Stainless Steel ». In *SEM 2009 Annual Conference & Exposition on Experimental & Applied Mechanics*. (Albuquerque New Mexico USA, June 1-4, 2009). Society for Experimental Mechanics.

Boyer, Howard E. 1990. *Atlas of stress-strain curves*. Metals Park, Ohio: ASM International, xx, 630 p.

Bridier, F., J-C. Stinville, N. Vanderesse, P. Villechaise and P. Bocher. 2014. « Microscopic strain and crystal rotation measurement within metallurgical grains ». *Key Engineering Materials,* vol. 592-593, p. 493-496.

Brooks, Charlie R. 1982. *Heat treatment, structure, and properties of nonferrous alloys*. Metals Park, Ohio: American Society for Metals, x, 420 p.

Byrne, J. Gerald. 1965. *Recovery, recrystallization, and grain growth*. Coll. « Macmillan series in materials science ». New York, : Macmillan, ix, 179 p.

Cahoon, J. R., Qiangyong Li and N. L. Richards. 2009. « Microstructural and processing factors influencing the formation of annealing twins ». *Materials Science and Engineering: A,* vol. 526, n^{o} 1–2, p. 56-61.

Cai, Dayong, Weihong Zhang, Pulin Nie, Wenchang Liu and Mei Yao. 2007. « Dissolution kinetics of δ phase and its influence on the notch sensitivity of Inconel 718 ». *Materials Characterization,* vol. 58, n^{o} 3, p. 220-225.

Chamanfar, A., L. Sarrat, M. Jahazi, M. Asadi, A. Weck and A. K. Koul. 2013. « Microstructural characteristics of forged and heat treated Inconel-718 disks ». *Materials & Design,* vol. 52, n^{o} 0, p. 791-800.

Chandler, Harry. 1995. *Heat treater's guide : practices and procedures for irons and steels*, 2nd. Materials Park, OH: ASM International, vii, 903 p.

Chen, K. K., R. J. Soldaat and R.M. Moses. 2004. *Free expansion bulge testing of tubes for automotive hydroform applications*. SAE technical paper No. 2004-01-0832. Warrendale, Pennsylvania.

Choi, Ho, Muammer Koc and Jun Ni. 2008. « A Study on Warm Hydroforming of Al and Mg Sheet Materials: Mechanism and Proper Temperature Conditions ». *Journal of Manufacturing Science and Engineering,* vol. 130, n^{o} 4, p. 041007-14.

Chunchun, Xu, Hu Gang and Wing-Yan Ng. 2004. « Relationship between the martensite phase transition and pitting susceptibility of AISI-321 stainless steel in acidic solutions of NaCl ». *Materials Science,* vol. 40, n^{o} 2, p. 252-259.

Corporation, Special Metals. 2007. « Inconel alloy 718 ». < www.specialmetals.com/documents/ >. Consulté le october 31st

Dash, S., and N. Brown. 1963. « An investigation of the origin and growth of annealing twins ». *Acta Metallurgica,* vol. 11, n^{o} 9, p. 1067-1075.

Datsko, J. 1966a. *Material Properties and Manufacturing Processes*. New York, USA: Wiley.

Datsko, Joseph. 1966b. *Material properties and manufacturing processes*. New York: Wiley, 543 p.

DeAntonio, D. A. , D. Duhl, T. Howson and M.F. Rothman. 1991. « Heat Treating of Superalloys ». In *Heat treating*, sous la dir. de International, ASM. Vol. 4, p. 793-814. Coll. « ASM handbook »: ASM International. < http://products.asminternational.org/hbk/index.jsp >. Consulté le 2013/06/21.

Desvallées, Y., M. Bouzidi, F. Bois and N. Beaude. 1994. « Delta pahse in inconel 718 : Mechanical properties and forging requirements ». In *Superalloys 718, 625, 706 and Various Derivatives*. sous la dir. de Loria, E.A., p. 281-91. The Minerals, Metals & Materials Society.

Doherty, R. D., D. A. Hughes, F. J. Humphreys, J. J. Jonas, D. Juul Jensen, M. E. Kassner, W. E. King, T. R. McNelley, H. J. McQueen and A. D. Rollett. 1997. « Current issues in recrystallization: a review ». *Materials Science and Engineering A,* vol. 238, n^{o} 2, p. 219-274.

Dohmann, F., and Ch Hartl. 2004. « Hydroforming-applications of coherent FE-simulations to the development of products and processes ». *Journal of Materials Processing Technology,* vol. 150, n^{o} 1-2, p. 18-24.

Durand-Charre, Madeleine. 1997. *The microstructure of superalloys*. Boca raton, Flor.: CRC Press, xiv, 124 p.

Eichelmann, G. H., and F. C. Hull. 1953. « The effect of composition on the temperature of spontaneous transformation of austenite to martensite in 18-8-type stainless steels ». *Transactions ASM,* vol. 45, p. 77-104.

Fischer. 2006. *Operator's manual for feritscope MP30E-S.*

Fullman, R. L., and J. C. Fisher. 1951. « Formation of Annealing Twins During Grain Growth ». *Journal of Applied Physics,* vol. 22, n^{o} 11, p. 1350-1355.

Garcia, C. I., Lis A.K., Loria E.A. and DeArdo A.J. 1992. « Thermomechanical processing and continuous cooling transformation behavior of IN-718 ». In *Superalloys 1992*. sous la dir. de Antolovich, S.D., R.W. Stusrud, R.A. MacKay, D.L. Anton, T. Khan, R.D. Kissinger et D.L. Klarstrom, p. 527-36. Warrendale, PA: The Minerals, Metals & Materials Society.

Geng, L., Young-Sang Na and Nho-Kwang Park. 1997. « Continuous cooling transformation behavior of Alloy 718 ». *Materials Letters,* vol. 30, n° 5–6, p. 401-405.

Gey, Nathalie, B. Petit and M. Humbert. 2005. « Electron backscattered diffraction study of / martensitic variants induced by plastic deformation in 304 stainless steel ». *Metallurgical and Materials Transactions A: Physical Metallurgy and Materials Science,* vol. 36, p. 3291-3299.

Gholipour, Javad, Michael J. Worswick and D. Oliviera. 2004. *Application of damage models in bending and hydroforming of aluminum alloy tube*. SAE technical paper No. 2004-01-835. Warrendale, Pennsylvania.

Ghosh, S., P. Mallick and P. Chattopadhyay. 2011. « Effect of reversion of strain induced martensite on microstructure and mechanical properties in an austenitic stainless steel ». *Journal of Materials Science,* vol. 46, n° 10, p. 3480-3487.

Gleiter, H. 1969. « The formation of annealing twins ». *Acta Metallurgica,* vol. 17, n° 12, p. 1421-1428.

Golovashchenko, Sergey, and Al Krause. 2005. « Improvement of formability of 6xxx aluminum alloys using incremental forming technology ». *Journal of Materials Engineering and Performance,* vol. 14, n° 4, p. 503-507.

Gottstein, G. 1984. « Annealing texture development by multiple twinning in f.c.c. crystals ». *Acta Metallurgica,* vol. 32, n° 7, p. 1117-1138.

Grannlund, Gösta H., and Hans Knutsson (Eds). 1995. *Signal processing for computer vision*. Dordrecht; Boston: Kluwer Academic Publishers, 437 p.

Groche, P., R. Huber, J. Dörr and D. Schmoeckel. 2002. « Hydromechanical Deep-Drawing of Aluminium-Alloys at Elevated Temperatures ». *CIRP Annals - Manufacturing Technology,* vol. 51, n° 1, p. 215-218.

Grosse, M., D. Kalkhof, M. Niffenegger and L. Keller. 2006. « Influencing parameters on martensite transformation during low cycle fatigue for steel AISI 321 ». *Materials Science and Engineering: A,* vol. 437, n° 1, p. 109-113.

Hartl, Ch. 2005. « Research and advances in fundamentals and industrial applications of hydroforming ». *Journal of Materials Processing Technology,* vol. 167, n° 2-3, p. 383-392.

Hecker, S., M. Stout, K. Staudhammer and J. Smith. 1982. « Effects of Strain State and Strain Rate on Deformation-Induced Transformation in 304 Stainless Steel: Part I. Magnetic Measurements and Mechanical Behavior ». *Metallurgical and Materials Transactions A,* vol. 13, n° 4, p. 619-626.

Hilkhuijsen, P., H. J. M. Geijselaers and T. C. Bor. 2012. « The influence of austenite texture on the martensitic transformation of an austenitic stainless steel ». *Journal of Alloys and Compounds*, n° 0.

Huang, Yi, and TerenceG Langdon. 2007. « The evolution of delta-phase in a superplastic Inconel 718 alloy ». *Journal of Materials Science,* vol. 42, n° 2, p. 421-427.

Humphreys, F. J. 2004. « Nucleation in recrystallization ». In *Proceedings of the Second Joint International Conferences on Recrystallization and Grain Growth, ReX and GG2, SF2M, August 30, 2004 - September 3, 2004*. (Annecy, France), I Vol. 467-470, p. 107-116. Coll. « Materials Science Forum »: Trans Tech Publications Ltd.

Humphreys, F. J., and M. Hatherly. 2004. *Recrystallization and Related Annealing Phenomena* 2nd ed. Oxford: Elsevier, 628 p.

Jiménez, J. A., and G. Frommeyer. 2010. « Analysis of the microstructure evolution during tensile testing at room temperature of high-manganese austenitic steel ». *Materials Characterization,* vol. 61, n° 2, p. 221-226.

Kaieda, Yoshinari, and Atsushi Oguchi. 1985. « Strain-induced transformation and plastic deformation behaviour of a 17Cr-7Ni-1Al steel at high hydrostatic pressure ». *Journal of Materials Science,* vol. 20, n° 5, p. 1847-1858.

Kleiner, M., M. Geiger and A. Klaus. 2003. « Manufacturing of Lightweight Components by Metal Forming ». *CIRP Annals - Manufacturing Technology,* vol. 52, n° 2, p. 521-542.

Koç, Muammer. 2008. *Hydroforming for advanced manufacturing*. Coll. « Woodhead publishing in materials ». Cambridge Boca Raton: Woodhead publishing ; CRC Press, xvi, 396 p.

Koç, Muammer, and Taylan Altan. 2001. « An overall review of the tube hydroforming (THF) technology ». *Journal of Materials Processing Technology,* vol. 108, n° 3, p. 384-393.

Koç, Muammer, Yingyot Aue-u-lan and Taylan Altan. 2001. « On the characteristics of tubular materials for hydroforming - experimentation and analysis ». *International Journal of Machine Tools and Manufacture,* vol. 41, n° 5, p. 761-772.

Krauss, George. 1990. *Steels : heat treatment and processing principles*. Materials Park, Ohio: ASM International, xvi, 497 p.

Kumar, B., B. Mahato, N. Bandyopadhyay and D. Bhattacharya. 2005. « Influence of strain-induced phase transformation on the surface crystallographic texture in cold-rolled-

and-aged austenitic stainless steel ». *Metallurgical and Materials Transactions A,* vol. 36, n° 11, p. 3165-3174.

Kumar, B. Ravi, A. K. Singh, B. Mahato, P. K. De, N. R. Bandyopadhyay and D. K. Bhattacharya. 2006. « Deformation-induced transformation textures in metastable austenitic stainless steel ». *Materials Science and Engineering: A,* vol. 429, n° 1–2, p. 205-211.

Kuo, C. M., Y. T. Yang, H. Y. Bor, C. N. Wei and C. C. Tai. 2009. « Aging effects on the microstructure and creep behavior of Inconel 718 superalloy ». *Materials Science and Engineering: A,* vol. 510–511, n° 0, p. 289-294.

Kurc-Lisiecka, A., W. Ozgowicz and W. Ratuszek. 2012. « Development of deformation texture of austenitic Cr-Ni steel ». *Machines, Technologies, Materials virtual journal*, n° 9, p. 47-50.

Kurdjumow, G., and G. Sachs. 1930. « Über den Mechanismus der Stahlhärtung ». *Zeitschrift für Physik,* vol. 64, n° 5-6, p. 325-343.

Kuwabara, T., M. Ishiki, M. Kuroda and S. Takahashi. 2003. « Yield locus and work hardening behavior of a thin-walled steel tube subjected to combined tension-internal pressure ». *J. Phys. IV France,* vol. 105, p. 347-354.

Lang, L. H., Z. R. Wang, D. C. Kang, S. J. Yuan, S. H. Zhang, J. Danckert and K. B. Nielsen. 2004. « Hydroforming highlights: sheet hydroforming and tube hydroforming ». *Journal of Materials Processing Technology,* vol. 151, n° Copyright 2004, IEE, p. 165-77.

Leban, Mirjam Bajt, and Robert Tisu. 2013. « The effect of TiN inclusions and deformation-induced martensite on the corrosion properties of AISI 321 stainless steel ». *Engineering Failure Analysis,* vol. 33, n° 0, p. 430-438.

Lecroisey, F., and A. Pineau. 1972. « Martensitic transformations induced by plastic deformation in the Fe-Ni-Cr-C system ». *Metallurgical and Materials Transactions B,* vol. 3, n° 2, p. 391-400.

Levy, B. S., C. J. Van Tyne and J. M. Stringfield. 2004. « Characterizing steel tube for hydroforming applications ». *Journal of Materials Processing Technology,* vol. 150, n° 3, p. 280-289.

Li, R. B., M. Yao, W. C. Liu and X. C. He. 2002. « Isolation and determination for δ, γ′ and γ″ phases in Inconel 718 alloy ». *Scripta Materialia,* vol. 46, n° 9, p. 635-638.

Lianfa, Yang, and Guo Cheng. 2008. « Determination of stress-strain relationship of tubular material with hydraulic bulge test ». *Thin-Walled Structures,* vol. 46, n° 2, p. 147-154.

Lula, R. A., J. Gordon Parr and Albert Hanson. 1989. *Stainless steel*, rev. Metals Park, Ohio: American Society for Metals, x, 173 p.

Mangonon Jr, P. L., and G. Thomas. 1970. « Structure and properties of thermal-mechanically treated 304 stainless steel ». vol. 1, p. 1587-1594.

Marshall, P. 1984. *Austenitic stainless steels : microstructure and mechanical properties*. London: Elsevier Applied Science Publishers, xi, 431 p.

Meetham, G. W. 1981. *The development of gas turbine materials*. New York, N.Y.: Halsted Press, J. Wiley and Sons., xi, 306 p.

Meyers, Marc A., and Lawrence E. Murr. 1978. « A model for the formation of annealing twins in F.C.C. metals and alloys ». *Acta Metallurgica,* vol. 26, n° 6, p. 951-962.

Mons, Claude. 1996. « Traitement thermiques des superalliages ». vol. Traitement des métaux, n° M1165.

Neugebauer, R., T. Altan, M. Geiger, M. Kleiner and A. Sterzing. 2006. « Sheet metal forming at elevated temperatures ». *CIRP Annals - Manufacturing Technology,* vol. 55, n° 2, p. 793-816.

Niang, Aliou, Bernard Viguier and Jacques Lacaze. 2010. « Some features of anisothermal solid-state transformations in alloy 718 ». *Materials Characterization,* vol. 61, n° 5, p. 525-534.

O'Donnell, M., D. Banabic, A. Leacock, D. Brown and R. McMurray. 2008a. « The Effect of Pre-Strain and Inter-Stage Annealing on the Formability of a 2024 Aluminium Alloy ». *International Journal of Material Forming,* vol. 1, n° 0, p. 253-256.

O'Donnell, M., A. Leacock, D. Banabic, D. Brown and R. McMurray. 2008b. « The Effect of Pre-Strain and Solution Heat Treatment on the Formability of a 2024 Aluminium Alloy ». *International Journal of Material Forming,* vol. 1, n° 0, p. 257-260.

Olson, G. B., and Morris Cohen. 1975. « Kinetics of strain-induced martensitic nucleation ». *Metallurgical Transactions A,* vol. 6, n° 4, p. 791-795.

Olson, G., and Morris Cohen. 1976. « A general mechanism of martensitic nucleation: Part I. General concepts and the FCC → HCP transformation ». *Metallurgical and Materials Transactions A,* vol. 7, n° 12, p. 1897-1904.

Oradei-Basile, A., and J.F. Radavich. 1991. « A current TTT diagram for wrought alloy 718 ». In *Superalloys 718, 625 and Various Derivatives*. sous la dir. de Loria, E.A., p. 325-35. The Minerals, Metals & Materials Society.

Panda, Sushanta Kumar, D. Ravi Kumar, Harish Kumar and A. K. Nath. 2007. « Characterization of tensile properties of tailor welded IF steel sheets and their formability in stretch forming ». *Journal of Materials Processing Technology,* vol. 183, n° 2–3, p. 321-332.

Paulonis, D.F., J.M. Oblak and D.S. Duvall. 1969. « PRECIPITATION IN NICKEL-BASE ALLOY 718 ». *Journal Name: ASM (Amer. Soc. Metals), Trans. Quart., 62: 611-22(Sept. 1969).; Other Information: Orig. Receipt Date: 31-DEC-70*, p. Medium: X.

Peterson, S., M. Mataya and D. Matlock. 1997. « The formability of austenitic stainless steels ». *JOM Journal of the Minerals, Metals and Materials Society,* vol. 49, n° 9, p. 54-58.

Ramirez, Jorge Armando Cortes, Toshio Tsuta, Yoshito Mitani and Kozo Osakada. 1992. « Flow Stress and Phase Transformation Analyses in the Austenitic Stainless Steel under Cold Working : Part 1, Phase Transformation Characteristics and Constitutive Formulation by Energetic Criterion ». *JSME international journal. Ser. 1, Solid mechanics, strength of materials,* vol. 35, n° 2, p. 201-209.

Rao, G. Appa, Mahendra Kumar, M. Srinivas and D. S. Sarma. 2003. « Effect of standard heat treatment on the microstructure and mechanical properties of hot isostatically pressed superalloy inconel 718 ». *Materials Science and Engineering: A,* vol. 355, n° 1–2, p. 114-125.

Ravi Kumar, B., S. K. Das, B. Mahato and R. N. Ghosh. 2010. « Role of strain-induced martensite on microstructural evolution during annealing of metastable austenitic stainless steel ». *Journal of Materials Science,* vol. 45, p. 911-918.

Ray, R. K., J. J. Jonas, Butr, oacute, Guill n, eacute, M. P. n and J. Savoie. 1994. « Transformation Textures in Steels ». *ISIJ International,* vol. 34, n° 12, p. 927-942.

Reed, Roger C. 2008. *The superalloys : fundamentals and applications*. Cambridge ; New York: Cambridge University Press, xv, 372 p.

Rosen, A., R. Jago and T. Kjer. 1972. « Tensile properties of metastable stainless steels ». *Journal of Materials Science,* vol. 7, n° 8, p. 870-876.

Saboori, M., H. Champliaud, J. Gholipour, A. Gakwaya, J. Savoie and P. Wanjara. 2010. « Analytical Evaluation and Finite Element Simulation of material Characteristics in Tube Hydroforming of Aerospace Alloys ». In.

Saboori, M., H. Champliaud, J. Gholipour, A. Gakwaya, J. Savoie and P. Wanjara. 2014. « Evaluating the flow stress of aerospace alloys for tube hydroforming process by free expansion testing ». *The International Journal of Advanced Manufacturing Technology,* vol. 72, n° 9-12, p. 1275-1286.

Saboori, Mehdi. 2015. « Material modeling for multistage tube hydroforming process simulation ». D.Eng. Ann Arbor, Ecole de Technologie Superieure (Canada), 191 p. In ProQuest Dissertations & Theses Global.

Saleh, Ahmed A., Elena V. Pereloma and Azdiar A. Gazder. 2011. « Texture evolution of cold rolled and annealed Fe–24Mn–3Al–2Si–1Ni–0.06C TWIP steel ». *Materials Science and Engineering: A,* vol. 528, n° 13–14, p. 4537-4549.

Schneider, C. A., W. S. Rasband and K. W. Eliceiri. 2012. « NIH Image to ImageJ: 25 years of image analysis ». *Nature methods,* vol. 9, n° 7, p. 671-675.

Sibum, H. 2003. « Titanium and Titanium Alloys—From Raw Material to Semi-finished Products ». *Advanced Engineering Materials,* vol. 5, n° 6, p. 393-398.

Slama, C., and M. Abdellaoui. 2000. « Structural characterization of the aged Inconel 718 ». *Journal of Alloys and Compounds,* vol. 306, n° 1-2, p. 277-284.

Slama, C., and G. Cizeron. 1997. « Structural behaviour of INC 718 (Etude du comportement structural de l'alliage NC 19 Fe Nb (Inconel 718)) ». *Journal de physique. III,* vol. 7, n° 3, p. 665-688.

Smaga, M., F. Walther and D. Eifler. 2008. « Deformation-induced martensitic transformation in metastable austenitic steels ». *Materials Science and Engineering A,* vol. 483-484, n° 1-2 C, p. 394-397.

Solomon, N., and I. Solomon. 2010. « Deformation induced martensite in AISI 316 stainless steel ». *Revista de metalurgia,* vol. 46, n° 2, p. 121-128.

Song, Jung Han, and Hoon Huh. 2007. « The effect of strain rate on the material characteristics of nickel-based superalloy inconel 718 ». *Key Engineering Materials,* vol. 340-341 I, p. 283-288.

Song, K. H., Y. B. Chun and S. K. Hwang. 2007. « Direct observation of annealing twin formation in a Pb-base alloy ». *Materials Science and Engineering: A,* vol. 454–455, p. 629-636.

Stinville, J. C., N. Vanderesse, F. Bridier, P. Bocher and T. M. Pollock. 2015. « High resolution mapping of strain localization near twin boundaries in a nickel-based superalloy ». *Acta Materialia,* vol. 98, p. 29-42.

Sundararaman, M., P. Mukhopadhyay and S. Banerjee. 1988. « Precipitation of the δ-Ni3Nb phase in two nickel base superalloys ». *Metallurgical Transactions A,* vol. 19, n° 3, p. 453-465.

Swift, H. W. 1952. « Plastic instability under plane stress ». *Journal of the Mechanics and Physics of Solids,* vol. 1, n° 1, p. 1-18.

Talonen, J., P. Aspegren and H. Hänninen. 2004. « Comparison of different methods for measuring strain induced α-martensite content in austenitic steels ». *Materials Science & Technology,* vol. 20, n° 12, p. 1506-1512.

Talonen, Juho, Pertti Nenonen, Gersom Pape and Hannu Hanninen. 2005. « Effect of strain rate on the strain-induced , &rarr -martensite transformation and mechanical properties of austenitic stainless steels ». *Metallurgical and Materials Transactions A: Physical Metallurgy and Materials Science,* vol. 36 A, n° Compendex, p. 421-432.

Talyan, V., R. Wagoner and J. Lee. 1998. « Formability of stainless steel ». *Metallurgical and Materials Transactions A,* vol. 29, n° 8, p. 2161-2172.

Totten, George E. 2007. *Steel heat treatment : metallurgy and technologies*, 2nd. Boca Raton, FL: Taylor & Francis, 833 p.

Tsuta, Toshio, and Jorge Cortes R. A. 1993. « Flow Stress and Phase Transformation Analyses in Austenitic Stainless Steel Under Cold Working : Part 2, Incremental Theory Under Multiaxial Stress State by the Finite-Element Method ». *JSME international journal. Ser. A, Mechanics and material engineering,* vol. 36, n° 1, p. 63-72.

Valle, L. C. M., L. S. Araújo, S. B. Gabriel, J. Dille and L. H. Almeida. 2013. « The Effect of δ Phase on the Mechanical Properties of an Inconel 718 Superalloy ». *Journal of Materials Engineering and Performance,* vol. 22, n° 5, p. 1512-1518.

Vanderesse, N., M. Anderson, F. Bridier and P. Bocher. 2016. « Inter- and intragranular delta phase quantitative characterization in Inconel 718 by means of image analysis ». *Journal of Microscopy,* vol. 261, n° 1, p. 79-87.

Venables, J. A. 1962. « The martensite transformation in stainless steel ». *Philosophical Magazine,* vol. 7, n° 73, p. 35-44.

Vollertsen, F. 2001. « State of the art and perspectives of hydroforming of tubes and sheets ». *Journal of Materials Science and Technology,* vol. 17, n° 3, p. 321-324.

Zhang, S. H. 1999. « Developments in hydroforming ». *Journal of Materials Processing Technology,* vol. 91, n° 1-3, p. 236-244.